

SEMICONDUCTOR QUANTUM DOTS DRIVEN BY
RADIATIVE AND NONRADIATIVE ENERGY
TRANSFER FOR HIGH-EFFICIENCY HYBRID LEDs
AND PHOTOVOLTAICS

A THESIS
SUBMITTED TO THE DEPARTMENT OF ELECTRICAL AND
ELECTRONICS ENGINEERING
AND THE GRADUATE SCHOOL OF ENGINEERING AND SCIENCE
OF BILKENT UNIVERSITY
IN PARTIAL FULLFILMENT OF THE REQUIREMENTS
FOR THE DEGREE OF
MASTER OF SCIENCE

By
Burak Güzeltürk
August 2011

I certify that I have read this thesis and that in my opinion it is fully adequate, in scope and in quality, as a thesis for the degree of Master of Science.

Assoc. Prof. Dr. Hilmi Volkan Demir (Supervisor)

I certify that I have read this thesis and that in my opinion it is fully adequate, in scope and in quality, as a thesis for the degree of Master of Science.

Assoc. Prof. Dr. Vakur B. Ertürk

I certify that I have read this thesis and that in my opinion it is fully adequate, in scope and in quality, as a thesis for the degree of Master of Science.

Prof. Dr. Engin Umut Akkaya

Approved for the Graduate School of Engineering and Science:

Prof. Dr. Levent Onural
Director of Graduate School of Engineering and Science

ABSTRACT

SEMICONDUCTOR QUANTUM DOTS DRIVEN BY
RADIATIVE AND NONRADIATIVE ENERGY
TRANSFER FOR HIGH-EFFICIENCY HYBRID LEDs
AND PHOTOVOLTAICS

Burak Güzeltürk
M.S. in Electrical and Electronics Engineering
Supervisor: Assoc. Prof. Dr. Hilmi Volkan Demir

August 2011

Today the world energy demand has overtaken unprecedented consumption levels, which have never been reached before in the history of the world. The current trends indicate that the increasing demand for energy will tend to continue at an increasing pace in the coming decades due to worldwide globalization and industrialization. Scientific community is challenged to devise and develop fundamentally new technologies to cope with the energy problem of the world. To this end, optoelectronics can offer several solutions for energy efficiency both in light harvesting and generation. In this thesis, we propose and demonstrate enhanced light generation and harvesting by utilizing both radiative and nonradiative energy transfer capabilities of semiconductor nanocrystal quantum dots, which are profited for the development of novel hybrid devices combining superior properties of the constituent material systems. One of our proposals in this thesis relies on grafting nanostructured light emitting diodes with nanocrystal quantum dots to realize highly efficient color conversion. To the best of our knowledge, we report the highest nonradiative energy transfer efficiency of 83% obtained at room temperature for this type of color-conversion light emitting diodes owing to the architectural superiorities of their nanostructure. In another proposal, we addressed charge injection problems of electrically pumped nanocrystal-based light emitting diodes. We proposed and demonstrated the utilization of novel excitonic injection scheme to drive such LEDs of nanocrystals, which may become prominent especially for the display

technology. Finally, we proposed and implemented quantum dot down-conversion layers in nanostructured silicon solar cells to benefit the advantages of their nanostructured architecture. We have shown that nanostructured silicon solar cells lead to stronger enhancements compared to the planar counterparts.

Keywords: Nanocrystals, quantum dots, light emitting diodes (LEDs), solar cells, nonradiative energy transfer, excitonics.

ÖZET

YARI İLETKEN NANOKRİSTAL KUVANTUM
NOKTACIKLARIN IŞIMALI VE IŞIMASIZ ENERJİ
TRANSFERİ KULLANIMI İLE VERİMLİLİĞİ
ARTIRILMIŞ MELEZ IŞIK YAYAN DİYOTLAR VE
GÜNEŞ GÖZELERİ

Burak Güzeltürk
Elektrik ve Elektronik Mühendisliği Bölümü Yüksek Lisans
Tez Yöneticisi: Doç. Dr. Hilmi Volkan Demir
Ağustos 2011

Günümüzde dünyanın enerji ihtiyacı şimdiye kadar hiç ulaşılmamış tüketim seviyelerine çıkmış bulunmaktadır. Yapılan tahminlere göre dünyadaki hızlı büyüme ve globalleşme enerji tüketimini gelecekte daha da artıracaktır. Bilim dünyası daha verimli enerji üretim ve kullanım teknolojileri geliştirebilmek için yoğun bir uğraş vermektedir. Işık ve elektronik teknolojilerini birleştiren optoelektronik dalı, güneş gözeleri ve ışık yayan diyotlar ile enerji üretim ve kullanım problemine verimli çözümler sunmaktadır. Bu tezde, yarı iletken nanokristal kuvantum noktacıklarının ışımalı ve ışımasız enerji transferi özelliklerini kullanarak, güneş pillerinin ve ışık yayan diyotların verimliliklerini artırmaya yönelik çalışmalar önerdik ve uygulamalarını gösterdik. Nano-sütun mimarisine sahip mavi ışıyan diyotları daha uzun dalga boyunda ışıyan nanokristaller ile melezleştirerek, nano-sütun yapısının sağladığı üstün mimari özellikleri sayesinde, diyotların yapı taşı kuvantum kuyular ile kuvantum noktacıkları arasında şimdiye kadar bilgimiz dahilinde rapor edilmiş en yüksek % 83'lük enerji transfer verimliliğini elde ettik. Bu sayede, renk dönüştürücülü ışık yayan diyotlar için gelecek vaadeden melez tasarımlar önerdik. Bundan başka, yük pompalaması metodu ile çalışan nanokristal tabanlı ışık yayan diyotlarda yaşanan yük sürme problemine çözüm olarak özgün ve yeni bir metot geliştirdik. Işımasız enerji transferi sayesinde uyarım enerjisini doğrudan nanokristallere pompalayarak elektro-ışımaya yapabildiği nanokristal tabanlı ışık

yayan diyotları geliřtirdik. Son olarak, silisyum tabanlı güneř pillerinin temel sorunlarından biri olan kısa dalga boyundaki ışığın verimsiz dönüřtürülmesi problemine çözümler olarak nano-sütun yapısında olan silisyum güneř gözelerinin ışığı yüksek dalga boyuna çeviren nanokristaller ile birleřtirilmesini gösterdik. Nano-sütun yapısı sayesinde, ışığın sütunlar arasına hapsedilmesinden dolayı, klasik düz mimarilere göre kısa dalga boyunda çok daha fazla iyileřtirme sağladık.

Anahtar Kelimeler: Nanokristaller, kuantum noktacıkları, güneř pili, ışık yayan diyot, ışımali ve ışımali enerji transferi.

Acknowledgements

On the verge of finishing my Master's degree, I feel happy that I have made the right decision of pursuing an academic career in interdisciplinary branches of science. Three years ago, I have joined the group of Prof. Hilmi Volkan Demir when I was just starting my senior year. Through these years, I have learned a lot from him both technically and personally. I would like to thank him for his contributions and guidance.

This thesis would not be possible without our good friends and colleagues. First, I would like to thank all past and present Demir group members for being always helpful and friendly to me. Specially, I would like to thank Evren Mutlugün and Dr. Sedat Nizamoğlu from whom I have learned my basic lab skills and they always responded whenever I asked for help. I would like to thank Tuncay Özel, Özge Özel, Emre Ünal, Dr. Rohat Melik, Emre Sarı and Can Uran, my seniors in the group, who always helped me and guided me very well. I would like to thank Dr. Nihan Koşku Perkgöz, Özgün Akyüz, Dr. Olga Samarskaya, Dr. Urartu Ö. Ş. Şeker, Gülis Zengin, Neslihan Çiçek, Mustafa Akın Sefunç, Onur Akın, Gürkan Polat, Aslı Ünlügedik, Talha Erdem, Veli Tayfun Kılıç, Hatice Ertuğrul, Sina Toru, Sayım Gökkyar, Uğur Karatay, Cüneyt Eroğlu and Kıvanç Güngör, Dr. Ludwig P. Hernandez-Martinez, Shahab Akhavan, Yusuf Keleştemur, A. Fatih Cihan, Ozan Yerli, Yasemin Coşkun, Aydan Yeltik, Togay Amirahmadov, Dr. Vijay Kumar Sharma and Onur Erdem for always being kind, helpful and friendly.

I would like to thank engineers and laboratory staff in UNAM and ARL who made our lives easier all the time.

I would like to acknowledge and thank TUBİTAK-BİDEB (2210 - Yurt İçi Yüksek Lisans Burs Programı) for the financial support throughout this thesis.

I would like thank Nisa Yeşilgöl without whom these last two years will be less colorful.

Finally, I would like thank my parents Halit and Nesrin for being always there whenever I need them along with their enormous patience and love.

Table of Contents

1. INTRODUCTION	1
1.1 MOTIVATION OF THE THESIS.....	1
1.2 ORGANIZATION OF THE THESIS	4
2. SCIENTIFIC BACKGROUND.....	6
2.1 PHOTOVOLTAIC SOLAR CELLS	6
2.1.1 Principles of Operation.....	6
2.1.2 Important Device Parameters and Characterization Techniques.....	10
2.2 SEMICONDUCTOR LIGHT EMITTING DIODES	15
2.2.1 Principles of Operation.....	15
2.2.2 Organic Light Emitting Diodes.....	18
2.2.3 Important Parameters and Characterization.....	23
2.3 EXPERIMENTAL METHODS.....	26
2.3.1 Fluorescence Lifetime Spectroscopy.....	26
2.3.2 Steady State Optical Characterizations.....	27
2.3.3 Material and Structural Characterizations	29
2.3.4 Fabrication Techniques	30
3. SEMICONDUCTOR QUANTUM DOT NANOCRYSTALS.....	31
3.1 INTRODUCTION	31
3.2 QUANTUM MECHANICS BEHIND NANOCRYSTAL QUANTUM DOTS	35
3.3 SYNTHESIS OF NANOCRYSTAL QUANTUM DOTS	38
3.4 PROPERTIES OF NANOCRYSTAL QUANTUM DOTS.....	42
3.5 APPLICATIONS	46
4. RADIATIVE AND NONRADIATIVE ENERGY TRANSFER MECHANISMS.....	49
4.1 INTRODUCTION	49
4.2 NONRADIATIVE ENERGY TRANSFER	49
4.3 RADIATIVE ENERGY TRANSFER	57
4.4 APPLICATIONS	57
5. RADIATIVE ENERGY TRANSFER FROM QUANTUM DOTS TO SILICON NANOPILLARS FOR ENHANCED NOVEL SILICON SOLAR CELLS.....	59
5.1 INTRODUCTION AND MOTIVATION	59
5.2 PROPOSAL AND PRINCIPLES OF OPERATION	62
5.3 EXPERIMENTS AND RESULTS	65
5.4 CONCLUSIONS.....	75
6. NONRADIATIVE ENERGY TRANSFER FROM INGAN/GAN MULTI QUANTUM WELL NANOPILLARS TO QUANTUM DOTS: EFFICIENT COLOR CONVERTERS FOR LIGHT EMITTING DIODES	76
6.1 INTRODUCTION AND MOTIVATION	76
6.2 PROPOSAL AND PRINCIPLES OF OPERATION	80
6.3 EXPERIMENTS AND RESULTS	82
6.4 CONCLUSIONS.....	96

7. SPECIFICALLY ANCHORED POLYMER - QUANTUM DOT HYBRIDS: TEMPERATURE DEPENDENT NONRADIATIVE ENERGY TRANSFER DYNAMICS FOR EXCITONICALLY PUMPED QUANTUM DOT BASED LIGHT EMITTING DIODES	98
7.1 INTRODUCTION AND MOTIVATION	98
7.2 PROPOSAL AND PRINCIPLES OF OPERATION	100
7.3 TEMPERATURE DEPENDENT NONRADIATIVE ENERGY TRANSFER DYNAMICS	103
7.4 EXCITONICALLY DRIVEN QD-LEDs	133
7.5 CONCLUSIONS	143
8. CONCLUSIONS	145
6.1 CONTRIBUTIONS	147
9. BIBLIOGRAPHY	148

List of Figures

Figure 2.1.1.1 Schematic representation of a p-n junction diode. Material is excited with photons in the visible range. Photogenerated electron-hole pairs are represented. Due to doping of the material resulting immobile ionized acceptors and donors along with free electrons and holes are shown. Energy vs. position schematic shows the alignment of the p- and n-doped regions with depletion region where built-in electric field exists.	8
Figure 2.1.1.2 Principle of operation of a solar cell is depicted. Electron and hole pair is created via photo-generation. A minority carrier (e.g., a hole in this case) diffuses in the region (1, 2). If it can reach the junction (i.e., depletion region) after diffusing (3), it is drifted to the other region where it is majority carrier (4). Due to this drift current, in the external circuit, the majority carrier (e.g., electron in this case) is given to external circuit (5) so that it recombines with a majority carrier in the other region (e.g., hole) through external circuit (6).	9
Figure 2.1.2.1 Short circuit current mode of a p-n junction solar cell.....	11
Figure 2.1.2.2 Open circuit mode operation of a p-n junction solar cell.....	12
Figure 2.1.2.3 Exemplary I-V curve of a silicon solar cell studied in this thesis. Important solar cell parameters, I_{sc} , V_{oc} , P_{max} , $P_{max\ ideal}$, $V_{\text{maximum power point}}$ and $I_{\text{max power point}}$ are shown on I-V and power – voltage plots.....	13
Figure 2.1.2.4 Measurement set-up for wavelength dependent responsivity and external quantum efficiency.....	14
Figure 2.1.2.5 Exemplary external quantum efficiency plot for a silicon based solar cell. EQE is low at both ends of the spectrum. In the UV part, it is low due to poor utilization of electron-hole pairs close to the surface. In the IR part, it is low due to poor absorption of silicon with back contact problems.	15

Figure 2.2.1.1 (a) A p-n homojunction diode under zero bias is shown with free electron and holes in n- and p-doped regions, respectively. (b) A p-n homojunction diode under forward bias is shown. Built-in electric field is reduced. Diffusion current increases. Quasi-Fermi levels form due to injection. Formed electron-hole pairs can emit light (i.e., electroluminescence).....	17
Figure 2.2.2.1 A typical band diagram of a conjugated polymer where LUMO level corresponds to conduction band and HOMO level to valence band.	19
Figure 2.2.2.2 The simplest device design for polymer based OLED. Top contact is used as cathode and bottom contact is used as anode.	20
Figure 2.2.2.3 Three different bias conditions for simple device design of sandwiched polymer layer between anode and cathode. (a) At zero bias charges cannot be injected. (b) At threshold forward bias level, charge injection becomes possible (immediately after this bias level). (c) At bias levels greater than threshold, charge injection can take place via tunneling.	20
Figure 2.2.2.4 An advanced design for an efficient OLED.	22
Figure 2.2.3.1 An exemplary I-V curve of an OLED.	23
Figure 2.2.3.2 An exemplary LI data of an OLED.	24
Figure 2.2.3.3 An EL spectrum of a quantum dot based LED.	25
Figure 2.3.1.1 FluoTime 200 time resolved fluorescence spectroscopy system used for time resolved measurements in this thesis.	27
Figure 3.1.1 Colloidally synthesized nanocrystal quantum dot with surface passivating ligands attached to surface Cd atoms are shown representatively. ...	33
Figure 3.1.2 Schematical examples of type I and type II core/shell NQDs.	35
Figure 3.2.1. Schematic representation of semiconductor NQDs , along with its bulk, showing modified electronic band structures due to quantum confinement.	38

Figure 3.3.1 Synthesis set-up consisting of Schlenk line for Argon flow and vacuum. Cold trap is utilized for vacuum line. Oxygen absorber is utilized for making oxygen free Ar flow.....	39
Figure 3.3.2 Glove box filled with nitrogen to create oxygen free environment for oxygen sensitive material processing.....	40
Figure 3.3.3 Our-synthesized CdSe core and CdSe/ZnS core/shell NQDs with different sizes emitting at correspondingly different wavelengths.	41
Figure 3.4.1. Photoluminescence and absorbance of CdSe/ZnS NQDs having different sizes (the largest particles has red emission, while the smallest has green emission).	43
Figure 3.4.2 Highly monodisperse CdSe/ZnS NQDs.	44
Figure 3.4.3 High resolution TEM image of CdSe/CdSe-CdS-ZnS/ZnS alloy like core/shell NQDs having PL QEs around 80%.	45
Figure 4.2.1 Exemplary experiment for the demonstration of the presence of NRET.....	50
Figure 4.2.2 An oscillating Hertzian dipole is shown with electric field radiation patterns in the near-field.	51
Figure 4.2.3 Schematic of the principle of operation of NRET between donor and acceptor luminescent molecules.	53
Figure 4.2.4 Jablonski energy diagram of a luminescent organic molecule with possible de-excitation pathways.....	56
Figure 5.1.1 Typical architecture of a planar crystalline silicon solar cell. Short wavelength (highly energetic) photons are absorbed very close to the silicon surface.....	61
Figure 5.1.2 Exemplary external quantum efficiency vs. wavelength of a silicon nanowire solar cell used in this study.....	62
Figure 5.2. 1 Illustration of the principles of operation of the nanocrystal up-converter layers for silicon solar cell. Comparison of the planar and nanopillar architecture is pictorially presented. UV and blue waves are shown as the excitation photons. Orange colored waves represents the longer wavelength	

emission of nanocrystals after conversion of UV and blue photons. Black colored arrows represents the built-in electric field in depletion region.	63
Figure 5.2.2 Absorption (black line) and emission spectrum (red line) of the utilized CdSe nanocrystals.	64
Figure 5.3.1 Scanning electron micrographs for fabricated radial p-n junction Si nanopillar solar cell are shown. The device architecture is also depicted. Photograph of the active device is given, where device active area is $\sim 0.81 \text{ cm}^2$	67
Figure 5.3.2 Transmission electron micrograph of synthesized CdSe nanocrystals (scale bar is 5 nm).	68
Figure 5.3.3 SEM images of silicon nanopillars after nanocrystals are incorporated.	69
Figure 5.3.4 Current-Voltage (I-V) curves of the nanopillar solar cell before and after nanocrystal incorporation under AM 1.5G 1sun illumination conditions.	71
Figure 5.3.5 Enhancement in responsivity due to nanocrystal hybridization in planar and nanopillar solar cell devices is presented. Inset shows external quantum efficiencies of the nanopillar and planar devices before and after nanocrystal incorporation.	72
Figure 5.3.6 Measured reflectivity of silicon surface with and without nanocrystal coating.	73
Figure 5.3.7 FDTD analysis of reduction of the reflectivity and enhanced light trapping of nanopillar silicon solar cell due to nanocrystal incorporation. Inset shows the measured reflection (%) before and after nanocrystal incorporation.	74
Figure 6.1.1 Color converter light emitting diodes can benefit NQDs as optically active converting materials. Combination of different color emitting NQDs can be used to generate white light.	78
Figure 6.1.2 A similar pump LED and a monolayer of CdSe NQDs used by Achermann <i>et al.</i> where they etched GaN capping layer in order to decrease the separation between top QW and monolayer of the NQDs. [83].	79

Figure 6.2.1 NQDs elliptically etched holes (a) reaching down to QWs, (b) lying only in p-GaN capping layer. [84] (This figure is reproduced with permission of the publisher John Wiley & Sons Inc.).....	80
Figure 6.2.2 InGaN/GaN multi-quantum-well nanopillars obtained via inductively plasma reactive ion etching (ICP REI). Inbetween pillars are incorporated NQDs.....	82
Figure 6.3.1 Explanatory schematics for the fabrication of InGaN/GaN MQW nanopillar structures.	83
Figure 6.3.2 SEM image of the top-down fabricated InGaN/GaN MQW nanopillars.	84
Figure 6.3.3 X-ray diffraction measurement of the nanopillars (blue) and planar (black) architecture.....	84
Figure 6.3.4 (a) Photoluminescence spectra of InGaN/GaN multi-quantum-well planar (black) and nanopillar (blue) structures, and (b) time resolved fluorescence decays for planar (black) and nanopillar (blue).	86
Figure 6.3.5 In-solution PL and absorbance spectra of the utilized CdSe/ZnS NQDs in this part of the thesis. Emission of the planar and nanopillar LEDs are also shown to indicate the spectral overlap between the donor emission and the acceptor absorption.....	88
Figure 6.3.6 (a) Time resolved fluorescence decays of multi-quantum-wells in nanopillar architecture with and without red NQDs along with exponential fits. (b) Steady state PL spectrum of the nanopillar NQD hybrid using red NQDs.	91
Figure 6.3.7 (a) Time resolved fluorescence decays of multi-quantum-wells in nanopillar architecture with and without green and yellow NQDs along with their fit exponential fits. (b) Steady state PL spectra of the nanopillar NQD hybrids using yellow and green NQDs.....	92
Figure 7.2.1 Five different vials containing functionalized polyfluorene (PF) derivative co-polymer emitting in blue and our own-synthesized core/shell	

NQDs of different sizes and emission wavelengths (green to orange).	
Functionalized PF is depicted as donating its excitons to the NQDs.....	101
Figure 7.2.2 Schematic of the QD-LED device architecture with the actual photograph of a fabricated device.	102
Figure 7.2.3 Schematic for the principle of operation of the exciton pumped QD- LEDs where electrons ‘-’ and holes ‘+’ are injected from cathode and anode, respectively. Also, red dots represent the hybridized NQDs. Due to finite mobility of the charges in the polymer matrix, they are combined to form excitons, which can be effectively transferred to the NQDs via nonradiative energy transfer.....	102
Figure 7.3.1 Schematic depiction of phase segregation between NQDs and polymer.....	104
Figure 7.3.2 Carboxyl group functionalized polyfluorene derivative co-polymer.	106
Figure 7.3.3 Non-functionalized polyfluorene derivative co-polymer used as a negative control group.	106
Figure 7.3.4 SEM images of thin films of (a)-(d) NQDs with non-functionalized PF blends shown with material EDAX analysis of the segregated parts of the films in (d), and (e) NQDs with functionalized PF hybrids.	109
Figure 7.3.5 Atomic force microscopy images of non-functionalized PF-NQD blends: (a) topography, and (b) phase image.	110
Figure 7.3.6 STEM images of NQDs in (a) functionalized PF and (b) non- functionalized PF.....	113
Figure 7.3.7 In-solution (a) and in-film (b) absorption - emission spectra of functionalized PF shown along with the absorption spectrum of NQDs..	114
Figure 7.3.8 (a) Lifetimes of the functional PF in the presence and absence of the quantum dots for 3 w% and 45 w% hybrids with respect to temperature. (b) Energy transfer efficiencies extracted from LAF model with respect to temperature for 3 w% and 45 w% cases.	119
Figure 7.3.9 NRET rates for 3 w% and 45 w% hybrids with respect to temperature.....	121

Figure 7.3.10 Iso-efficiency curves with respect to D vs. n_A and L_D vs. Acceptor-acceptor separation for (a) 3 w% and (b) 45 w% hybrids. Semitransparent pink regions indicate the possible regions for D and L_D for predicted n_A and NQD separations in thin film.....	124
Figure 7.3.11 One dimensional schematic interpretation of the exciton diffusion in polymer in relation to NRET dynamics.....	128
Figure 7.3.12 Steady state PL for only polymer and hybrid at different temperatures [PLs should be corrected with the correction factor.	130
Figure 7.3.13 Amplitude averaged acceptor lifetimes for (a) 3 w% and (b) 45 w% at each temperature and sample measured for its peak emission wavelength.	132
Figure 7.3.14 Exemplary lifetime decays of donor alone, 3 w% and 45 w% with IRF at room temperature.....	133
Figure 7.4.1 Schematic representation of the fabrication steps of the QD-LEDs following the fabrication steps 1-8. Photograph of a fabricated and encapsulated device is also shown.	135
Figure 7.4.2 Exemplary electroluminescence of a QD-LED made up of non-functionalized PF and core/shell NQDs.....	136
Figure 7.4.3 EL spectrum of excitonically driven QD-LEDs prepared with increasing concentration of NQDs and only polymer-LED at same voltage level with normalized EL spectra.....	137
Figure 7.4.4 Typical I-V curve for the excitonically driven QD-LEDs fabricated with functionalized PF and red emitting CdSe/ZnS NQDs.	138
Figure 7.4.5 Luminance – current (LI) measurement of the fabricated excitonically QD-LED consisting of functionalized PF and red emitting CdSe/ZnS NQDs.	139
Figure 7.4.6 EL spectrum of excitonically injection pumped QD-LEDs utilizing different color emitting NQDs.	140
Figure 7.4.7 EL spectrum of excitonically driven QD-LED with functionalized PF and green emitting CdSe/CdS/ZnS NQDs designed for obtaining pure green emission.....	141

Figure 7.4.8 Cyclic voltammetry measurement of functionalized PF in order to determine its highest occupied molecular orbital level (HOMO).	142
Figure 7.4.9 External quantum efficiency vs. injected current for a QD-LED showed relatively high efficiencies.	143

List of Tables

Table 5.3.1 Evolution of solar cell parameters before and after incorporation of nanocrystals.....	70
Table 6.3.1 Total decay rate for nanopillar alone and energy transfer rates, efficiencies and percent of transferred electron-hole pairs for red, orange and yellow emitting NQDs incorporated into nanopillars are shown.....	94
Table 6.3. 2. Experimental and theoretical energy transfer rates are compared. Other parameters used for the calculation of the theoretical rates are also given (J , n , d , and σ).....	96

This thesis is dedicated to my parents ...

Chapter 1

Introduction

1.1 Motivation of the Thesis

In today's world, energy production and utilization became a vital problem of the human society. Environment-unfriendly means of energy production escalate the global warming. Inefficient utilization of energy in lighting, transportation, heating, etc. also causes significant loss of effort and sources. Scientific community is challenged to develop better ways of production and utilization of the energy.

Optoelectronic devices such as photovoltaic solar cells and light emitting diodes offer possible competent solutions to the problems of energy. Today, luminescent semiconductor nanocrystal quantum dots arise as a unique and novel material class, holding great promise to be harnessed for optoelectronics technology for excelled devices. To this end, we propose and show enhancement of photovoltaic solar cells and light emitting diodes via hybridization of semiconductor nanocrystal quantum dots while promoting and mastering their radiative and nonradiative energy transfer capabilities.

According to U.S. Energy Information Administration, 12% of the residential and 25% of the commercial (e.g., industry, government) electrical consumption in U.S.A is due to lighting. [1] According to another report, approximately 19% of the total electricity production on earth is used for lighting purposes. [2]

Although a huge portion of the produced electricity is used for lighting, incandescent and fluorescent lamps still make the main means of lighting, which are not quite efficient as compared to the light emitting diodes. Incandescent lamps provide poor luminous efficiencies (lm/W) around 10-20 lm/W with short lifetimes up to 1000 hours. [3] Fluorescent lamps, which can be as efficient as 30 - 80 lm/W, feature lifetimes limited to at most 10,000 hours. [3] However, light emitting diodes can offer both high efficiencies around 30-100 lm/W and increased lifetimes more than 30,000 hours. [3] Year by year, LED market grows faster. In 2006, the market was valued to be 4 billion USD. Predictions for 2015 expect the LED market to grow 15 billion USD. [4] Wide application areas of LEDs such as display technology, automotive and general lighting contribute to this rapid growth of the LED market. Although there have been many advancements in the LED technology, the pursuit of better and more efficient devices still continues.

In the-state-of-art LED technology, color converter layers are typically used to obtain white light. [5] In display applications, Red-Green-Blue (R-G-B) colors can also be obtained via color conversion method. Color converter layers generally employ rare-earth doped phosphor materials. However, these phosphors limit the optical quality of the LEDs since their emission spectrum cannot be tuned and controlled easily. Novel luminescent quantum dot nanocrystals are promising and interesting materials showing competitive advantage to be used for color converter layers. [6] These quantum dots are promising candidates to replace phosphor based converter layers in the future. [7] In this thesis, we focus on the utilization of these novel luminophore quantum dot nanocrystals as efficient color converter layers for novel nanostructured LEDs to harness increased nonradiative energy transfer mechanisms between the pump LED and quantum dot nanocrystals. The pump LED is also nanostructured to exploit the nonradiative energy transfer means effectively.

Rising field of organic optoelectronics draws a great attention owing to its advantages such as low cost production of versatile devices even on flexible substrates with the ease of production methods such as solution processing. Hybrid systems based on quantum dot nanocrystals and organic materials can combine the superior properties of both material systems. Hybrid quantum dot based LEDs have been proposed to be promising devices for display applications. [8, 9] However, due to poor electrical properties and high potential barrier on the ligands of the colloiddally synthesized quantum dot nanocrystals, charge injection problems exist in these devices. In this thesis, we propose and present a proof-of-concept demonstration of excitonically pumped quantum dot based hybrid LEDs. We investigate the dynamics of exciton injection that is achieved via nonradiative energy transfer from conductive polymers to quantum dot nanocrystals. Exciton injection scheme is a novel approach which can be utilized as an alternative method for electroluminescent nanocrystal-based LEDs.

Convenient energy production means are fossil fuels such as coal, natural gas, petroleum and nuclear sources which are not quite nature friendly. Burning fossil fuels causes increased greenhouse gas emission, which has contributed to the accelerated global warming problem in the previous century. Emission of the greenhouse gases should be cut down to preserve our living habitat. Alternative and clean energy sources are welcomed today with the support of international communion. Photovoltaic (PV) solar cells are one of the most promising candidates as alternative and clean energy sources primarily because enormous potential of the Sun, although there are cost issues for wide scale use. The Sun delivers on the average 89,000 TW power instantly to earth crust, which is three orders of magnitude greater than the worldwide energy consumption of about 15 TW. [10] If we were to compare the potential of the Sun with other energy sources on earth, we would see that the annual solar irradiation energy impinging earth is a few orders of magnitude greater than the potential of the individual energy sources on earth (e.g., coal, natural gas). [11] Examples of the

potential of solar energy are stunning. If we were to cover two thirds of Sahara desert with commercially available 15% efficient silicon solar panels, then all of the energy demand of the world could be only met by solar means. Also, if we were to cover roof tops of the buildings in Antalya, then almost 18% of the energy demand of Turkey could be met by those solar panels. [12] However, there exist feasibility problems due to economical and production related issues. Today's PV technology has a limited capacity of production so that covering some part of Sahara with 15% efficient modules will take almost 100 years of production. Although alternative solar cell technologies except silicon has been developed such as organic solar cells offering the ease of roll-to-roll fabrication methods, silicon is still the dominant material in PV technology. [13] This is because material processing technologies for silicon are quite mature thanks to developments in micro-fabrication technologies. Silicon is also one of the most abundant materials on earth. Nevertheless, due to intrinsic properties of silicon, optoelectronic devices such as photo-detectors and solar cells suffer from poor UV and blue light responsivities. For photovoltaic applications, poorly utilized UV and blue spectra constitutes almost 10 % of the total spectrum of the sun light. In this thesis, we propose the utilization of novel luminescent quantum dot nanocrystals as wavelength up-converter layers so that UV and blue photons in sun light will be harvested better by silicon solar cells. To benefit this color conversion approach, nanostructured silicon solar cell is utilized because of unique optical trapping properties.

1.2 Organization of the Thesis

This thesis consists of eight chapters. Here is the organization of the rest of the thesis. In Chapter 2, we review the theory and experimental methods related to the scientific content of this thesis. In Chapter 3, novel luminescent quantum dot nanocrystals are presented in detail including the theory of the quantum confinement. Here we also explain the synthesis of these quantum dots. Subsequently, possible applications are summarized. In Chapter 4, we discuss the physics of radiative and nonradiative energy transfer mechanisms. Quantum

dot based application examples are also provided. In Chapter 5, we present our study on enhanced silicon nanopillar radial p-n junction solar cells via radiative energy transfer from quantum dot nanocrystals utilized as wavelength down-converters of UV-blue photons in the sunlight. In Chapter 6, we investigate the utilization of nanopillar InGaN/GaN multi-quantum-well pump LEDs as efficient energy donors for color converter layers made up of quantum dots. The physics and dynamics of energy transfer are studied both experimentally and theoretically. Results of the proof-of-concept hybrid devices are presented. In Chapter 7, we present our proposal of novel exciton injection pumping scheme for electroluminescent quantum dot nanocrystal based LEDs. Hybrid material system of nanocrystals and functionalized polymer that is proposed to achieve exciton injection is explained. Temperature dependent exciton transfer dynamics are investigated using time resolved fluorescence measurements. Physical model are discussed. The proof of concept devices are also presented. Last, in Chapter 8, we conclude the thesis with remarks on the completed projects and future steps.

Chapter 2

Scientific Background

2.1 Photovoltaic Solar Cells

2.1.1 Principles of Operation

Although there are different generations of solar cells based on various material systems, the fundamental principle of operation is the same for all generations of devices. The main goal of a photovoltaic solar cell is to convert the sunlight into electricity. Semiconductor materials are the most appropriate material class to be utilized for photovoltaics because of available energy band gaps tunable in the spectra of the sunlight. Absorption of a photon by semiconductor material causes creation of an excitation energy carrier called electron hole (e-h) pair in the material. The principle of operation of the photovoltaic devices depends on the separation of the created e-h pairs in the p-n junction so that photocurrent is generated in the external circuit. For this reason, solar cells act as current sources.

The first generation solar cells use only single p-n junction diodes made up of single crystalline silicon as the active absorbing material. The first generation devices are still popular since they can provide respectively high power conversion efficiencies despite the high production costs due to utilization of high quality single crystalline silicon substrates. [14] The second generation devices also called thin film solar cells have been introduced against the first

generation devices to reduce the costs via utilization of very thin semiconductor compound or alloy materials. Common materials used for the second generation photovoltaics are amorphous silicon (a-Si), cadmium sulfide/cadmium telluride (i.e., CdS/CdTe) and copper indium gallium di-selenide (i.e., CIGS). However, these devices are generally limited with relatively low power conversion efficiencies due to poor absorption of the sunlight in thin films.

Newly emerging third generation solar cells based on several different approaches such as organic conductive materials, conductive oxides with dye sensitization, optical concentrators, multi junctions, carrier multiplication (i.e., multiple carrier generation), hot carrier collection, quantum dot sensitization, IR utilization, and nano-structured light trapping. The physics, chemistry and materials may change a lot, but the operation principle still follows the basic photovoltaic effect of e-h pair photogeneration and dissociation and subsequent charge collection. [15] It is also worth noting that there are differences between various photovoltaic devices in terms of how a photogenerated e-h pair is dissociated (e.g., through built-in field, acceptor-donor interaction).

To give a detailed picture of the principle of operation of photovoltaic solar cells, a simple p-n junction diode would be the easiest to understand. Here we depict a p-n homojunction diode under light illumination with a photon energy larger than the band gap of the utilized semiconductor material (see Figure 2.1.1.1). Although there are a huge number of electrons in a semiconductor material, most of them are bound to atomic nucleus, so called valence electrons, which are incapable of moving the crystalline material freely. If some of the electrons gain energy due to excitation (i.e., photon absorption or electrical injection), then excited electrons in the valence band would move freely in the conduction band. Empty states in the valence band by excited electrons are then called holes, virtual positively charged mobile charge carriers. Both electrons and holes can contribute to conduction in a semiconductor material. In a n-doped material, there are a lot of free electrons that constitute the majority

carriers and there are positively charged immobile dopant atoms (see Figure 2.1.1.1) (i.e., since they have donated their electrons). In a p-doped material, conversely, there will be a lot of free holes that are the majority carriers and there are negatively charged immobile dopant atoms (see Figure 2.1.1.1). Minority carriers (i.e., holes for n-doped, electrons for p-doped) can only be created in the material due to either photo-generation, thermal excitations or reverse biasing. These minority carriers play a quite important role in the operation of p-n junction solar cells for the generation of the photocurrent.

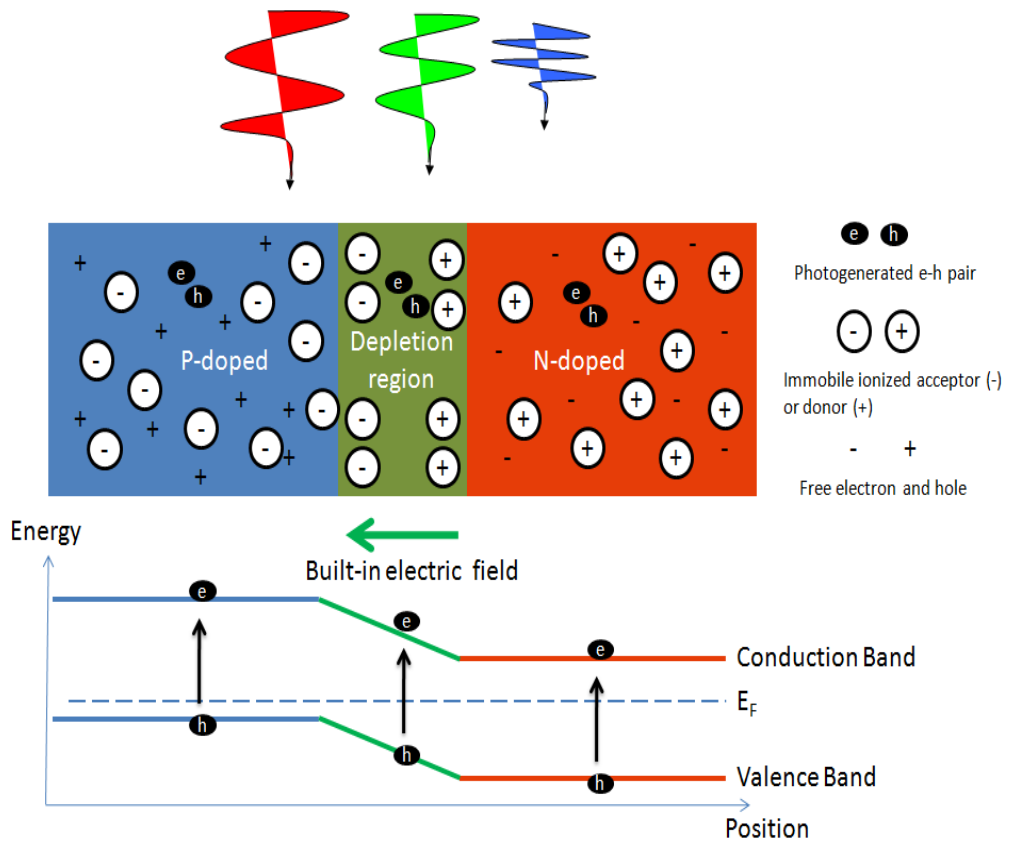


Figure 2.1.1.1 Schematic representation of a p-n junction diode. Material is excited with photons in the visible range. Photogenerated electron-hole pairs are represented. Due to doping of the material resulting immobile ionized acceptors and donors along with free electrons and holes are shown. Energy vs. position schematic shows the alignment of the p- and n-doped regions with depletion region where built-in electric field exists.

Photons having energy greater than the band gap energy will have a chance to be absorbed by the material. As a consequence of photon absorption, in either n-

doped, p-doped or depletion region of the material, electron-hole pairs will be created (see Figure 2.1.1.2). Minority carriers have a limited lifetime in the doped regions, since recombination with a majority carrier is likely to happen. However, in this limited duration of the minority carrier lifetime, minority carriers should be carried towards the junction (see Figure 2.1.1.2 – process 1,2). Diffusion is the dominant process for the motion of minority carriers toward the junction. When a minority carrier reaches the junction (i.e., depletion region), then due to strong built-in electric field in the junction, minority carriers are drifted towards the opposite region where they are already majority carriers (see Figure 2.1.1.2 – process 3-4). When a minority carrier becomes a majority carrier due to drift current in the depletion region, this creates a current in the external circuit as shown in Figure 2.1.1.2 (process 5-6).

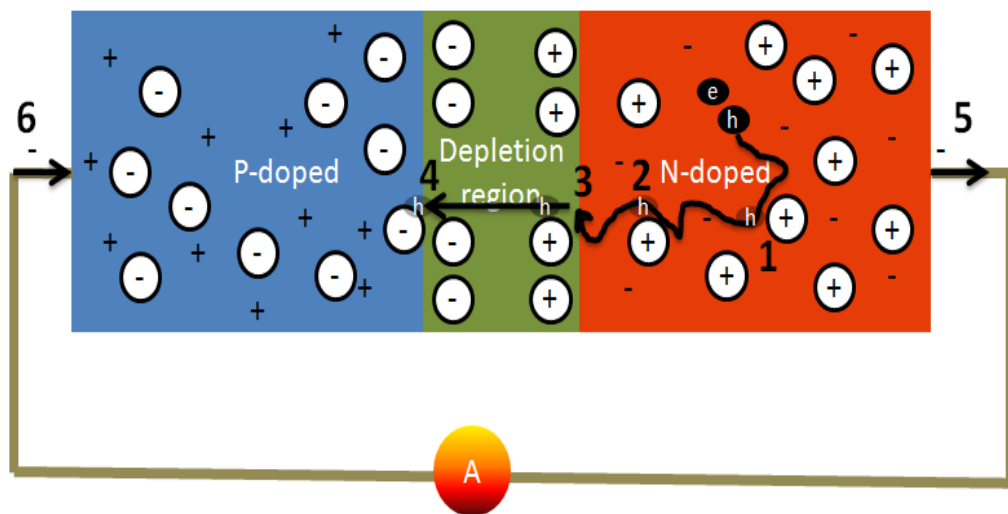


Figure 2.1.1.2 Principle of operation of a solar cell is depicted. Electron and hole pair is created via photo-generation. A minority carrier (e.g., a hole in this case) diffuses in the region (1, 2). If it can reach the junction (i.e., depletion region) after diffusing (3), it is drifted to the other region where it is majority carrier (4). Due to this drift current, in the external circuit, the majority carrier (e.g., electron in this case) is given to external circuit (5) so that it recombines with a majority carrier in the other region (e.g., hole) through external circuit (6).

2.1.2 Important Device Parameters and Characterization Techniques

There are basically four important parameters related to characterization of solar cells: Short circuit current (I_{sc}), open circuit voltage (V_{oc}), fill factor (FF) and power conversion efficiency. Spectral response related parameters as spectral responsivity ($R(\lambda)$) and external quantum efficiency ($EQE(\lambda)$) reflect the important spectral properties of the devices.

Short circuit current, as its name implies, is the current driven in the external circuit in the absence of any load due to photo-generation as shown in Figure 2.1.2.1. I_{sc} is the maximum attainable current that a solar cell can supply. Because any load attached to the external circuit will cause a positive bias on the p-n junction, which will reduce the photocurrent due to increase in the oppositely signed diffusion current in the devices caused from reduced built-in electric field. However, a photovoltaic device cannot be operated under short circuit conditions since no power can be supplied to the external circuit. The parameter, short circuit current, depends on a few factors: optical light power intensity, spectrum of the light, and optical and electrical properties of the device. Short circuit current is a negative current since it flows in opposite direction to the forward biased current (see Figure 2.1.2.1). Since short circuit current is negative, current-voltage characterization of solar cells is undertaken in the fourth quadrant of I-V curve (current in y axis, voltage in x axis) (see Figure 2.1.2.3).

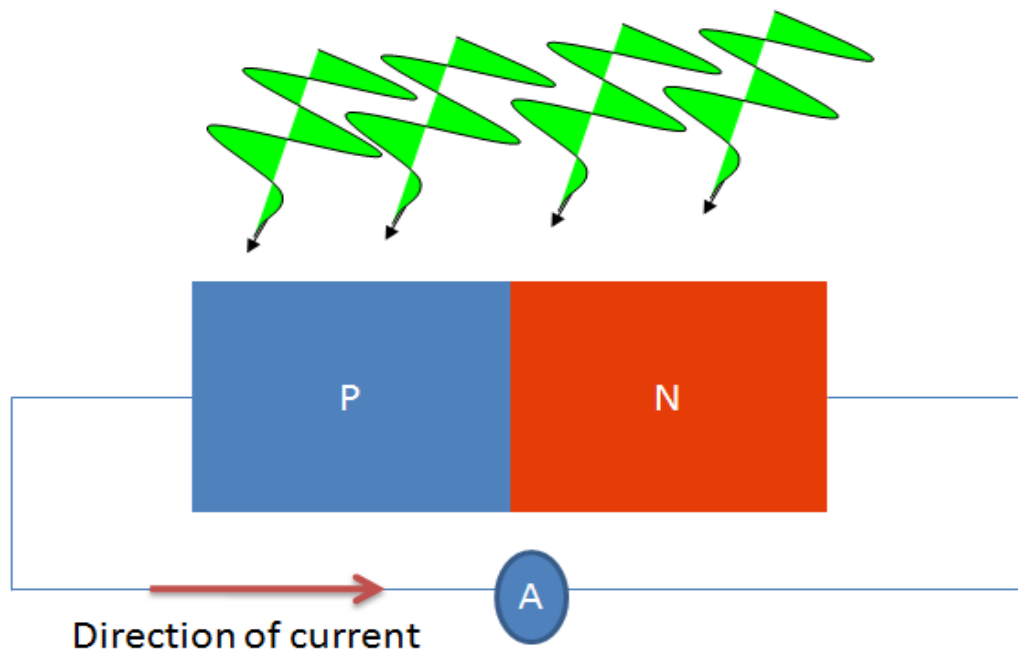


Figure 2.1.2.1 Short circuit current mode of a p-n junction solar cell.

Under light illumination, open circuit voltage is the voltage difference between two terminals of the p-n junction solar cell with no current flow. This voltage build-up across a p-n junction due to photo-generation is explained by the photovoltaic effect. The photo-generated electron-hole pairs that drift in opposite directions across the depletion region due to the built-in field (see Figure 2.1.2.2) creates an electric field of their own through the diode in an opposite direction to the built-in electric field. The resulting reduction of the built-in electric field in the depletion region also increases diffusion currents since barrier against electrons in n-doped region to pass p-doped region is reduced (the same happens for holes in the p-doped region to diffuse into n-doped region). Also reduced built-in electric field decreases the drift currents. Since direction of the diffusion current and drift current is opposite, when drift currents are equalized with the diffusion currents due to increased photo-voltage, net current becomes zero. This condition is called open circuit voltage where as similar to short circuit current case, there is no net power generation. Although short circuit current depends on factors related to optical light intensity, open circuit voltage is more related to internal structure and material

properties of the device. It depends on recombination dynamics and dark current of the device along with the amount of built-in electric field.

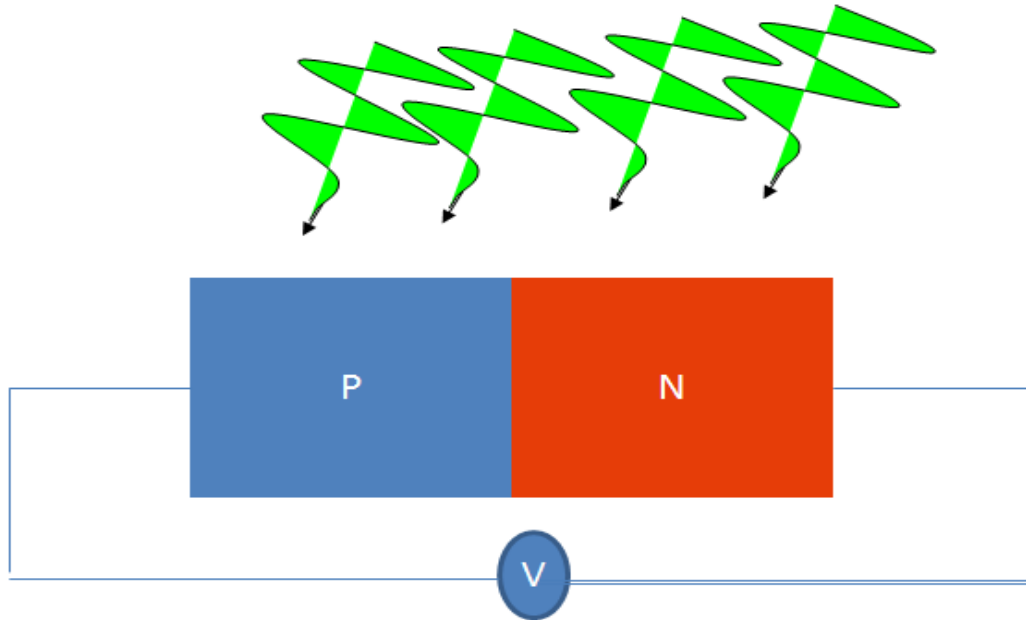


Figure 2.1.2.2 Open circuit mode operation of a p-n junction solar cell.

Fill factor is a measure of maximum power generation capability of a solar cell. Since solar cells are not made up of ideal diodes, current-voltage (I-V) characteristics does not follow ideal diode behavior. Then, fill factor (FF) is the ratio of the area under the square defined by the actual maximum power point (I_{MPP} and V_{MPP}) and the square defined by the ideal maximum power point (I_{SC} and V_{OC}) (see Figure 2.1.2.3). FF is given by (2.1.2.1).

$$FF = \frac{I_{\text{maximum power point}} V_{\text{maximum power point}}}{I_{SC} V_{OC}} = \frac{P_{Max}}{P_{Max\ ideal}} \quad (2.1.2.1)$$

As can be seen from an exemplary I-V curve, I_{sc} , V_{oc} , I_{MPP} , V_{MPP} , P_{Max} and P_{Max_ideal} parameters are all indicated in Figure 2.1.2.3.

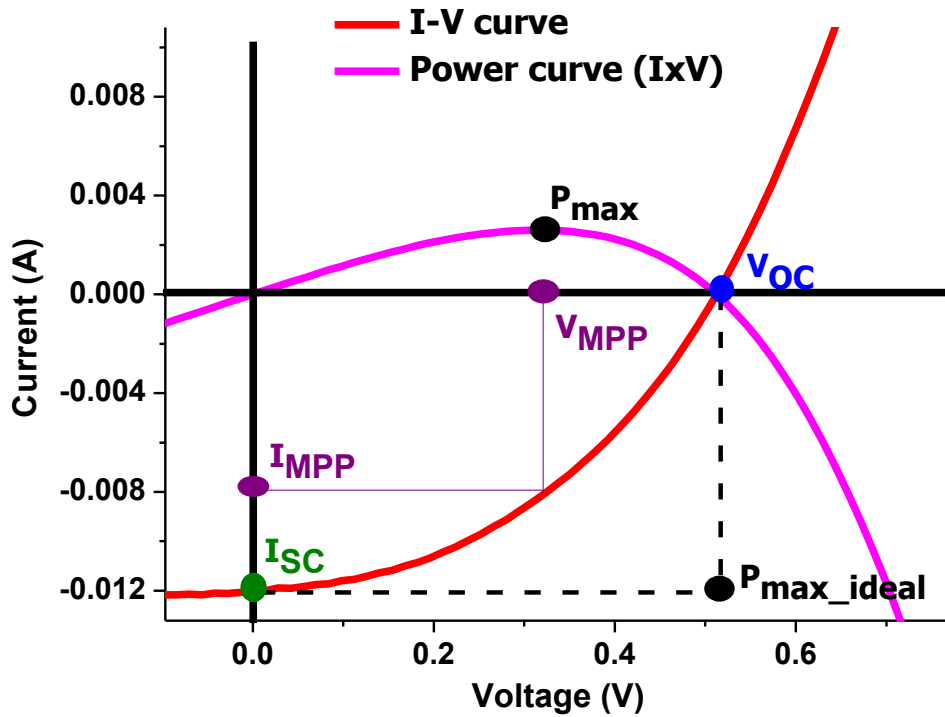


Figure 2.1.2.3 Exemplary I-V curve of a silicon solar cell studied in this thesis. Important solar cell parameters, I_{sc} , V_{oc} , P_{max} , $P_{max\ ideal}$, $V_{\text{maximum power point}}$ and $I_{\text{max power point}}$ are shown on I-V and power – voltage plots.

Power conversion efficiency factor is one of the most important figure-of-merits for solar cells. It is physically defined as the ratio between maximum electrical output power and optical input power as given in (2.1.2. 2).

$$\eta = \frac{P_{\text{maximum power point}}}{P_{\text{optical input}}} = \frac{I_{MPP} V_{MPP}}{P_{\text{optical input}}}$$

(2.1.2. 2)

Power conversion efficiencies are determined using a universal standard called one sun - Air Mass 1.5 Global Solar Spectrum (AM 1.5G), which is the measured spectra of sunlight on earth surface on a bright sunny day with a power intensity of 100 mW/cm^2 . To produce AM 1.5G spectra with desired power intensity, specially designed solar simulators are utilized. These produce wide emission spectra illumination using a Xenon-arc lamp and with the help of optical filters designed specifically for imitating the spectra of sunlight,

AM1.5G conditions can be satisfied. A calibrated solar cell is used to correct the power intensity levels of a solar simulator system.

Another characteristics of a solar cell is the wavelength dependent characteristics the so-called spectral responsivity (in units of A/W) or external quantum efficiency (# of electrons out / # of photons in). These spectral properties can be measured with a spectrometer set-up as shown in Figure 2.1.2.4. A monochromator picks desired emission wavelength from the wide emission spectra of the Xenon lamp. A lock-in amplifier works in harmony with the optical chopper in order to reduce the noise due to any light in the environment by making modulated optically chopped measurements. We also measure the optical power levels in the measurement spectrum via an optical powermeter by placing the powermeter detector instead of the sample. Spectral responsivity can be obtained by simply dividing the measured currents by the measured spectral optical power levels. There is a strong relation between the spectral responsivity ($R(\lambda)$) and the external quantum efficiency (EQE). We can calculate spectral EQE using (2.1.2. 3) where $h\nu$ is the photon energy and e is unit charge.

$$EQE(\lambda) = \frac{R(\lambda)}{\lambda} \frac{hc}{e} = \frac{R(\lambda)}{\lambda} 1.24 \mu m W/A$$

(2.1.2. 3)

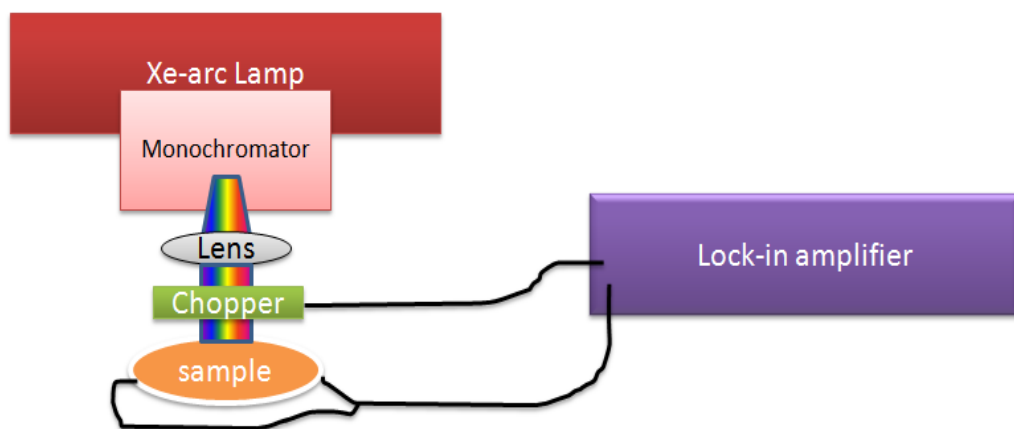


Figure 2.1.2.4 Measurement set-up for wavelength dependent responsivity and external quantum efficiency.

Figure 2.1.2.5 shows an exemplary spectral EQE of a silicon p-n junction solar cell. In the visible region, this device exhibits a high EQE. However, at both ends of the spectra, EQE tends to decrease. The decrease in UV part is due to strong absorption of the photons close to the top surface of the device so that these created e-h pairs cannot contribute to the drift current since minority carriers recombine at high surface trap states. In the IR region, EQEs are again reduced due to decreasing absorption coefficient of silicon.

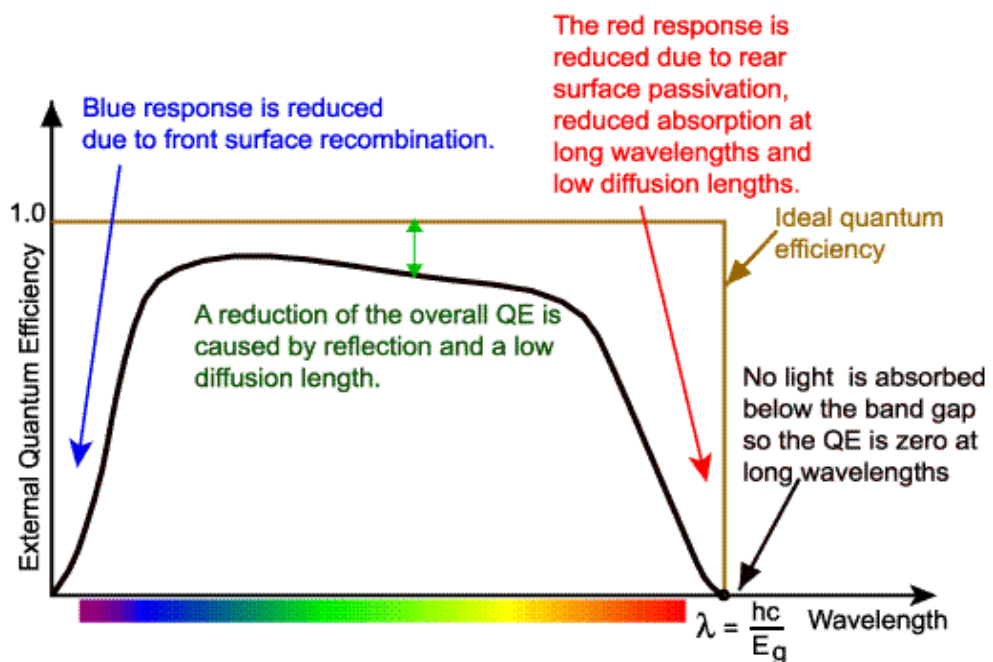


Figure 2.1.2.5 Exemplary external quantum efficiency plot for a silicon based solar cell. EQE is low at both ends of the spectrum. In the UV part, it is low due to poor utilization of electron-hole pairs close to the surface. In the IR part, it is low due to poor absorption of silicon with back contact problems. [16]

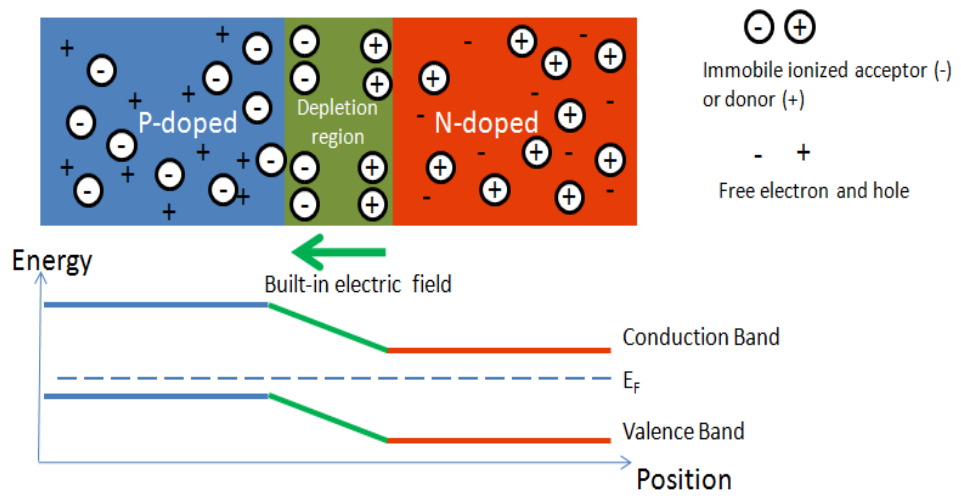
2.2 Semiconductor Light Emitting Diodes

2.2.1 Principles of Operation

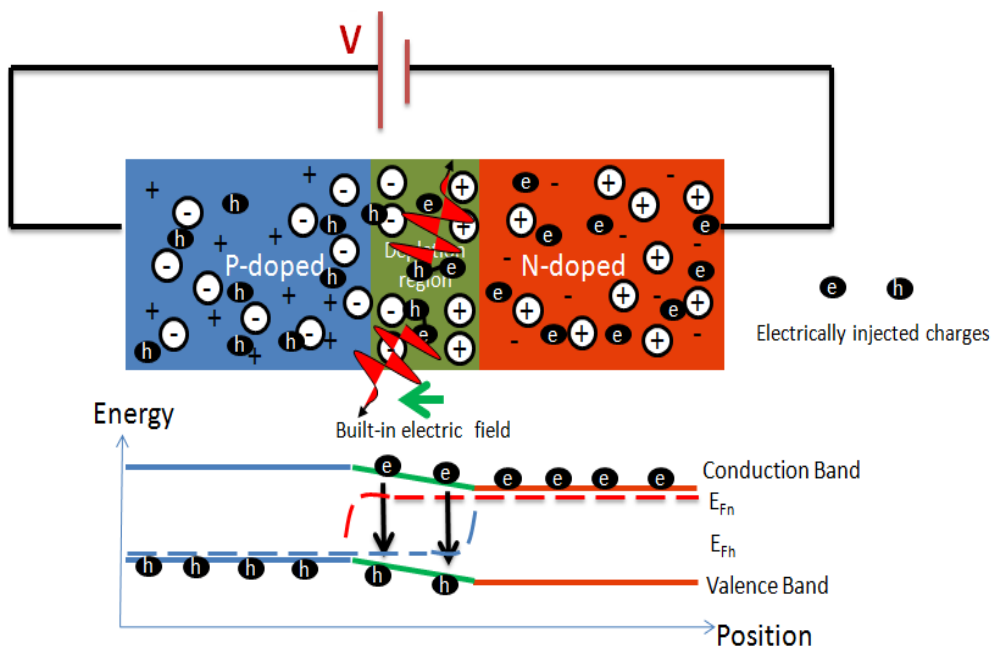
Most of the direct band gap semiconductor materials having band gap energies matching with the electromagnetic spectrum of light (i.e., UV to IR) are known to possess fluorescence properties. When excited with a light source having

photon energy larger than the band gap of the semiconductors, electron-hole pairs are photo-generated. Due to radiative recombination properties of semiconductor materials, these electron-hole pairs can recombine to give their excess energy in the form of photon emission. Electroluminescence (EL) is the principle of operation of light emitting diodes where electrically injected charges are combined to form electron-hole pairs so that radiative recombination results in emission of photons. Conversely to solar cells, where photo-generated electron-hole pairs are extracted into external circuit, here in LEDs electrons and holes are injected into the junction and subsequently, they recombine to emit photon.

The main principle of operation of LEDs is summarized schematically in Figure 2.2.1.1. Under zero bias, a p-n junction diode has a structure and energy diagram as shown in Figure 2.2.1.1 (a). However, if we apply a positive forward bias, charge carriers will be injected from respective contacts (i.e., electrons from n-doped region and holes from p-doped region) (see Figure 2.2.1.1 (b)). Those charge carriers will perturb the carrier balance in doped regions so that quasi Fermi levels will be formed (i.e., E_{fn} and E_{fp}). Injected carriers will diffuse in the material towards the junction. Built-in electric field is reduced due to forward bias, then charges will have less hindrance to move through the junction. Some of the electrons and holes will combine together to form bound electron hole pairs so that they will either radiatively or nonradiatively recombine depending on the internal luminescence properties of the material.



(a)



(b)

Figure 2.2.1.1 (a) A p-n homojunction diode under zero bias is shown with free electron and holes in n- and p-doped regions, respectively. (b) A p-n homojunction diode under forward bias is shown. Built-in electric field is reduced. Diffusion current increases. Quasi-Fermi levels form due to injection. Formed electron-hole pairs can emit light (i.e., electroluminescence).

Today, LED technology utilizes direct band gap epitaxially grown compound semiconductor materials such as GaAs, AlGaAs, GaP and AlGaInP for IR and red emitting diodes; GaN, InGaN and GaAsP for yellow and green emitting diodes; InGaN, ZnSe and AlGaN for blue and UV emitting diodes. These

materials are generally grown by metalorganic chemical vapor deposition technique which is quite expensive and slow compared to deposition methods of colloidal particles and organic polymers and molecules.

2.2.2 Organic Light Emitting Diodes

There are alternative approaches to all inorganic LEDs such as organic light emitting diodes (OLEDs), which utilize luminescent and conductive organic materials. OLED technology provides cheaper and versatile devices with ease of fabrication techniques. Conjugated polymers which were invented in late 70's have undergone many developments in the last decades and a new technology based on these materials emerged. Their inventors were awarded with a Nobel prize in 2000.

Due to π - π^* bond stacking, band-like electronic and optical properties are observed for conjugated polymers (see Figure 2.2.2.1). Formation of the highest occupied molecular orbital (HOMO) and the lowest occupied molecular orbital (LUMO) resembles valence and conduction band properties of the inorganic semiconductor materials. The energy difference between HOMO and LUMO is the effective band gap of the polymer. Although their electrical properties are poorer as compared to mono-crystalline highly doped semiconductor materials, these organic counterparts provide advantages such as ease of processing methods with novel mechanical properties, which make them very promising materials for future optoelectronic applications. Solar cells, light emitting diodes, lasers and transistors made up of all organic means have been already shown. [17, 18, 19, 20]

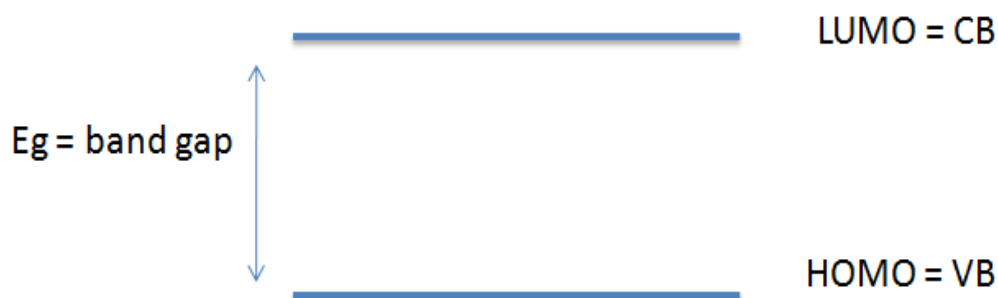


Figure 2.2.2.1 A typical band diagram of a conjugated polymer where LUMO level corresponds to conduction band and HOMO level to valence band.

The similar principle of operation for inorganic LEDs also applies to OLEDs, which simply relies on the electroluminescence under current injection. The whole visible spectrum can be covered with different conjugated polymer types having different band gaps. These novel semiconductor materials have been observed to make good electrical contacts with metal interfaces. Although charge mobility in these materials are not so fast, this does not create a main drawback for LEDs; however, this might be a problem for laser applications where very fast electron-hole pair formation is required. A side note should be given here that, in the context of organic materials, electron-hole pairs are not articulated much, since organic materials are known to have strongly bound excitation carriers, the so-called excitons (i.e., Frenkel excitons) with binding energies more than a few hundreds meV. A polymer based OLED can be designed in its simplest form in a single layer architecture as shown in Figure 2.2.2.2. Generally low work function metals such as Ca and Mg and their combinations with other relatively low work function metals Ca/Al, Mg/Ag, etc, are used to make top contacts. These top contact serve as cathode so that electrons are injected. The bottom electrode is chosen to be transparent since light extraction to external world should take place. Most popular transparent conductive oxides (TCO) are indium tin oxide (ITO) and fluorine doped tin oxide (FTO). TCOs are used as anodes (i.e., hole injection). ITO is far most popular TCO since ITO provides a better work function match with commonly used polymer's HOMO levels for hole injection. Injected electrons and holes are

combined in the polymer to form excitons, subsequent to exciton formation emission of a photon takes place.

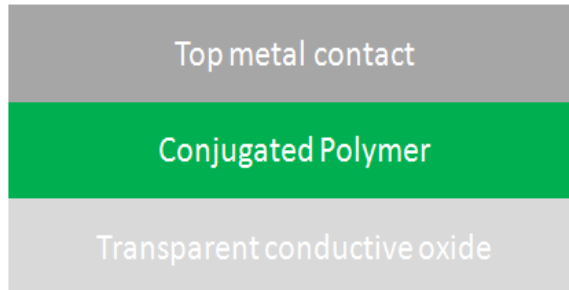


Figure 2.2.2.2 The simplest device design for polymer based OLED. Top contact is used as cathode and bottom contact is used as anode.

We have drawn the band diagram of the simplest polymer OLED design as shown in Figure 2.2.2.3 to understand the EL properties of the devices. At zero bias, there will be no potential difference between the anode and cathode, and charges cannot be injected (Figure 2.2.2.3 (a)). At increased forward bias levels, we will first reach a threshold voltage after which injection will start immediately (Figure 2.2.2.3 (b)). At higher bias levels, charge could be injected into polymer through tunneling from cathode and anode (Figure 2.2.2.3 (c)). Injected charges would then meet each other to form excitons in the polymer.

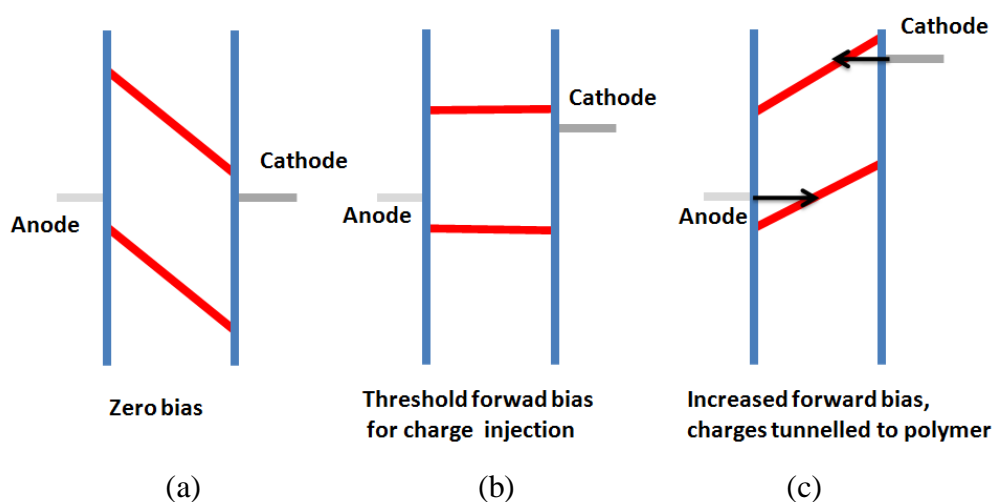


Figure 2.2.2.3 Three different bias conditions for simple device design of sandwiched polymer layer between anode and cathode. (a) At zero bias charges cannot be injected. (b) At threshold

forward bias level, charge injection becomes possible (immediately after this bias level). (c) At bias levels greater than threshold, charge injection can take place via tunneling.

For polymers emitting in red, yellow and green, the offset energy between anode and cathode work function is not significantly high, so that injection can be still effectively achieved via tunneling. However, for large band gap blue emitting polymers, energy offsets between work function of the contacts and HOMO or LUMO levels of the polymer may reach about 1 eV, which significantly reduces the device efficiencies due to poor charge injection. Better designs are required to make charge injection more efficient and balanced; also, charge confinement in the active layer would help to form more excitons in the active emission layer. Use of injection, transport and blocking layers are ideally utilized in a more advanced design as shown by Figure 2.2.2.4. In this kind of an OLED design, quite efficient devices can be obtained. Electron and hole injection layers reduce the mismatch between metal and the first organic layer. Injected carriers are then transferred to transport layers which can have high conduction properties for a given charge carrier type. Carrier blocking layers help to block the other type of charge carrier due to large difference in HOMO or LUMO levels between the active layer and the block layer. When charge carriers are injected into polymer active emission layer, excitons will be formed. Exciton formation probabilities are increased because of blocking layers providing confinement of charges in the active layer.

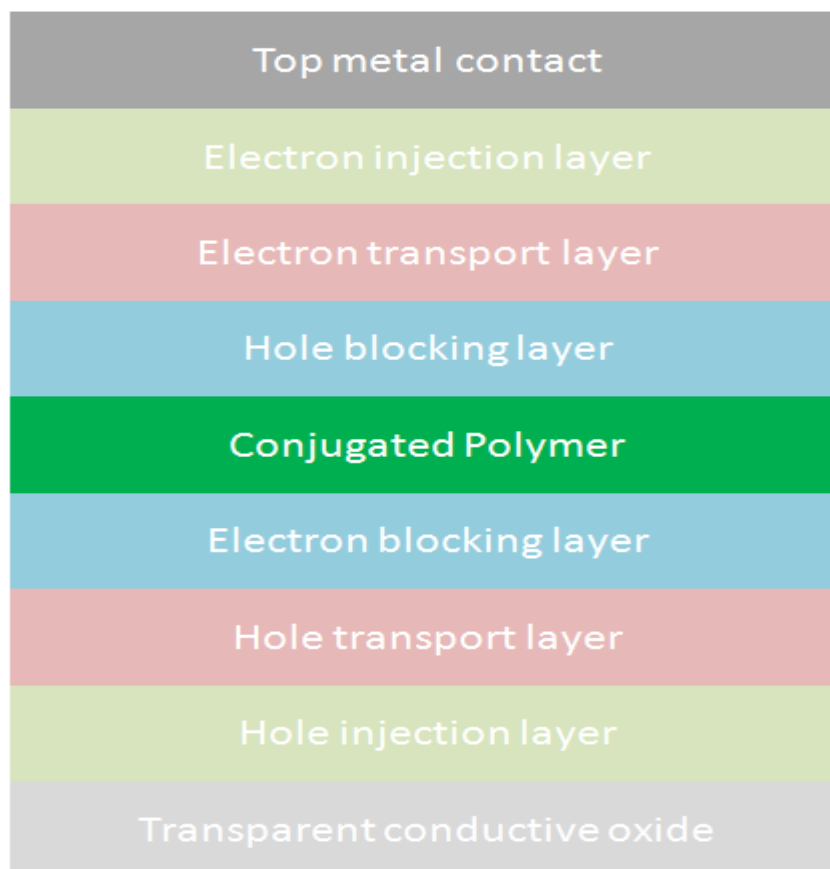


Figure 2.2.2.4 An advanced design for an efficient OLED.

Except conjugated polymers, small organic fluorescent molecules can also be used as the active emitting layers. Most of the injection, transport and blocking layers consist of small organic molecules, which are generally coated via thermal evaporation techniques. When these molecules are heated to moderate temperatures such as 300- 400°C under vacuum, molecules tend to evaporate without breaking into atoms so that controlled films can be easily achieved. However, solution processing is also possible, which is quite inexpensive, and an easy method of spin coating or similar cheap and straightforward methods are utilized. One of the vital advantages of organic materials is that they can be coated on flexible substrates, allowing for roll-to-roll processing, since they have ductile material properties unlike crystalline inorganic materials. In the future, wearable devices could become possible with the developments in organic optoelectronics.

2.2.3 Important Parameters and Characterization

Light emitting diodes are mainly characterized with several measurement techniques. Electrical properties are mainly studied with current-voltage (I-V) measurements. Luminosity-current (L-I) measurements can be made to understand the relation between injected current levels and number of output photons to specify the stable operation regions. Electroluminescence (EL) spectrum measurements are also performed to observe the EL spectra of the devices under different bias and current levels. Some important device parameters are turn-on voltage, luminous efficiency (LE), and external quantum efficiency of the devices.

An exemplary I-V curve of an OLED is shown in Figure 2.2.3.1. I-V data is useful to understand the electrical properties of the LEDs since directly turn-on voltage and injection related properties can be analyzed through I-V curves. A parameter analyzer is typically utilized to measure the I-V relation of the diode.

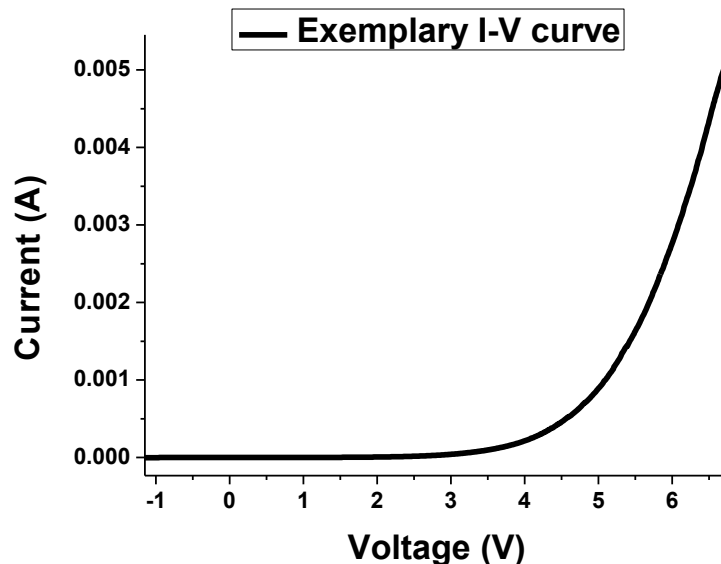


Figure 2.2.3.1 An exemplary I-V curve of an OLED.

In order to determine the L-I (luminosity-current) property of a LED, optical power meter can be used. We also utilize an integrating sphere to collect emission of the LEDs in all direction An example L-I data of an OLED is shown Figure 2.2.3.2. L-I data is useful to understand the operation limits of the devices. For example, after driving higher current through a device, L-I curve does not follow a linear relation due to heating problems of the LEDs, which can severely reduce the efficiencies.

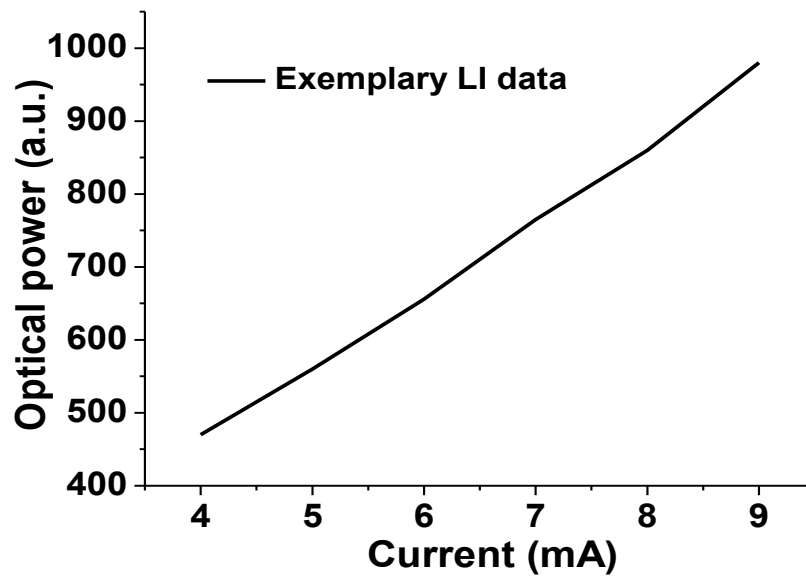


Figure 2.2.3.2 An exemplary LI data of an OLED.

Another important characterization is the measurement of EL spectrum. An exemplary EL spectrum of an OLED is shown in Figure 2.2.3.3. EL spectrum can be easily measured using a charge-coupled-device (CCD) integrated spectrometer (Ocean Optics 2000) connected to an optical fiber, which is attached to the integrating sphere where sample is electrically excited. EL spectrum is quite important since one of the most important specifications of the LEDs is their EL spectra. EL data can be taken at different charge injection levels to check spectral stability of the devices.

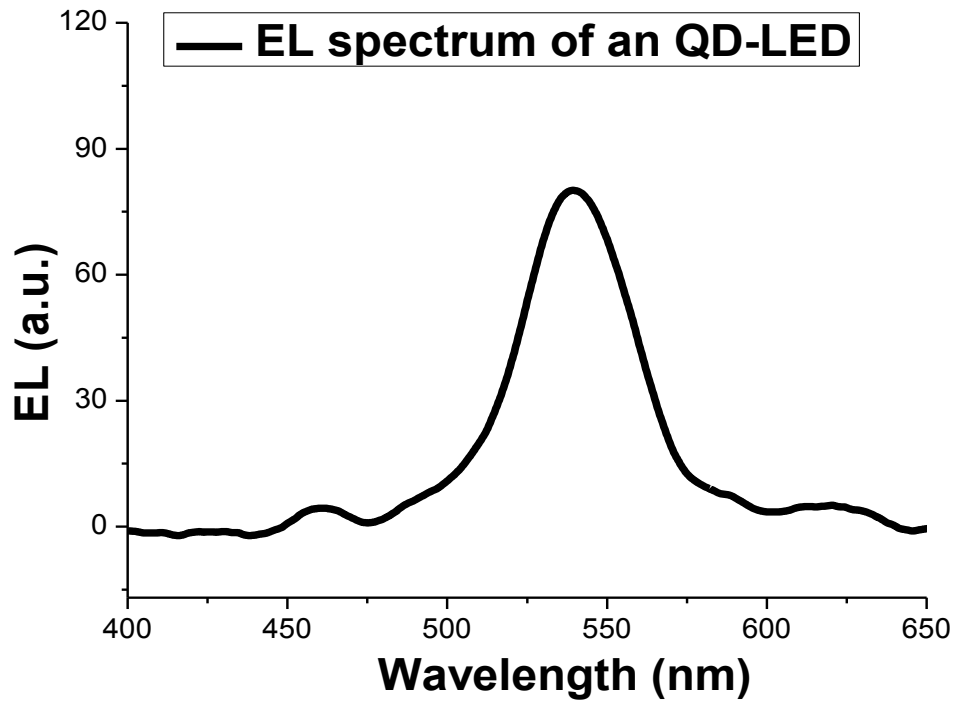


Figure 2.2.3.3 An EL spectrum of a quantum dot based LED.

The important parameters of external quantum efficiency (EQE) and luminous efficiency (LE) are calculated since they give valuable information about the electrical and optical quality of the devices. External quantum efficiency is defined as the ratio of output photon number to electrically injected electrons. From the measurement of L-I curve, we can easily calculate EQE using (2.2.3.1) where $h\nu$ is the photon energy and e is the unit charge.

$$\eta_{EQE} = \frac{\frac{P_{output\ photon}}{h\nu}}{\frac{I_{input}}{e}}$$

(2.2.3.1)

Another metric is luminous efficiency, in units of lm/W, which gives the relation between perceived light power by a human eye and electrical input power given by (2.2.3.2). Here $V(\lambda)$ is the human eye sensitivity function, $P(\lambda)$ is the optical output power and $P_{electrical}$ is simply $I \times V$ (electrical input power).

$$LE = \frac{683 \frac{lm}{W} \int V(\lambda) P(\lambda) d\lambda}{P_{electrical}}$$

(2.2.3 2)

2.3 Experimental Methods

2.3.1 Fluorescence Lifetime Spectroscopy

Time resolved fluorescence spectroscopy is a useful tool to investigate lifetime decay kinetics of fluorescent materials. The results obtained via time resolved spectroscopy is quite informative for wide range of applications in physics, biology and chemistry. Since excited state decay kinetics are quite sensitive to molecular level interactions and dynamics, many different phenomena (e.g. rotation, diffusion, molecular conformations, molecular binding, energy transfer, charge transfer, etc.) can be directly observed through fluorescence decay curves. Today, fluorescence lifetime spectroscopy is also used for bio-imaging purposes. [21]

In our laboratory, we use a time correlated single photon counting (TCSPC) system having a time resolution down to 4 ps (PicoHarp 300) integrated with a picosecond pulsed laser with an output photon energy of 3.307 eV driven by a driver module (PDL-800 series) capable of delivering laser pulses with 80 MHz repetition rate. The system utilizes a fast photo multiplier tube (PMT) (Hamamatsu H5783 series) to resolve lifetimes on the order of tens of picoseconds. Also, we integrate a close cycle Helium cryostat with this system to make temperature dependent studies. The whole system with its complementary components is shown in Figure 2.3.1.1.

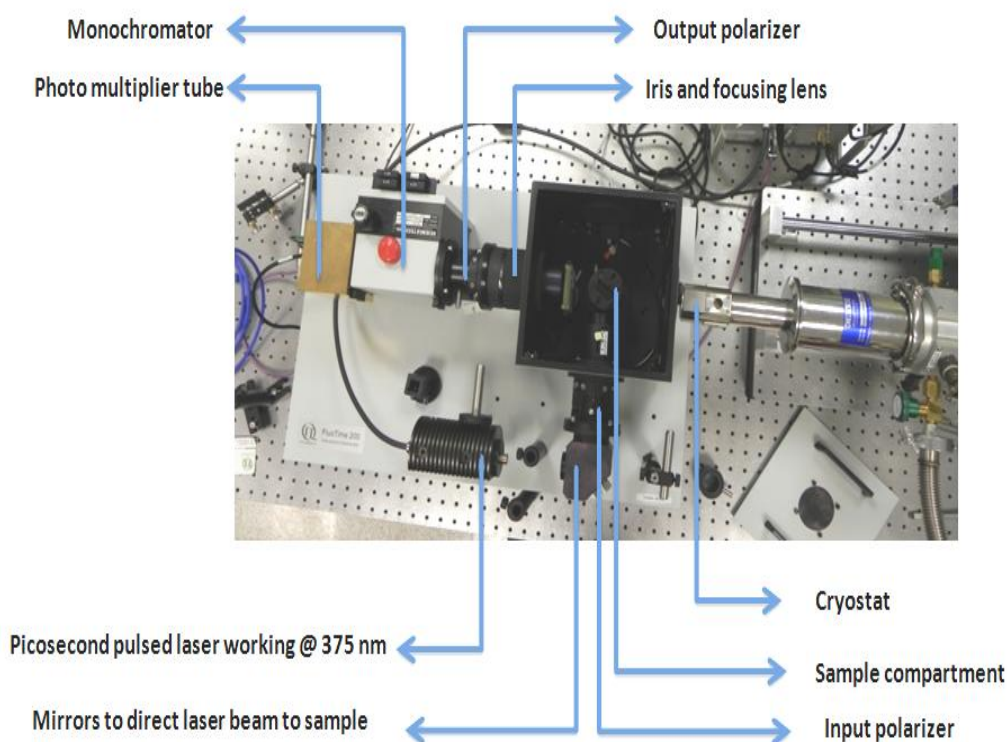


Figure 2.3.1.1 FluoroTime 200 time resolved fluorescence spectroscopy system used for time resolved measurements in this thesis.

2.3.2 Steady State Optical Characterizations

Steady state optical characterizations have been performed using a fluorescence spectrometer (Cary Eclipse and Fluorolog 3) for photoluminescence measurements and a UV-Vis and UV-Vis-NIR spectrometers (Cary 100 and Cary 5000, respectively) for absorption measurements.

Steady state fluorescence spectroscopy also gives a lot of information both on the material properties and dynamics taking place at nano-scale due to high sensitivity of the photo-physical properties of the materials to even small changes in the molecular level. The main principle of operation of these tools rely on spectrally selective excitation of the samples. Observation of emitted or transmitted signal at the detector end give us PL or absorption information,

respectively. Instrumentation of a spectrofluorometer consists of several different components: Light sources, monochromators, optical filters, detectors, and polarizers. Light sources generally are made of Xenon and Mercury lamps (e.g., Xe flash or arc, Xe-Hg arc, high-pressure Hg lamps, etc.). Sometimes lasers or LED sources can also be utilized. Monochromators use diffraction gratings to disperse wide spectrum of light (i.e., white light) to select the output spectrum. Issues related to monochromators are dispersion efficiency, stray light mixing and harmonic light suppression. Dispersion efficiency is related to spectral narrowness of the output light. FWHMs can be reduced by placing smaller width slits on the entrance and exit ports of the monochromator. However, utilization of smaller slit widths yield reduced excitation signals which could decrease the signal to noise ratio of the measurements. Stray light mixing is an unwanted light spectrum that is unintentionally coupled to the output of the monochromator. Gratings work on the principle of light diffraction, however higher order harmonics of the desired emission wavelength may couple to the output of the monochromator. Due to this problem, utilization of spectral filters are quite important. Most of the spectrometers include built-in filters to decouple higher order harmonics from the output.

The mostly used measurements are photoluminescence (PL), photoluminescence excitation (PLE), absorption and transmission. PL measurements are made with fluorescent samples at a chosen excitation wavelength, emission spectrum of the material is recorded. PLE measurement is carried out by specifying an emission wavelength and recording the excitation spectrum while varying the excitation wavelength. Absorption measurements are made using calibrated spectrometer detectors since excitation light after the sample is compared with the excitation light without the sample.

2.3.3 Material and Structural Characterizations

Dealing with nanoscale materials and devices involves frequent utilization of imaging techniques such as scanning electron microscopy (SEM), transmission electron microscopy (TEM) and atomic force microscopy (AFM). These imaging methods help a lot to understand and characterize many properties of the materials and devices.

SEM is one of the most useful tools since it is more straightforward to use among other techniques, but it may provide as much information as others can do. General surface topography, nanoscale structures and sub-micron particles can be easily imaged with a resolution down to tens of nanometers. Also integrated energy dispersive x-ray spectroscopy equipment, SEM becomes more powerful since elemental analysis of the imaged materials can be achieved.

TEM is one of the most difficult techniques among them, however the highest resolution down to a few Angstroms can be achieved. Crystalline structures and materials can be easily characterized in terms of their material and structural properties. Again, energy dispersive spectroscopy can be integrated to TEM, which enables us to understand more on the elemental distribution of the nanoscale materials.

AFM is another alternative approach, which is useful for surface topography imaging. However, many different modes developed for AFM could be employed to image and characterize different properties of the materials. For example, phase imaging, which deals with the phase changes of the AFM tip while tapping on the surface, can give material information since tapping of the tip involves interaction with the material. Kelvin probe force microscopy mode of AFM, for example, can reveal electrical properties of the materials on the surface such as conduction and valence band offsets from vacuum level.

2.3.4 Fabrication Techniques

In this thesis, since we have worked with quantum dot hybrid material systems, we utilized solution processing methods typically. Spin coating, drop casting and layer-by-layer assembly can be applied to coat solution processable materials depending on the requirements. Spin casting is very fast, but control over thickness and film uniformity is moderate. Drop casting is the fastest, but control over film properties is quite poor. Layer-by-layer assembly enables the best control for film formation and thicknesses, however it is quite slow.

Another mostly utilized technique is the physical vapor deposition (PVD). Most metals having moderate boiling points can be formed in thin films using PVD technique. High boiling point materials such as W and Mo can be used as crucibles for metals to be evaporated. Under high vacuum conditions, the crucibles, or boats, are heated with high current passage through the boat material. The metal inside the boat becomes molten and starts to evaporate under vacuum. The rate of evaporation can be tuned via changing of the current over the boat, monitored with quartz micro crystal balance sensors. Thin films ranging from tens of nanometers to hundreds of nanometers can be easily coated.

Chapter 3

Semiconductor Quantum Dot Nanocrystals

3.1 Introduction

Semiconductor nanocrystal quantum dots (NQDs) are unique luminescent materials exhibiting quantum confinement effects due to their small sizes on the order of a few nanometers. They are called nanocrystals because they show crystalline material properties. They are also called quantum dots, since quantum mechanical modeling of three dimensionally confined quantum dot model agrees well with the observed properties of NQDs. There are more than one types of NQDs, which are distinguished by their growth techniques. These techniques include growth of nanocrystals in inorganic matrices (e.g., glass, zeolites, ionic crystals, etc.) and use of epitaxial growth techniques as molecular beam epitaxy (MBE) or metalorganic chemical vapor deposition (MOCVD). [22] However, the most popular method to grow NQDs is the means of colloidal chemistry. Colloidal synthesis provides an easy method as compared to other alternatives, also together with its increased control over the growth kinetics. High quality semiconductor NQDs with a wide range of materials can be grown using the colloidal routes. Other than semiconductors, nanocrystals of metals and insulating materials could also be performed using colloidal synthesis.

Synthesis of nanocrystals using colloidal chemistry roots back to 80's, but the quality of the synthesized nanocrystalline materials were poor at those times in

terms of their optical (e.g., photoluminescence quantum efficiency) and material properties (e.g., monodispersity, stability). However, in the beginning of 90's, an optimized way of synthesizing NQDs in high boiling point coordinating organic solvents has been realized, which has led to further developments in the field of semiconductor nanocrystals. [23] This new approach provided an excellent control over the growth of NQDs due to stoichiometry between growing inorganic nanocrystals and stabilizing organic solvent. The organic solvent also played different roles besides serving as the matrix of synthesis. The organic solvents attaches onto the surfaces of grown nanocrystals so that they become ligands (i.e., surfactants) of the NQDs (see Figure 3.1.1 for a schematic showing CdSe NQDs with surface ligands attached to Cd atoms). Surface ligands are important since they passivate the surfaces of NQDs in order to reduce trap states. Unless these trap states are passivated, luminescence properties are degraded significantly yielding inefficient NQDs. Also, utilization of high boiling point solvents has enabled the growth of crystals at elevated temperatures like 200 - 300 °C so that crystal quality could be considerably increased. Another property imposed by the organic ligands is that NQDs become soluble in different various solvents by the help of their ligands, so that cheap and easy solution processing techniques could be employed for diverse applications of NQDs.

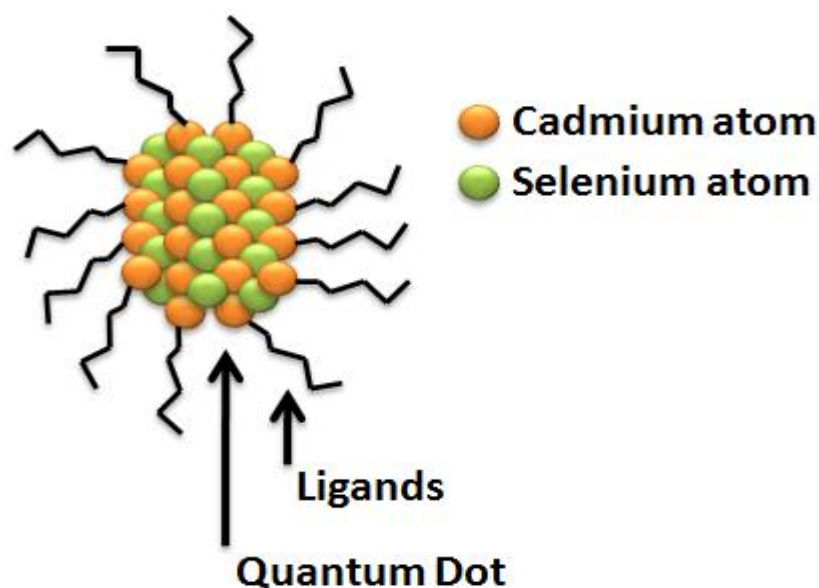


Figure 3.1.1 Colloidally synthesized nanocrystal quantum dot with surface passivating ligands attached to surface Cd atoms are shown representatively.

First NQDs, which were synthesized with colloidal chemistry techniques, were generally cadmium chalcogenide based (i.e., CdSe, CdTe, CdS) II-VI materials. These NQDs were exploited and optimized extensively. Besides, III-VI and IV-VI materials have been also synthesized and optimized for colloidal means. The material system represents a great importance, since emission properties depend on the bulk energy band gap plus additional energy quantization caused due to quantum confinement effects (see Chapter 3.2). As a result, the starting bulk band gap energy determines the smallest possible photon energy that can be emitted by NQD. As a result, NQDs emit at shorter wavelengths than their bulk counterparts. For example, Cd chalcogenide based compound semiconductors have bulk band gaps in NIR so that their NQDs have band gap energies covering the whole visible region (i.e., red to some part of the blue). Another material system of Pb chalcogenides (i.e., PbS, PbSe), on the other hand, have different properties of emission, since bulk band gap is in IR so that even NQDs of the Pb based materials emit in IR or NIR regions. Recently, heavy metal free (i.e., Cd and Pb free) NQDs have gained importance due to toxicity problems of the heavy metal containing NQDs. Compounds such as CuInS, InP and Zn based

chalcogenides are being shown as the candidates to replace heavy metal containing NQDs.

In the first era of NQDs, they consisted of single types of compounds such as only CdSe, CdTe and CdS, which today are called only core NQDs. However, it was realized that growing inorganic shells made up of different compounds around the core NQDs using the same colloidal approaches can enhance optical (e.g., quantum yield) and material properties (e.g., environmental stability) significantly. These type of NQDs are now known as core/shell structures. Generally, inorganic shells utilize compound materials having larger band gap energies than the band gap energy of the core NQD to confine excitons better in the cores. By confining the excitons mostly in the cores, it is aimed to prevent any disturbing effects of the external media around NQDs through surface interactions that may possibly degrade the optical qualities. Again, to provide stability and solubility, organic ligands reside on the surfaces of the inorganic shells. For example, most popular core/shell nanocrystal is CdSe/ZnS where ZnS shells have a much greater band gap energy than CdSe has, so that photogenerated excitons can be confined fully in the nanocrystal (when three or more monolayers of shell ZnS is used), leading to very high quality NQDs. These exciton confining core/shell structures are called type I NQDs due to band alignments, as can be seen in Figure 3.1.2. Also, it is possible to synthesize type II like NQDs. As also shown in Figure 3.1.2, CdTe/CdSe forms a type II like band alignment; these NQDs show unique properties such separation of the photo-generated charges inside the quantum dot along with elongated exciton lifetimes.

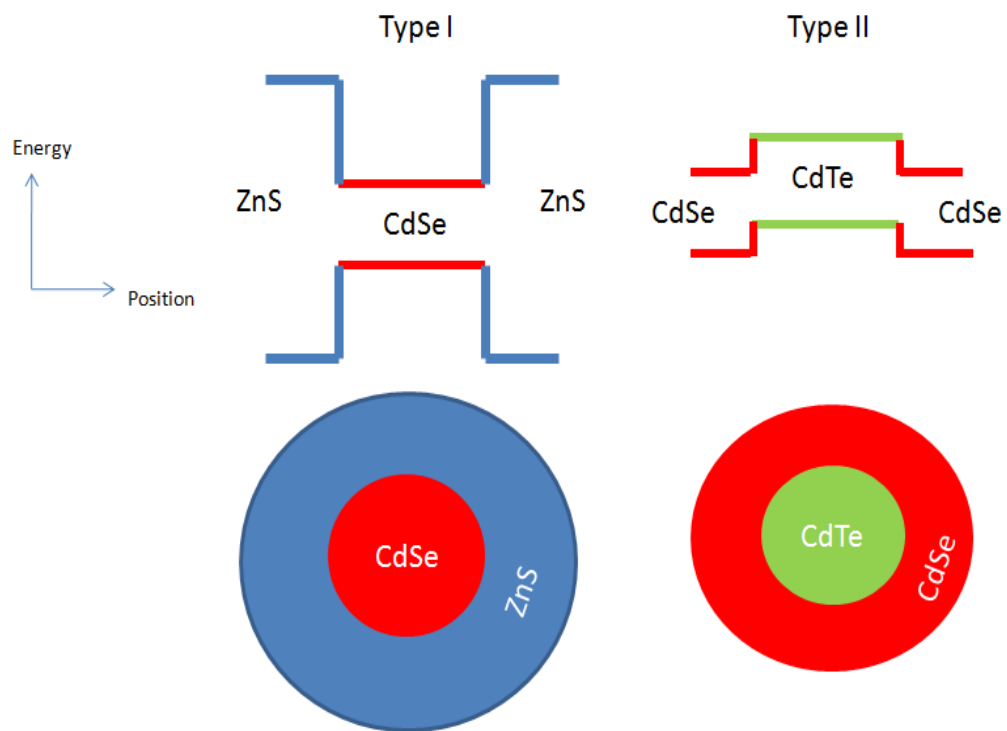


Figure 3.1.2 Schematical examples of type I and type II core/shell NQDs.

3.2 Quantum Mechanics behind Nanocrystal Quantum Dots

As we have mentioned in section 3.1, optical and electrical properties of NQDs can be directly predicted by quantum mechanical means. Even a simple model in quantum mechanics called ‘particle in a box’ model provides a deeper insight on the properties of NQDs. Quantum confinement is more pronounced for the cases when the spatial extent of an electron-hole pair in a semiconductor is comparable or larger than the actual size of the material. Spatial extent of a bound electron-hole pair is called exciton Bohr radius, which could become larger than the radius of a small nanocrystals so that confinement effects can be easily observed. (3.2. 1) gives the exciton Bohr radius of a material having a

dielectric constant of ϵ , a rest mass of the electron as m , an effective mass of the particle as m^* and Bohr radius of hydrogen atom as r_0 .

$$r_B = \epsilon \frac{m}{m^*} r_0 \quad (3.2.1)$$

Generally, Bohr radius of an exciton is on the order of ten nanometers. For example, CdSe has an exciton Bohr radius of 6 nm. [24]

Assuming a small particle lies in a box of infinite potential, we can calculate the available energies that the particle can attain under these conditions using quantum mechanics. ((3.2.2) indicates the infinite potential barrier exists on the boundaries of the particle, which has a size of r_p .

$$V(r) = \begin{cases} 0, & \text{if } r < r_p \\ \infty, & \text{if } r \geq r_p \end{cases} \quad (3.2.2)$$

We can write down the time independent Schrödinger equation as in (3.2.3), where $\psi(r)$ is the wavefunction (eigen function) and E is the energy of the particles (eigen energy).

$$-\frac{\hbar^2}{2m} \frac{\partial^2 \psi}{\partial r^2} + V(r) \psi(r) = E \psi(r) \quad (3.2.3)$$

If we think of the particle as a sphere in three dimension, infinite potential barriers affect the particle in every direction equally. Then, we can use the separation of variables to write down the time independent Schrödinger equation in a single direction as (3.2.4).

$$-\frac{\hbar^2}{2m} \frac{\partial^2 \psi}{\partial x^2} + V(x) \psi(x) = E \psi(x) \quad (3.2.4)$$

By inserting the boundary conditions given in (3.2.6).

$$\psi(x) = 0, \quad \text{if } x = r_p \text{ and } x = 0 \quad (3.2.5)$$

We obtain a solution for the wave function of the particle (i.e., electron or hole) as given in (3.2.6).

$$\psi(x) = A \sin(kx) + B \cos(kx) \text{ and } k = \sqrt{\frac{2mE}{\hbar^2}} \quad (3.2.6)$$

Using the boundary condition, we find with possible k values as in (3.2.7).

$$k = \frac{n \pi}{r_p}, n \text{ is an integer} \quad (3.2.7)$$

So, we obtain the possible energies for the particle in an infinite potential barrier as in (3.2.8).

$$E_n = \frac{\hbar^2}{2m} \left(\frac{n \pi}{r_p} \right)^2, n \text{ is an integer} \quad (3.2.8)$$

As a result, energy values that a particle (i.e., electron or hole) can take becomes quantized by an integer value n. Also, these quantized energies depend on the size of the particle, which is r_p . As the size of the particle is decreased, the possible energy levels are increased and separated more. This quantization of the energy levels as the particle size is reduced is called quantum confinement effect. Figure 3.2.1 shows schematically the effects of quantum confinement for a NQD with its bulk counterpart. The size of the bulk material is much greater than the exciton Bohr radius so bulk material properties are observed. However, as we make nanocrystals of the same material, energy levels split up and become discretized. As the particle size is further decreased, then energy splitting from the original bulk case increases as shown for red emitting and blue emitting NQDs of the same material, the only difference being the size of the particles (see Figure 3.2.1). Atom like band behaviors can also be observed for very small sized NQDs.

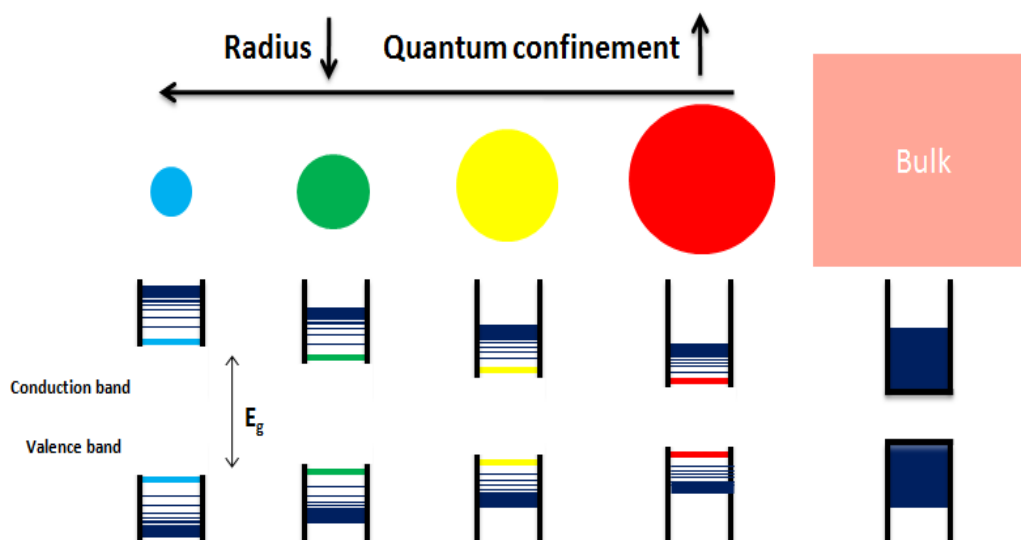


Figure 3.2.1. Schematic representation of semiconductor NQDs , along with its bulk, showing modified electronic band structures due to quantum confinement.

3.3 Synthesis of Nanocrystal Quantum Dots

Synthesis of NQDs is realized via colloidal chemistry routes. One of the most popular colloidal synthesis methods is hot injection. Hot injection technique is based on the injection of one of the precursors of the NQD into the mixture of the solvent and the other precursor at elevated temperatures so that both precursors react and start nucleation of NQDs in the presence of coordinating solvents. Most of the high quality core and core/shell NQDs are prepared using the hot injection method. To give some insight about the synthesis, here we provide a detailed explanation of the synthesis of CdSe core NQDs.

CdSe core NQDs are synthesized in a mixed high boiling point organic solvent mixture. Oleic acid (OA), tri-n-octylphosphine oxide (TOPO), tri-n-octylphosphine (TOP), hexadecylamine (HDA) and octadecene (ODE) are used as solvent, ligand and stabilizer for the synthesis. Precursors are prepared from

selenium powder (Se) and cadmium oxide (CdO). Toluene, methanol, acetone and chloroform are used before and after the synthesis.

First cadmium stock solution is prepared as follows: In a 100 mL flask, optimized amounts of CdO, OA and ODE are mixed. To get rid of any undesired species such as impurities in the solvents, the mixture is heated under vacuum using a Schlenk line (see Figure 3.3.1). The temperature can be permitted to increase up to 100°C for 30 min. If there are any undesired impurity other than our solvents inside the mixture, it will be sucked by the vacuum with the help of heating. After that, we immediately change vacuum line to Ar flow using the valve in the Schlenk line. Chiller is also turned on to cool the water in the condenser so that at elevated temperatures as 300 °C, boiling solvents could be returned to the reaction flask (see Figure 3.3.1). We enable the magnetic stirrer in the flask so that it will provide homogenous distribution of materials in the mixture. The temperature is increased step by step up to 300°C. Until transparent yellowish viscous solution is observed, the mixture is kept at 300°C while Ar flow continues to prevent any oxidation. Subsequently, the mixture is cooled down slowly to room temperature. Then, Cd stock solution becomes prepared.



Figure 3.3.1 Synthesis set-up consisting of Schlenk line for Argon flow and vacuum. Cold trap is utilized for vacuum line. Oxygen absorber is utilized for making oxygen free Ar flow.

Next, we prepare selenium stock solution. Since Se can be easily oxidized in ambient atmosphere, we perform the preparation in a nitrogen filled glove box environment (see Figure 3.3.2). 1 M solution of selenium stock solution is prepared by dissolving proper amount of Se powder in TOP at 200°C under constant stirring. A transparent solution is formed since all of the Se is dissolved.



Figure 3.3.2 Glove box filled with nitrogen to create oxygen free environment for oxygen sensitive material processing.

After preparation of Se stock solution, hot injection method is performed to synthesize CdSe cores NQDs. In a 25 mL 3-neck flask, optimized amounts of TOPO, HDA, ODE, and Cd stock solution is prepared and mixed. Again, using the Schlenk line system (see Figure 3.3.1) the mixture is purified from undesired impurities in solvents under vacuum by moderate heating. After the purification step, vacuum line is turned off and Ar flow is enabled. The mixture is heated up to 300 °C where the mixture becomes almost colorless. Selenium injection solution is prepared from as-prepared Se-stock solution, TOPO and ODE again

in glove box. The temperature is slightly decreased to 280 °C since a better crystal formation is observed at this temperature. Selenium solution is injected into the flask at 280 °C containing cadmium precursor and other solvents. Subsequent to the injection of the Se precursor, color of the mixture turns into yellow indicating that first nanocrystal formation has started. The duration of the synthesis determines the peak emission wavelength. At the beginning of the synthesis, smaller nanocrystals are formed so that they emit at shorter wavelengths. However, as the duration of the synthesis is increased, the particle sizes increase due to continuing growth of NQDs so that longer wavelength emission will be obtained. Depending on the aim of the synthesis, solution can be kept under constant stirring at 280 °C until the desired wavelength emission is reached, which can be checked by taking aliquots from the main solution and observing the PL under UV illumination. In Figure 3.3.3, synthesized CdSe core and CdSe/ZnS core/shell NQDs covering most of the visible emission spectrum are shown with increasing sizes from left to right.



Figure 3.3.3 Our-synthesized CdSe core and CdSe/ZnS core/shell NQDs with different sizes emitting at correspondingly different wavelengths.

3.4 Properties of Nanocrystal Quantum Dots

Emission of the NQDs can be easily tuned via either adjusting the size of the particles or material composition. For example, either making very small NQDs of CdSe or relatively larger NQDs of ZnSe, or alloy CdZnSe can be used to obtain cyan color emission. Also in Figure 3.4.1, we have shown green, yellow and red emitting CdSe/ZnS NQDs having different sizes. Although Cd chagonides can cover almost the whole visible range, Pb chagonides are popular for their emission spectra tunable from 800 to 2000 nm.

Also, absorbance of NQDs shows differences from organic counterparts such as dyes. Strong excitonic absorption peak can be observed for NQDs (see Figure 3.4.1). This is called the first excitonic absorption peak, which matches the ground state and first excited state transition (see also Figure 3.2.1 for schematic band diagram of NQDs). Due to inhomogenous broadening of the absorption related to poor monodispersivity of the NQDs, we cannot observe the very sharp excitonic peak, but more like a broadened peak. As can be attributed to their semiconductor properties, they have broad absorption spectra due to many available states at higher energy levels. The difference between excitonic peak in the absorption of NQDs and emission peak is the Stokes shift.

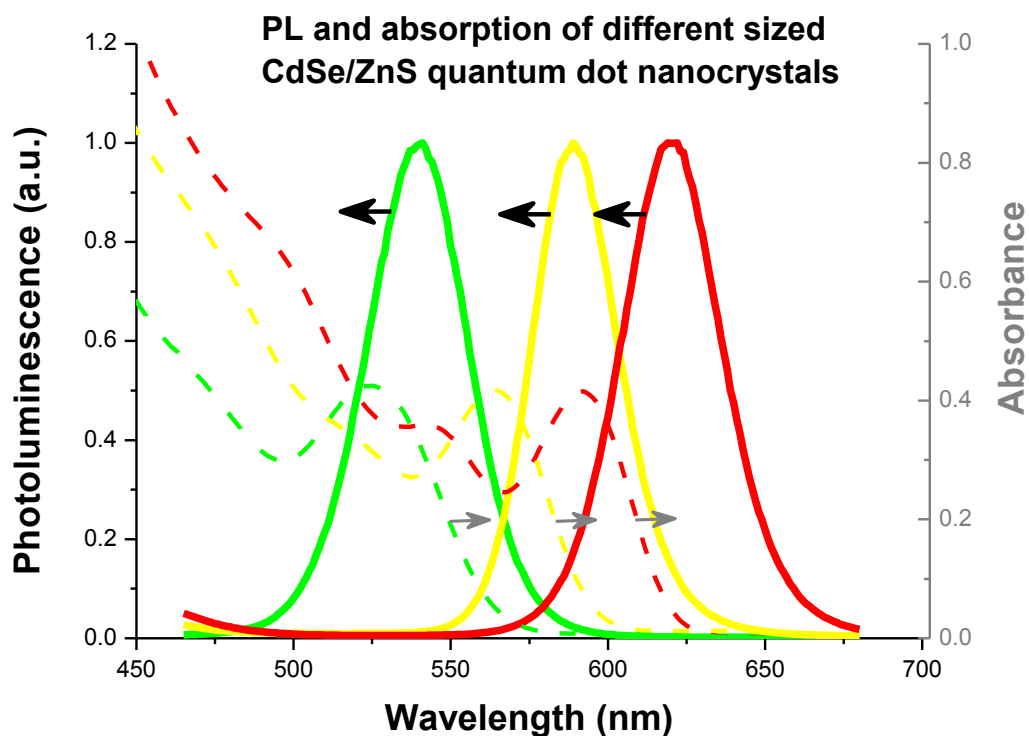


Figure 3.4.1. Photoluminescence and absorbance of CdSe/ZnS NQDs having different sizes (the largest particles has red emission, while the smallest has green emission).

One of the striking properties of NQDs is that they have quite narrow emission full width at half maximum, which is significant for display and lighting applications. The FWHMs range from 20 to 50 nm depending on the monodispersivity of the synthesized NQDs. In display applications, pure color emitters are required so that colloidal NQDs are thought as good candidates. TEM images of NQDs are useful to check for monodispersivity of the NQDs. CdSe/ZnS NQDs prepared with hot injection method are shown in Figure 3.4.2. Also, optical means such as dynamic light scattering instrument (DLS) could be employed to investigate size distribution of the particles.

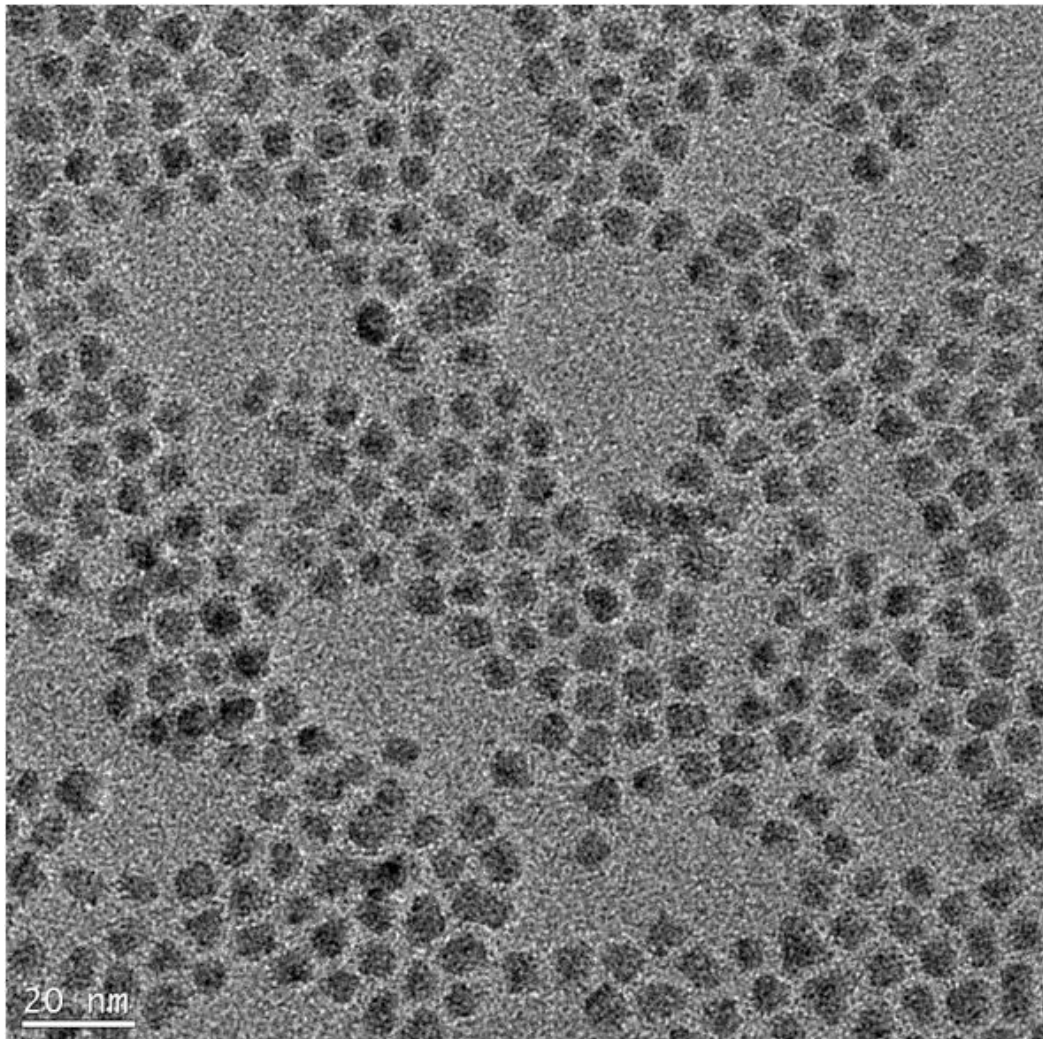


Figure 3.4.2 Highly monodisperse CdSe/ZnS NQDs.

Nowadays, NQDs can reach photoluminescence quantum efficiencies (PL QE) over 90 %. [25] High PL QEs arise from almost perfect crystalline properties and perfectly passivated surfaces by inorganic shells and organic ligands. In Figure 3.4.3, a TEM image of NQDs prepared in our lab is shown with a sub-nanometer resolution. These NQDs possess PL QE over 80%. Crystal structures as can be seen from TEM images are almost perfect. These NQDs possess unique alloy like structures consisting of CdSe/CdSe-CdS-ZnS/ZnS where mid-shell behaves as transition alloy region for better lattice match of the layers so that traps are minimized. To note here, PL QE measurements are generally

carried out via standard absorbance and photoluminescence measurement using a reference dye of a known PL QE.

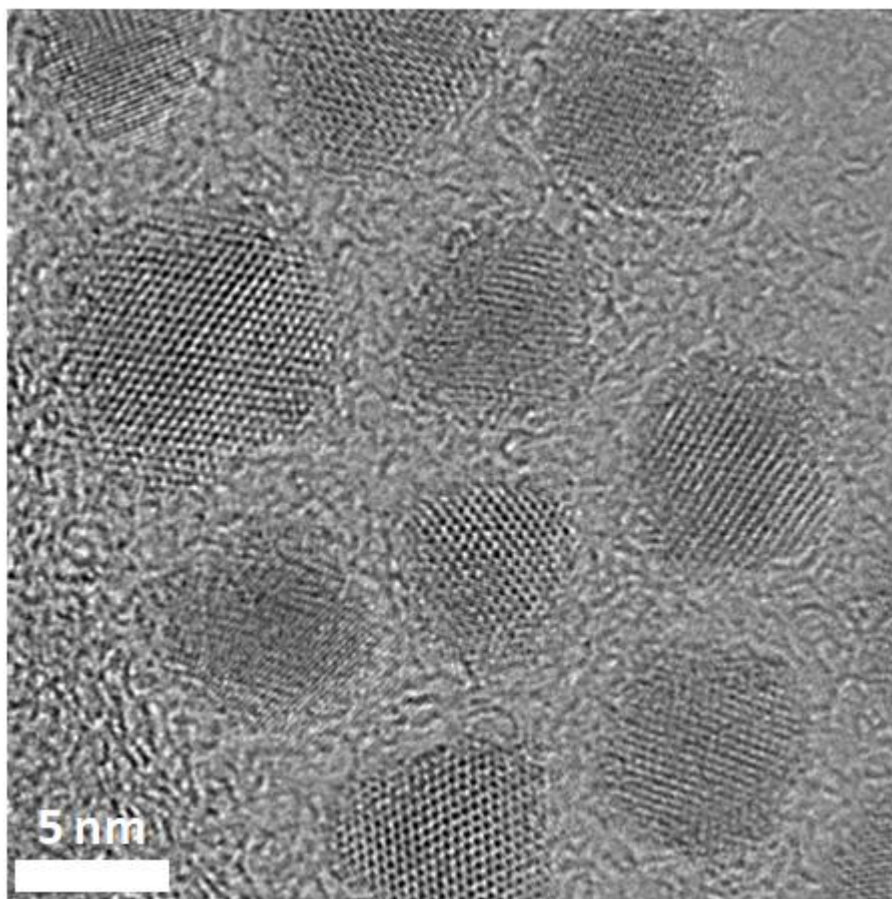


Figure 3.4.3 High resolution TEM image of CdSe/CdSe-CdS-ZnS/ZnS alloy like core/shell NQDs having PL QEs around 80%.

Another property of the NQDs is the increased environmental stabilities as compared to organic luminescent materials such as dyes and polymers. Photo-bleaching is a known phenomena for organic materials especially when they are excited with highly energetic photons (e.g., UV light). However, NQDs are quite stable materials due to increased nature of inorganic materials and strong covalent bonds, also stabilizing ligands and inorganic shells. As a result, they offer increased resistance against photo-degradation and –bleaching.

Thin film formation properties of NQDs are also quite important. NQDs are soluble in most of the solvents so that solution processing techniques such as spin coating, drop casting, layer-by-layer assembly, and ink jet printing can be employed. However, when made into thin films, high PL QEs of NQDs cannot be preserved due to their aggregate nature, which causes extra channels for the decay of excitons via nonradiative means despite of the high PL QEs in solution. As a result, methods such as embedding NQDs in host polymer matrices can be helpful to sustain high PL QEs. There are also many different properties of NQDs, which are still being investigated by the scientific community including blinking, charging, electroluminescence and emission polarization.

3.5 Applications

Today, NQDs are commercially available products, which are sold as dispersions. Each year more companies are involving in applications of NQDs. Main application areas cover wide range of optoelectronics such as light emitting diodes (LEDs), solar cells, detectors and lasers. In addition, NQDs could find many applications in biology in terms of bio-sensing and bio-tagging applications.

As mentioned in section 3.4, NQDs are novel luminescent materials and they are very promising materials for LEDs. They can be employed either as optically pumped color converter layers or can be electrically pumped in the active layer of the devices. Application of NQDs for color converter layers is significant especially for white light related applications because of versatility of the NQDs and possible schemes of enhancing the color conversion, for example, via nonradiative energy transfer means. [26, 27, 28] LEDs can also utilize electrically pumped NQDs. Electrically driven NQD based LEDs are also promising especially for display applications. [29, 30] Recently, Samsung R&D

has reported NQD based LEDs and displays with a complete demonstration of the first NQD based television. [31]

Applications of NQDs in photovoltaic solar cells is also promising since these materials have very high absorption coefficients as compared to their bulk counterparts owing increased oscillatory strengths of the dipoles (i.e., electron-hole pairs). Another advantage is the wide absorption spectra, which can be easily tuned. Alivisatos *et al.* is the first to show photovoltaic device applications of nanocrystal quantum rods while hybridizing them with polymeric charge transport materials. [32] However, applications related to charge extraction from NQDs is not straightforward since the design of NQDs favor confinement of the excitons in the cores, for better light emission makes it difficult to separate excitons into charge carriers and then transfer them to the respective collectors. Designing hetero-structures in different shapes and geometries could offer better solutions for solar cell applications since chances of charge extraction and transport could be enhanced. [33] Recently, Pb chalconide based nanocrystals become significant materials for solar cell applications since they have small band gaps so that huge portion of the sunlight could be utilized effectively. [34] Also, interesting physics such as carrier multiplication and hot electron transfer could become possible with these low band gap NQDs to harvest solar energy more efficiently. Alternatively, there are approaches of utilizing NQDs such as wavelength up-converters for better spectral utilization of the sunlight since most of the inorganic based solar cells cannot harvest UV and blue photons effectively due to photo-generation of electron-hole pairs close to trap state rich regions causing nonradiative recombination of the created electron hole pairs before they create photocurrent. [35]

Other applications such as detectors and lasers are still under development. Detectors made up of NQDs attract attention especially due to solution processing methods enabling ease of fabrication methods with the versatility of

utilizing even flexible substrates for the devices. [36] Among other solution processible materials for photodetectors, NQDs step forwards thanks to their stable nature as compared to its organic counterparts such as polymers and small organic molecules. Laser applications are still on the way, though most of the laser applications are performed with epitaxially grown quantum dots instead of colloiddally grown ones. This is due to poor electrical properties of colloiddally synthesized NQDs so that gain conditions can be only realized for optical pumping to date.

Chapter 4

Radiative and Nonradiative Energy Transfer Mechanisms

4.1 Introduction

Transfer of excitation energy (i.e., exciton, or bound electron-hole pair) between luminescent materials can be realized basically in two different means: Radiative and nonradiative. Exploiting these energy transfer mechanisms becomes important, since a lot of information about the molecular level interactions between luminescent materials could be revealed. Also, radiative and nonradiative energy transfer enabled applications in various fields ranging from biology to optoelectronics can help the development of novel enhanced devices such as biosensors, solar cells and light emitting diodes.

4.2 Nonradiative energy transfer

Nonradiative energy transfer (NRET) is the transfer of the excitation energy created in a luminescent material to another material which is generally (but not necessarily) luminescent. Nonradiative transfer of the excitation energy is a naturally occurring phenomenon between different photoactive parts of the photosynthesis systems in living organisms such as green plants and algae. In photosynthesis, light is absorbed via light absorbing molecules, and subsequently these molecules rapidly transfer their excitation energy via NRET to light harvesting proteins where reaction center enzymes are activated due to transferred excitation energy. Also in laboratories, NRET between different

luminescent material systems has been observed, but it could not be possible to explain and understand it until the proposed theories in 1940's. As can be seen in Figure 4.2.1, two different species of molecules lie in the same solvent. When donor molecules (D) and acceptor molecules (A) are homogeneously separated, fluorescence measurements give combined emission of the two species. If donor and acceptor molecules are made to bind to each other with some molecular linker, it has been observed that emission of the donor was quenched significantly, while, emission of the acceptor is observed to be increased. Radiative energy transfer mechanisms cannot explain this dramatic change in the emission spectrum of D-A molecules due to spatial positions of the molecules..

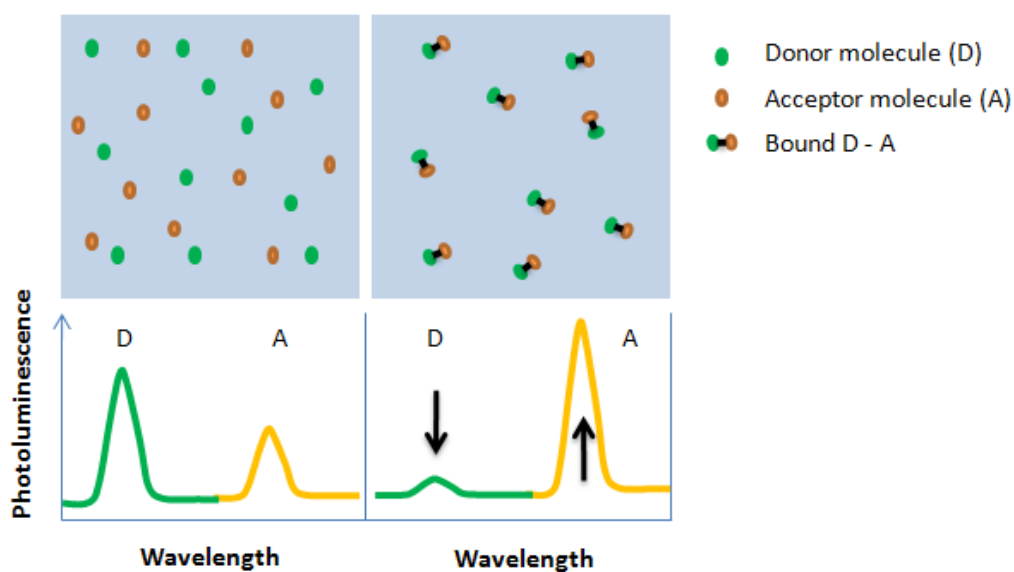


Figure 4.2.1 Exemplary experiment for the demonstration of the presence of NRET.

Perrins was the first who claimed that nonradiative energy transfer could be possible between luminescent molecules due to dipole-dipole interaction. [37] However, his formulation did not match the experimental results. Later, Theoder Förster was the first who explained the NRET in a more complete manner by incorporating a resonance requirement in addition to the dipole-dipole coupling. [38] Förster's formulation agreed very well with most of the experiments, so that today nonradiative energy transfer is also called Förster resonance energy

transfer (FRET). Here we will discuss the physical interpretation of the principle of operation of NRET to gain more insight about this phenomenon.

Excitation energy in the material consist of excited state excited electron in the conduction band (i.e., LUMO for molecular materials) and excited hole in the valence band (i.e., HOMO for molecular materials) spatially close to each other. For this reason, excited state can be seen as an oscillating transition dipole which resembles to a Hertzian dipole consisting of one positively and one negatively charged particle separated by some distance. The dipole created in the luminescent material has a dipole moment. Electric field is induced outside of the dipole (see Figure 4.2.2), which shows different properties in near field and far-field. In the near-field, created electric field is a non-propagating field, although in the far-field it becomes a propagating wave.

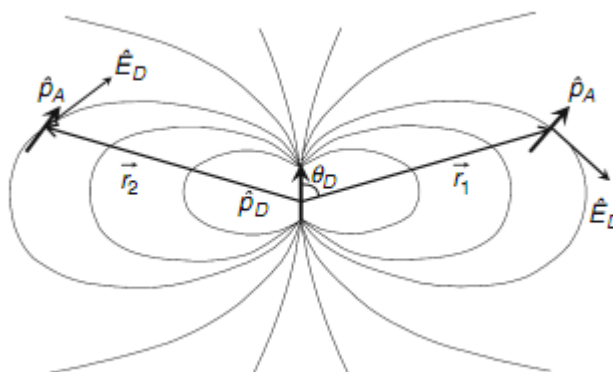


Figure 4.2.2 An oscillating Hertzian dipole is shown with electric field radiation patterns in the near-field. [39]

If another molecule, which is in its ground state but has a matching dipole moment property, is brought in close proximity to a luminescent molecule having an oscillating transition dipole due to its excited state electron and hole pair, a near field interaction energy is induced on ground state molecule: $E_{interaction} \propto \vec{E}_D \cdot \vec{p}_D \cdot \vec{p}_A$. This in fact shows the dipole-dipole coupling between two molecules. Here E_D is the electric field induced by oscillating

dipole in excited donor molecule, and p_D is the dipole moment in the donor molecule. p_A is the dipole moment in the acceptor molecule.

Electric field in the near-field is much more intense as compared to far-field electric field. If the acceptor molecule is close enough to the donor molecule, then the strong electric field in the presence of near-field conditions of the oscillating transition dipole in the donor molecule will be coupled to the acceptor dipole with the help of resonance between D - A molecules. The resonance requirement is related to the spectral overlap between donor emission and acceptor absorption. In other words, acceptor should have many available states matching with the excited state energies of the donor so that resonance condition will be satisfied. The coupling between dipoles due to resonance can also be seen as the coulomb coupling between the oscillating electron distributions in donor and acceptor molecules in the near-field conditions. Figure 4.2.3 shows the schematical representation of the principle of operation of NRET for luminescent molecules. A shorter wavelength pump excites (1) donor molecule where acceptor molecule cannot absorb that light due to unavailability of high energy states (i.e., no absorption at that wavelength of light). After the excitation of donor, rapid relaxation of the excited carriers towards band minima take place in very short time durations smaller than a few picoseconds (2). Due to the presence of a nearby acceptor molecule, dipole-dipole coupling occurs at the resonance condition and energy is transferred to the acceptor without emission of a photon (3-4). Then, an electron in the acceptor molecule becomes an excited state (5) followed by a rapid relaxation down to band minima (6). After that, emission of the acceptor at longer wavelengths can take place (7).

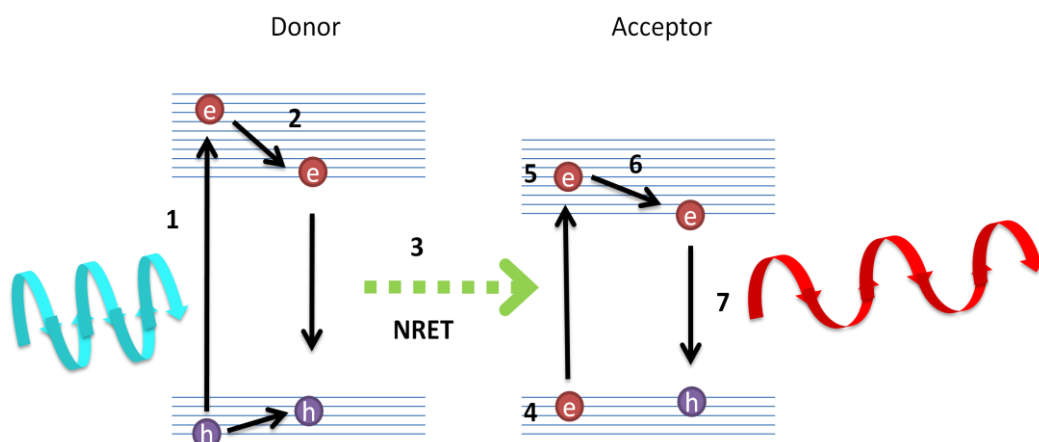


Figure 4.2.3 Schematic of the principle of operation of NRET between donor and acceptor luminescent molecules.

Förster made a few assumptions while developing the theory of NRET. One of them is that excitations in acceptor and donor molecules are in equilibrium state so that excited electrons and holes have already relaxed to their corresponding band minima prior to energy transfer. Since Förster assumed equilibrium conditions, time independent probability functions per unit time could be used to predict the amount of transferred energy. Another assumption was related to spatial arrangement of the D-A molecules, Förster has assumed that D-A molecules are just in close proximity so that they have only weak dipole coupling. However, alternative cases exist, in strong coupling regime due to very close packing of the D-A molecules, leading to results which cannot be explained by Förster. As observed in the photosynthesis systems, due to strong coupling between D-A molecules, coherent energy transfer is observed, which implies that excitation energy is transferred before excited carriers reaching their equilibrium condition. Förster's assumption of equilibrium condition generally leads to interpretation of incoherent energy transfer between D-A molecules.

In order NRET to occur, Förster predicted several requirements. The resonance requirement is satisfied with the spectral overlap between the donor emission and the acceptor absorption. Another requirement is that donor must be a luminophore with nonzero emission quantum efficiency (QE) so that it will at

least have some oscillating dipole. Also, D-A molecules should be close to each other (i.e., 1-10 nm) to yield decent NRET. Finally, donor should be in its excited state and acceptor should be in its ground state.

Spectral overlap J is calculated using overlap integral given in (4.2.1). $F_D(\lambda)$ is the normalized fluorescence of the donor. $\varepsilon_A(\lambda)$ is the extinction coefficient of acceptor. If λ is in nanometers and ε_A is in $M^{-1}cm^{-1}$ units, then J is in units of $M^{-1}cm^{-1}nm^4$.

$$J = \int_0^{\infty} F_D(\lambda) \varepsilon_A(\lambda) \lambda^4 d\lambda \quad (4.2.1)$$

Spectral overlap determines the strength of the resonance condition. The reason why whole spectrum of donor emission and acceptor absorption is utilized instead of considering only a smaller portion of the emission spectrum of the donor is related to Heisenberg uncertainty principle. Since D-A molecules are in their near field, uncertainty in position decreases so that uncertainty in energy is increased which further broadens the resonance energy levels so that Förster decided to use whole spectra for donor and acceptor to calculate the spectral overlap.

Another significant parameter of the NRET is the so-called Förster radius, which is defined as the specific distance between D-A molecules where the energy transfer efficiency is 50%. R_o (Förster radius) is calculated as in ((4.2.2).

$$R_o = 0.211 (\kappa^2 n^{-4} QE J)^{\frac{1}{6}} \quad (4.2.2)$$

where κ^2 is the dipole orientation factor between D-A. It is generally taken to be 2/3 for randomly oriented D-A dipoles. However, one must be careful while dealing with κ^2 since it may change for different material systems especially for quasi-zero dimensional materials such as polymer and quantum wells. n is the refractive index of the medium. QE is the fluorescence quantum efficiency of the donor. J is the as-calculated spectral overlap between D-A.

Energy transfer rate can be calculated using (4.2.3) where τ_D is the donor fluorescence lifetime in the absence of acceptor molecules. R_o is the Förster radius, and r is the actual separation between D-A molecules.

$$k_{ET} = \frac{1}{\tau_D} \left(\frac{R_o}{r} \right)^6 \quad (4.2.3)$$

As a result, the main control over the NRET rate is the separation distance between D – A molecules, which leads to many applications such as precise measurement of the distance between different molecules.

The methods to characterize NRET generally involves the use of optical spectroscopy. Time resolved and steady state fluorescence measurements can be used to measure the dynamics of NRET. Fluorescence lifetime of donor molecules in the presence and absence of the acceptors can be easily measured with time resolved fluorescence spectroscopy tool (see section 2.3.1) from where energy transfer efficiencies can be directly calculated using ((4.2.4).

$$\eta_{ET} = 1 - \frac{\tau_{DA}}{\tau_D} \quad (4.2.4)$$

For this formula to hold, donor molecules should be fitted with single exponential decays in the presence (τ_{DA}) and absence (τ_D) of acceptors. For τ_{DA} multi-exponential decays could be used, but amplitude averaged lifetimes are then used to calculate the NRET efficiency.

Upon introduction of acceptor molecules nearby donor molecules causes donor lifetime to be shortened, since an extra channel of transferring the excitation energy in the donor molecules becomes available. Figure 4.2.4 shows the Jablonski energy diagram for a fluorescent molecule with possible pathways for de-population of the excited state. When nonradiative energy transfer channel is opened up due to the presence of nearby acceptor molecules, then the total rate of de-excitation increases so that donor lifetime is shortened.

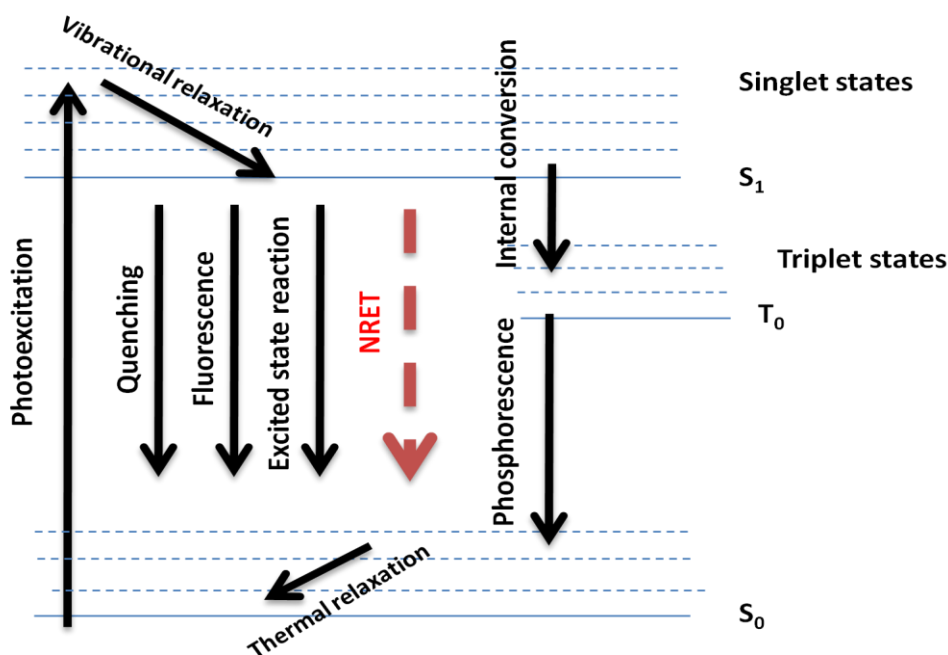


Figure 4.2.4 Jablonski energy diagram of a luminescent organic molecule with possible de-excitation pathways.

Also using steady state fluorescence measurements energy transfer efficiencies can be calculated using ((4.2.5) where I_{DA} and I_D are the emission intensities of donor molecules in the presence and absence of acceptors. Since some of the excitation is transferred to the acceptor molecules, emission of the donor molecules is quenched.

$$\eta_{ET} = 1 - \frac{I_{DA}}{I_D} \tag{4.2.5}$$

Energy transfer efficiency can be also calculated using derivation from the rate equation formalism as shown in (4.2.6).

$$\eta_{ET} = \frac{k_{ET}}{k_{ET} + \tau_D^{-1}} \tag{4.2.6}$$

Back energy transfer is not a problem for NRET based systems. Due to the conservation of energy, new excited state created in the acceptor molecule has

the same energy as the donor molecule excited state due to the resonance condition. However, rapid internal relaxations of the excited state particles in the acceptor ends up with conduction band minima, so that back energy transfer will not be allowed since acceptor energy band gap is smaller than the band gap of donor. This can also be observed in step (3-6) in Figure 4.2.3.

4.3 Radiative Energy Transfer

Radiative energy transfer optical pumping is different from nonradiative energy transfer in terms of participation of photons directly. Again, there should be a spectral overlap between the donor emission and the acceptor absorption. However, those species do not have to be close to each other. For example the Sun is one of the biggest radiative energy transfer donor, however it is quite far away from the acceptors in the world. Radiative energy transfer is a weak process as compared with nonradiative energy transfer. Unlike NRET, which can be maximized by making species closer, radiative energy transfer mainly depends on the material properties (i.e., PL QE, absorption coefficient). While making spectroscopic experiments, radiative energy transfer acts as a secondary effect. It becomes important especially when the concentration of acceptors are increased due to increased optical density of the acceptors where interaction probability of photons with acceptor molecules is increased as the density of acceptors is increased.

4.4 Applications

In this part of the thesis, we will summarize the applications of radiative and nonradiative energy transfer (RET and NRET) mechanisms for semiconductor nanocrystal quantum dots, although RET and NRET can be applied to various material systems. Nanocrystal quantum dots (NQDs) can be both used as donor and acceptor species in NRET studies. [40] In late 90's it was shown that different sized CdSe NQDs can be used as energy donors (smaller NQDs) and

acceptors (larger NQDs) in thin films. [41] Both steady state PL and time resolved characterization have shown that efficient energy transfer can take place in between different sized NQDs.

The first applications of NQDs exploiting their energy transfer capabilities were found in bio-sensing area. A nanocomposite structure of NQDs-protein-dye is proposed to control NRET between NQDs and dyes through conformations of protein in the presence of materials to be sensed. The sensing material causes conformations on the protein so that the acceptor dye and the donor NQDs are drawn away from each other, which decreases NRET rates. [42] Another application is utilizing NQDs as sensitizers for Pc4, which is used to create singlet oxygen for photodynamic medical therapy purposes. The spectral light utilization of Pc4 is enhanced via NRET from NQDs in this system so singlet oxygen creation rate could be increased. [43] Except for biology and biotechnology applications, NQDs can find utilization in optoelectronics. Both RET and NRET are utilized to obtain enhanced solar cells, detectors and light emitting diodes with novel device designs. [44, 45, 46]

Chapter 5

Radiative Energy Transfer from Quantum Dots to Silicon Nanopillars for Enhanced Novel Silicon Solar Cells

This chapter is based in part on the publication “Photovoltaic nanopillar radial junction diode architecture enhanced by integrating semiconductor quantum dot nanocrystals as light harvesters,” **B. Guzelturk**, E. Mutlugun, X. Wang, K.L. Pey, and H. V. Demir, *Applied Physics Letters* 97, 9 (2010). Reproduced (or ‘Reproduced in part’) with permission from American Institute of Physics. Copyright 2011 American Institute of Physics

5.1 Introduction and Motivation

The enormous potential of Sun as an efficient source of electricity fascinated people to develop photovoltaics for a long time. [47] The science and industry of photovoltaics evolved a lot in the last decades. Today’s photovoltaic market is currently being dominated by conventional crystalline silicon based solar cells, also known as the first generation solar cells. [48] Due to limitations of silicon, alternative materials and device designs that can potentially enable efficient solar conversion at reduced costs are heavily being investigated. However, silicon, being the second most abundant material on earth, still stands as the most promising candidate. [49] Today one dimensional nanostructures such as

one dimensional nanowires and nanorods are gradually coming into prominence in photovoltaics research due to their advantages for effective light harvesting. [50, 51, 52, 53]

Si nanopillar solar cells are promising candidates as they can harness the advantages of one-dimensional confined structures including enhanced photocurrent owing to increased junction area with a large surface-to-volume ratio and improved optical properties including light trapping, and increased absorption and reduced reflectance with respect to their planar thin film counterparts. [54, 55, 56, 57, 58] However, the-state-of-art efficiencies of these nanostructured solar cells are typically lower than their planar versions due to the problems encountered in nanofabrication processes and difficulties related to their poor surface passivation.[51] Although such nanofabrication methods can be matured in the future, it is technically challenging to overcome the intrinsic limitations of silicon. Such one important limitation is that Si based solar cells suffer from poor responsivities at short wavelengths, particularly in UV and blue. [59] However, this unused spectral range of the solar irradiation constitutes almost 10% of sun light spectra at the surface of the earth. [60] The main reason of poor conversion of UV and blue spectrum is the high absorption coefficient of silicon at those wavelengths. [59] As shown in Figure 5.1.1 UV and blue photons are absorbed very strongly so that electron-hole pairs are created very close to the surface of silicon (i.e., a few tens of nanometers), where these e-h pairs will suffer mostly from a large number of surface traps and limited charge mobility of Si, which will limit those carriers reaching the junction in order to contribute to the photocurrent.

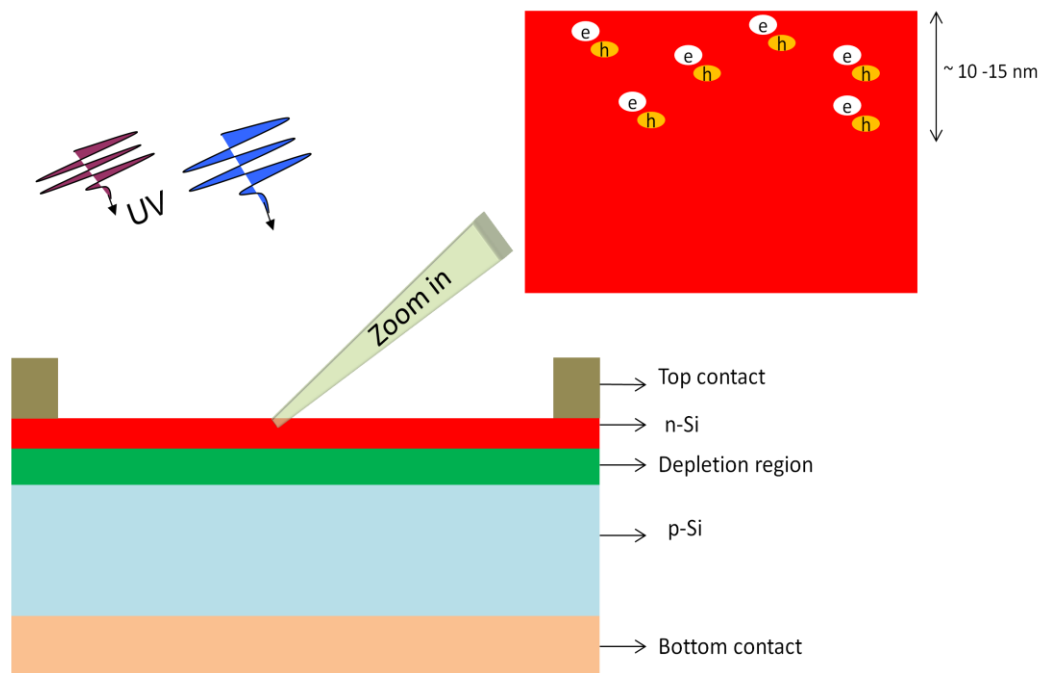


Figure 5.1.1 Typical architecture of a planar crystalline silicon solar cell. Short wavelength (highly energetic) photons are absorbed very close to the silicon surface.

At short wavelengths, current responsivities (amount of created output current / amount of optical power input) or external quantum efficiencies (amount of created output electrons / amount of input photons) become very small due to this intrinsic property of silicon as shown in Figure 5.1.2 as an exemplary external quantum efficiency versus wavelength plot of a silicon nanowire solar cell that is used in this thesis.

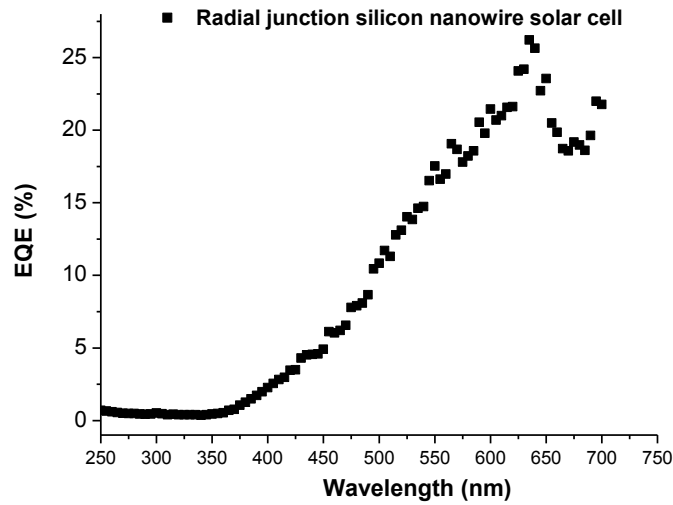


Figure 5.1.2 Exemplary external quantum efficiency vs. wavelength of a silicon nanowire solar cell used in this study.

5.2 Proposal and Principles of Operation

To provide a solution to this low responsivity and light harvesting problem at short wavelengths, we have proposed and demonstrated the utilization of colloidal quantum dots as wavelength up-converters hybridized on radial p-n junction nanopillar solar cells made of Si to improve their UV performance and enhance their solar conversion efficiency. [61] There have been previous reports focusing on the use of luminescent wavelength up-converters for silicon based solar cells thus far, including quantum dots to harvest light spectrally better to improve the performance of Si based photodetectors [62] and photovoltaic devices. [63, 64, 65, 66] However, to date, the class of new solar cell architectures based on nanopillars have not been investigated for the hybridization of quantum dots as optical wavelength up-converters to enhance solar conversion activity. With incorporation of such quantum dots, structural advantages of nanopillars including increased light trapping can also be

benefited to obtain higher levels of enhancement compared to planar solar cell counterparts.

In this chapter of the thesis, we investigate the integration of CdSe nanocrystals intimately on radial p-n junction based Si nanopillar solar cells, with these nanocrystals strongly absorbing incident UV and blue light, and emitting at a longer wavelength, which were chosen to match the higher spectral response of the silicon solar cell. Figure 5.2. 1 illustrates the principles of operation of the proposed hybrid device.

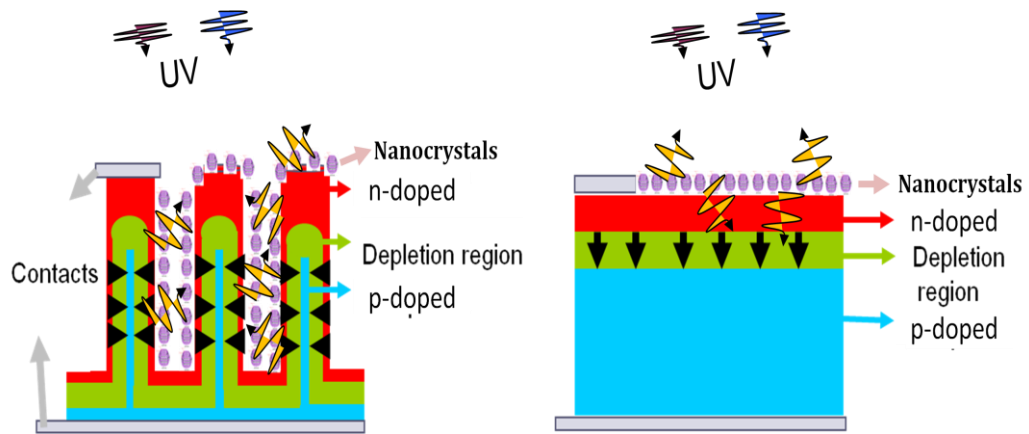


Figure 5.2. 1 Illustration of the principles of operation of the nanocrystal up-converter layers for silicon solar cell. Comparison of the planar and nanopillar architecture is pictorially presented. UV and blue waves are shown as the excitation photons. Orange colored waves represents the longer wavelength emission of nanocrystals after conversion of UV and blue photons. Black colored arrows represents the built-in electric field in depletion region.

CdSe nanocrystals deposited on nanowires act as wavelength up-converters due to their absorption and emission characteristics as shown in Figure 5.2.2. Unlike organic luminescent materials, nanocrystals have wide absorption and narrow emission spectra. We utilize the effective absorption of these nanocrystals at UV and blue wavelengths.

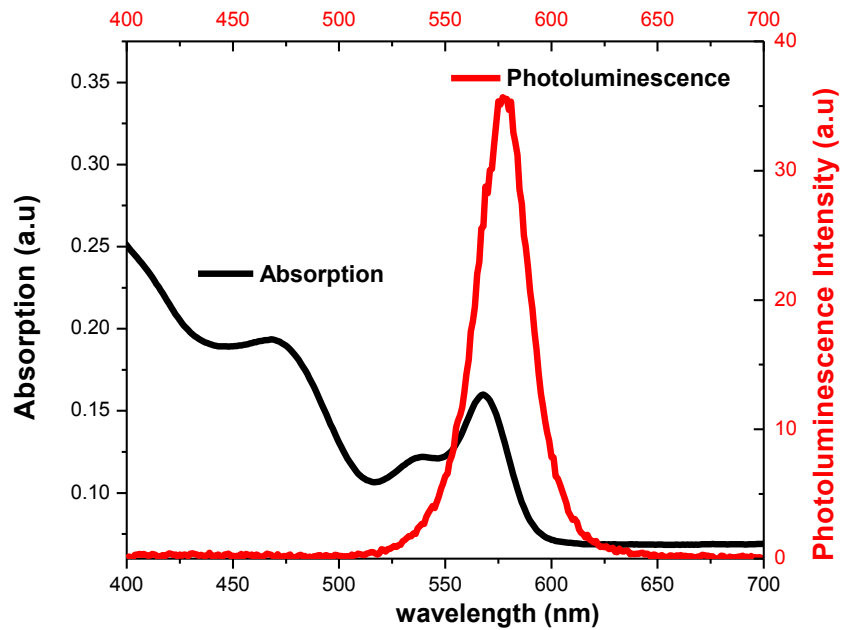


Figure 5.2.2 Absorption (black line) and emission spectrum (red line) of the utilized CdSe nanocrystals.

Subsequent to the absorption, longer wavelength emission, which is related to the size and material composition of the nanocrystal, takes place. Emission of the nanocrystals is chosen to be matching with the better responsivity region of silicon so that poorly used UV and blue photons are converted into longer wavelength photons that are more favorably converted into photocurrent.

Use of nanopillar architecture will benefit for its increased light trapping properties. In our previous proposal Mutlugun *et al.* have utilized planar architecture p-n junction silicon solar cells to integrate with nanocrystals where at least half of the converted photons cannot be coupled to the solar cell due to isotropic emission of the nanocrystals. [63] However, use of non-planar architectures (i.e., silicon nanopillars) would be advantageous to lead to larger enhancements because of wavelength up-conversion of nanocrystals.

5.3 Experiments and Results

Through incorporation of these colloidal quantum dots on Si nanopillar solar cells, we have demonstrated approximately 13% enhancement of overall solar conversion efficiency measured under AM1.5G (air mass 1.5 global conditions). We have also shown spectral enhancement up to 6-folds in responsivity of the nanopillar photovoltaic devices measured under monochromatic UV light illumination. Comparing against the planar architecture of the same silicon solar cells with the same amount of hybridized quantum dots, we have shown that a maximum enhancement factor of more than four times can be achieved using the nanopillar architecture, because of its superior geometric and structural characteristics that enables efficient utilization of the emission from nanocrystals.

In our experiments, scanning electron microscopy (SEM) images are taken by FEI Quanta 200 FEG, and transmission electron microscopy (TEM) images, by FEI Tecnai G2 F30. Absorbance and emission spectra are recorded using Cary UV-Vis spectrophotometer and Cary 100 Fluorometer, respectively. A dynamic light scattering DLS system from Malvern Zeta Sizer is used for the quantum dot size characterization, and a Newport Series 150 W Solar Simulator is employed for photovoltaic performance characterizations. Here, for solar cell testing, the standard sunlight spectrum is simulated at an intensity level of 100 mW/cm² incident on the Earth surface by using an AM1.5G filter in front of the solar simulator to include both diffusive and direct sunlight radiation. Subsequently, external quantum efficiency, EQE, and responsivity of these devices are investigated using a wide spectrum Xe light source, a monochromator, a chopper, and an optical powermeter to observe the spectral enhancement effects of the up-converter nanocrystal layers.

Figure 5.3.1 shows SEM images of silicon nanopillars and a completed working device. The pillar diameter is around 670 nm with a pillar height over 1 μm . These are radial p-n junction coaxial solar cells fabricated by diffusion process based on metal assisted chemical top-down etching method. [67, 68] Briefly, the Si nanopillar arrays were formed by the electrochemical etching method combined with nanosphere lithography using metal assisted chemical etching method. The starting Si(100) here is p-type (boron-doped) with a resistivity of 0.1-1 $\Omega\cdot\text{cm}$. The nanopillar diameter is about 670 nm defined by the nanosphere lithography. After the nanopillar formation using metal assisted chemical etching of silicon, a novel doping process was developed to convert the nanopillar shell to n-type, forming the core-shell p-n junction structure. After the junction formation, the contact was formed by depositing Ti/Au ($\sim 10\text{ nm}/100\text{ nm}$) at the backside, and Ti/Ag ($\sim 30\text{ nm}/1000\text{ nm}$) at the front side to form a continuous film on the nanopillar arrays.

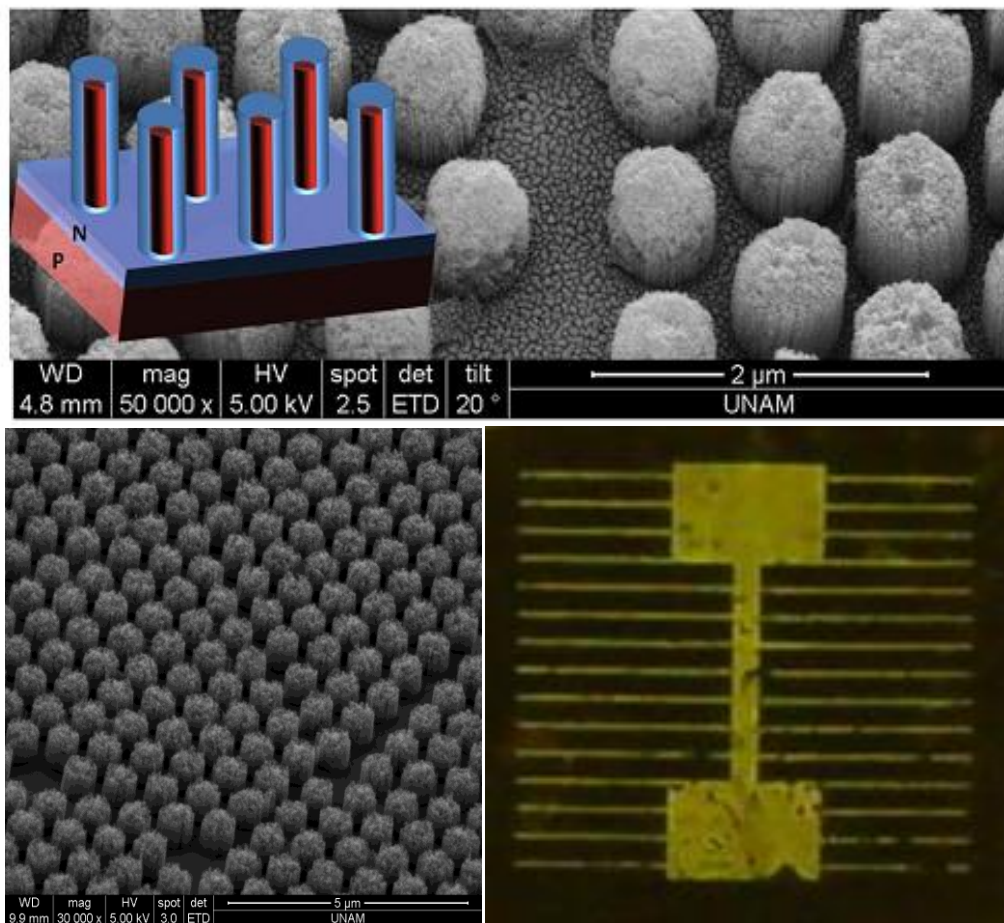


Figure 5.3.1 Scanning electron micrographs for fabricated radial p-n junction Si nanopillar solar cell are shown. The device architecture is also depicted. Photograph of the active device is given, where device active area is $\sim 0.81 \text{ cm}^2$.

Figure 5.2.2 shows the absorption and photoluminescence spectra of colloidal CdSe nanocrystals in solution. TEM image of the nanocrystals is shown in Figure 5.3.2. These quantum dots are synthesized in organic nonpolar solvent using hot-injection technique as also described in Chapter 3 [69, 70]. The first exciton peak of CdSe nanocrystals corresponds to 568 nm with a peak emission wavelength of 579 nm. In solution photoluminescence quantum yield of nanocrystals is measured as 35% using rhodamine 6G as a reference dye. The radius of the core CdSe quantum dots is calculated to be 3.46 nm [71] and experimentally observed to be 7.65 nm using DLS; here the diameter is observed to be larger possibly due to the ligands attached on the surface of the quantum dots.

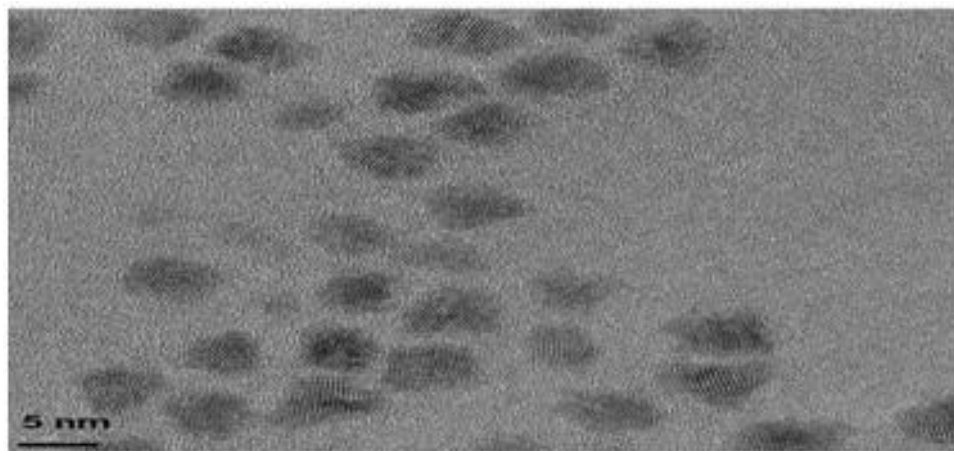


Figure 5.3.2 Transmission electron micrograph of synthesized CdSe nanocrystals (scale bar is 5 nm).

To employ the quantum dots as optical wavelength up-converting layer, we have coated CdSe nanocrystals over solar cells both in nanopillar and planar architectures using drop-casting method (see Figure 5.3.3). The hybridized amount of nanocrystals is identical for both architectures, which is empirically found to be $81.74 \mu\text{g}/\text{cm}^2$ in the optimal case.

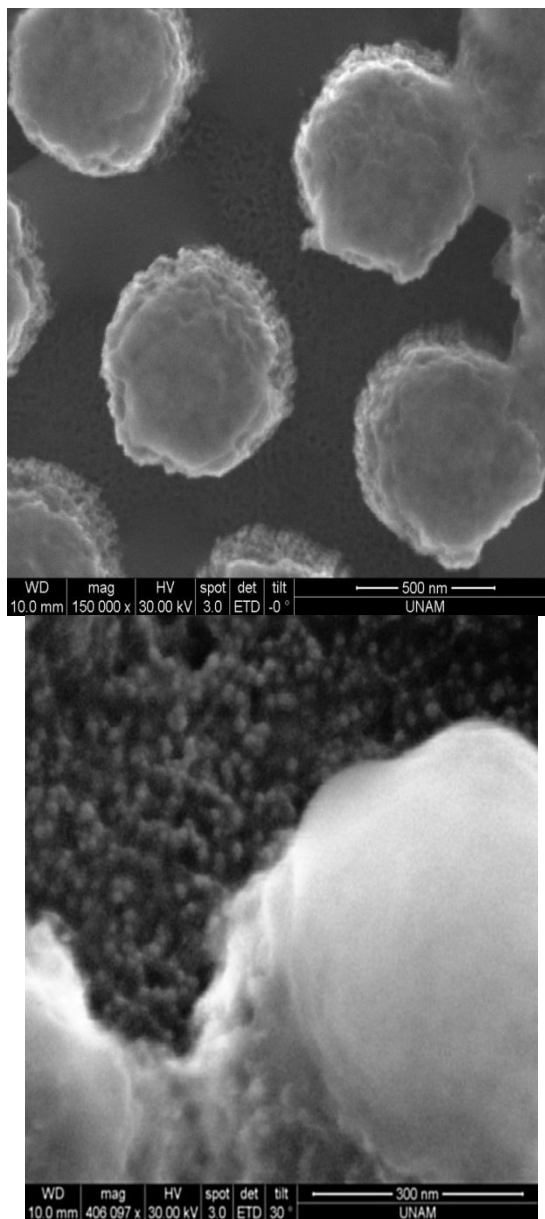


Figure 5.3.3 SEM images of silicon nanopillars after nanocrystals are incorporated.

The current-voltage (I-V) characteristics of solar cells are measured using solar simulator under AM1.5G conditions to study the evolution of solar cell parameters before and after nanocrystal integration. Table 5.3.1 shows the solar cell parameters before and after nanocrystal introduction for both nanopillar and planar architecture solar cells. Also, Figure 5.3.4 shows I-V curves of nanopillar solar cell measured under AM1.5G conditions before and after the hybridization of CdSe nanocrystals. Introduction of the up-converter layer on both nanopillar

and planar solar cell structures increased the short circuit current (I_{sc}) as expected, as a result of the enhancement in responsivity of the respective hybrid devices. Open circuit voltage (V_{oc}) remained approximately the same before and after the nanocrystal incorporation. The solar power conversion efficiency is increased by 13.37% and 12.42% in nanopillar solar cell and thin film planar solar cell architectures, respectively.

Sample	I_{sc} (mA)	V_{oc} (V)	Fill factor (%)	Efficiency (%)
Nanopillar solar cell w/o QDs	6.59	0.42	50.4	1.72
Nanopillar solar cell w QDs	6.90	0.42	54.5	1.95
Planar solar cell w/o QDs	12.01	0.52	41.95	3.22
Planar solar cell w QDs	14.43	0.53	38.3	3.62

Table 5.3.1 Evolution of solar cell parameters before and after incorporation of nanocrystals.

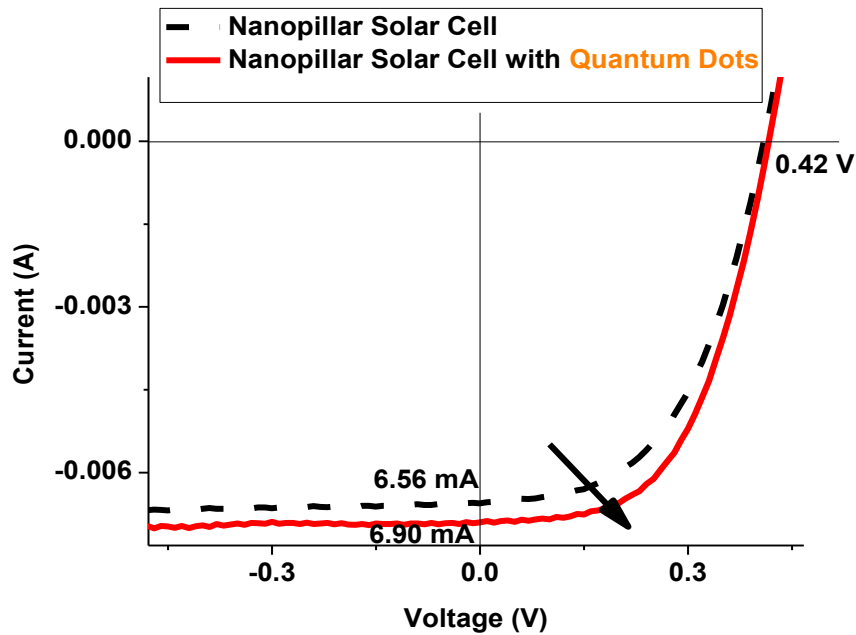


Figure 5.3.4 Current-Voltage (I-V) curves of the nanopillar solar cell before and after nanocrystal incorporation under AM 1.5G 1sun illumination conditions.

This enhancement stems from the enhanced EQE of the hybrid devices. Compared to the planar solar cells, the enhancement achieved with nanopillar solar cells is larger since the nanopillar solar cell provides a suitable geometry for light trapping. In the nanopillar architecture light emitted by the nanocrystals is mostly trapped, which facilitates stronger absorption of these emitted photons in Si, whereas at least half of the emitted photons from nanocrystals cannot be harvested in the planar case.

Furthermore, to gain more physical insight on the origin of the enhancement, we have used monochromatic light, and measured the EQE of the devices. When nanocrystals are hybridized on the solar cell platform, it is shown that higher energy photons corresponding to the ultraviolet and blue range of the solar spectrum are utilized more efficiently (see Figure 5.3.5). EQE spectra of nanopillar and planar solar cell architectures are also depicted before and after hybridization of nanocrystal layer in inset of Figure 5.3.5. Here we show that the nanocrystals provide up to six-fold EQE enhancement in the UV portion of solar light on the nanopillar solar cell platform (see Figure 5.3.5). The maximum EQE

enhancement achieved using nanopillar architecture is found to be more than 4 times larger compared to the planar structure. This stems from the superior light trapping of the nanopillar structure revealed by the use of nanocrystals.

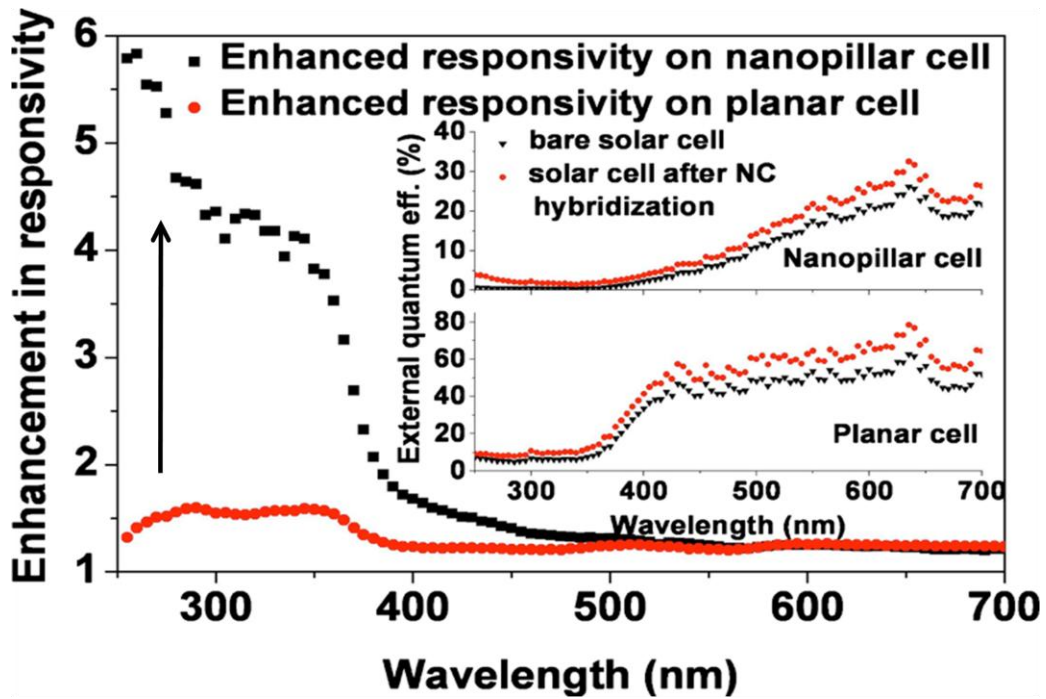


Figure 5.3.5 Enhancement in responsivity due to nanocrystal hybridization in planar and nanopillar solar cell devices is presented. Inset shows external quantum efficiencies of the nanopillar and planar devices before and after nanocrystal incorporation.

Although CdSe nanocrystals have no emission at longer wavelengths, there is still an enhancement about 20% in EQE of both nanopillar and planar devices at these wavelengths. It is found that introduced nanocrystal thin film over silicon serves as a graded index layer, which also increases the coupling of light into solar cell even at long wavelengths where nanocrystals do not emit, as confirmed by reflectivity measurements. Since refractive index mismatch between silicon and air is large (i.e., $n_{\text{silicon}} = \sim 3.5$, $n_{\text{air}} = \sim 1$), nanocrystal layer having refractive index around 1.8 reduces the mismatch like a anti-reflective coating. As seen from Figure 5.3.6 we observe that the reflection of Si planar solar cells is reduced with the integration of quantum dots in the range of 50%.

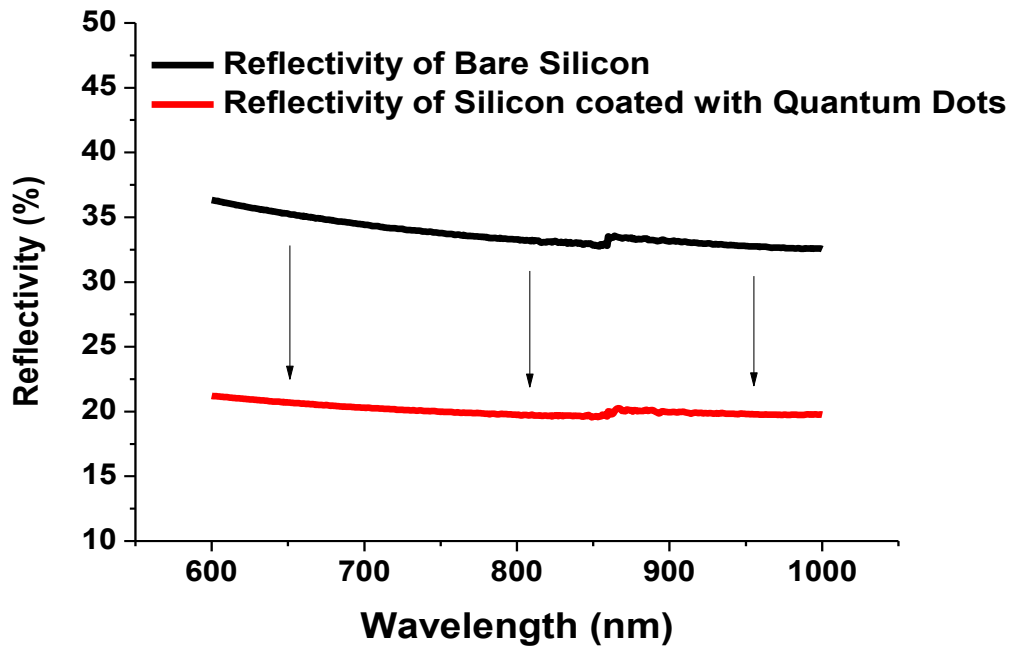


Figure 5.3.6 Measured reflectivity of silicon surface with and without nanocrystal coating.

For nanopillar architecture, reflectivity is much lower than its planar counterpart due to structural superiority as shown in the inset of Figure 5.3.7. We also made FDTD analysis of the reflection properties of nanopillars before and after quantum dot incorporation. While mimicking nanocrystal layer as a planar layer of refractive index and extinction coefficient (n and k , respectively) measured from ellipsometer. We represent our results as enhanced light trapping which indicates the amount of reduction in reflection. We obtained similar results as the experimental ones as shown in Figure 5.3.7.

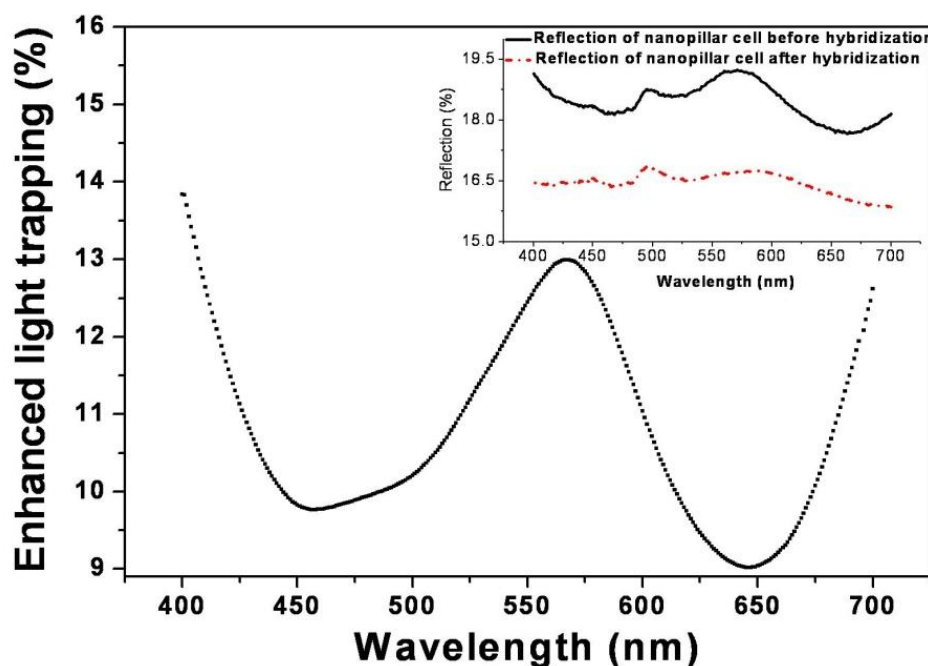


Figure 5.3.7 FDTD analysis of reduction of the reflectivity and enhanced light trapping of nanopillar silicon solar cell due to nanocrystal incorporation. Inset shows the measured reflection (%) before and after nanocrystal incorporation.

Due to immature fabrication methods, EQE of nanopillar solar cells is lower than that of thin film devices (see Table 5.3.1). As a result, a planar solar cell typically has a higher solar conversion efficiency than a nanopillar solar cell. The problem of large surface states in nanopillar devices undesirably leads to higher recombination rates for photogenerated electron-hole pairs, which in turn results in lower EQE than its planar counterparts. When a wavelength up-converting nanocrystal layer is incorporated, although the resulting EQE enhancement in nanopillar structure is much larger than that in planar device because of better light trapping of nanopillars, this enhancement is not fully reflected in the overall solar conversion efficiency enhancement. This is due to fact that smaller enhancement in EQE of planar device contributes more additional photocurrent than the additional amount contributed in the case of nanopillar device, while the starting EQE is much larger in the planar device. Ideally, with nanopillar solar cells having similar EQE as the planar solar cells,

much larger enhancements in solar conversion efficiency can be obtained in nanopillar architecture.

5.4 Conclusions

In summary, we studied and showed enhanced photovoltaic device performance by hybridizing CdSe nanocrystals on radial p-n junction based silicon nanopillar solar cells. In such hybrid architecture, these nanocrystals are utilized as efficient wavelength up-converters to harvest incident photons that are otherwise poorly utilized at short wavelengths and convert them to photons favorably used at long wavelengths by silicon solar cells. We demonstrated approximately 13% enhancement of solar conversion efficiency under AM1.5G condition and up to six-fold enhancement in responsivity in UV spectrum for the nanopillar solar cells. Additionally, we achieved a maximum responsivity enhancement of more than four-fold in UV using the nanopillar solar cells compared to the planar cell case. This is enabled by the superior light trapping properties of nanopillar architecture. Radial junction nanopillar solar cells hold promise for possible future photovoltaic applications with their performance enhanced via the hybridization of optical wavelength up-converting nanocrystal quantum dots around the pillars. Future work could include enhancing the film efficiencies of the nanocrystals so that wavelength conversion will be more effective process. Definitely, in order to exploit the full advantages of the nanostructured solar cells, matured fabrication methods will be required in the future.

Chapter 6

Nonradiative Energy Transfer from InGaN/GaN Multi Quantum Well Nanopillars to Quantum Dots: Efficient Color Converters for Light Emitting Diodes

This chapter is based in part on the publication “Efficient nonradiative energy transfer from InGaN/GaN nanopillars to CdSe/ZnS core/shell nanocrystals” S. Nizamoglu, **B. Guzelturk**, D-W. Jeon, I-H. Lee, and H. V. Demir, Applied Physics Letters 98, 1 (2011). Reproduced (or ‘Reproduced in part’) with permission from American Institute of Physics. Copyright 2011 American Institute of Physics.

6.1 Introduction and Motivation

Luminescent nanocrystal quantum dots are emerging materials for various optoelectronic devices such as light emitting diodes, solar cells, light modulators, and lasers. [72,73] Nanocrystal quantum dots (NQDs) having high photoluminescence quantum efficiencies, increased environmental stabilities as compared to their organic counterparts (e.g., luminescent dyes), and tunable emission spectra along with narrow emission full-width-at-half-maximums

(FWHM) make them impressive and promising material systems for light emitting devices.

There are two main schemes for utilizing these NQDs in light emitting diodes. First, NQDs can be electrically pumped via injection of the electrical charges in light emitting diode architectures similar to organic light emitting diodes (OLEDs). Emission takes place as a result of recombination of electron-hole pairs in the NQDs by means of electrical pumping of the charge carriers. [74, 75] Electrical injection approach has fundamental difficulties due to material properties of the NQDs. The core of a NQD, where excitons are mostly confined and the photon emission mainly takes place, is generally surrounded with inorganic shells and organic ligands. Inorganic shell has multiple purposes as protecting the cores from surrounding environment and confining the excitons. Organic ligands increase the solubility of the material. However, these ligands pose very high potential barriers for the direct injection of the charges into the available state of the core. As a result, direct charge injection is generally an inefficient process for colloiddally prepared NQDs. Other problems such as balance of injected charges and charging of the NQDs make electrically active NQD based light emitting devices complicated. [76] To amend some of the mentioned problems of direct charge injection, we also propose an alternative exciton injection scheme, which is further explained in Chapter 7.

An alternative and less complicated approach is the utilization of NQDs as an electrically passive, but optically active film, as the so-called color converters. Color converter light emitting diodes are composed of two parts: The first part is short wavelength emitting pump LED. The second is color converter layer made up of highly luminescent materials placed on top of the pump LED in order to achieve color conversion though radiative energy transfer of the pump photons down-converted to longer wavelength photons (i.e., in a desired and tunable fashion) via converter layer. Color converter approach is quite popular for the-state-of-art LED technology. [77, 78, 79]

Because of novel properties of the NQDs, they are considered as notable candidate materials for color converter layers. Besides providing saturated colors (i.e., narrow emission FWHM), different emission layers can be easily combined to obtain a desired spectrum of light (e.g., white light generation) (see Figure 6.1.1). [80] However, the use of only radiative energy transfer to convert photons emitted from the pump LED is not an efficient process. First, the converter layer has to be thick enough in order to absorb and convert all of the pump photons (i.e., 100% color conversion assumed). Second, the total internal reflection of the pump photons due to refractive index differences between higher refractive index epitaxially grown pump LED and smaller refractive index nanocrystalline converter layer causes considerable amount of loss due to problems related to light coupling.

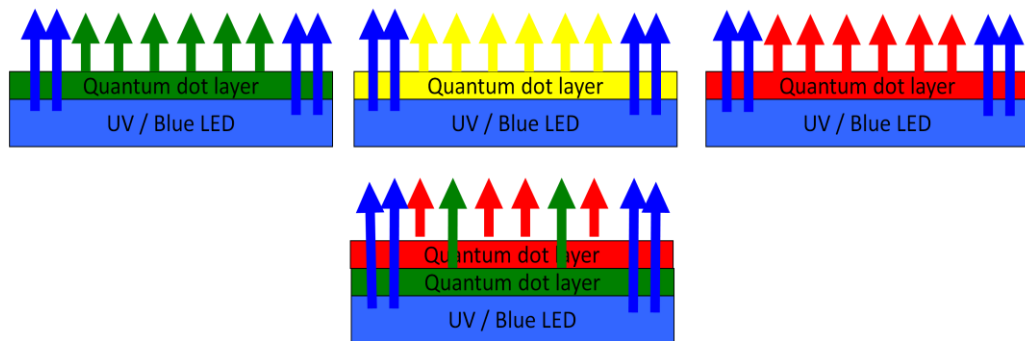


Figure 6.1.1 Color converter light emitting diodes can benefit NQDs as optically active converting materials. Combination of different color emitting NQDs can be used to generate white light.

As an alternative and elegant approach, excitation energy (i.e., electron-hole pairs) in the pump LED can be transferred to the converter layer without emission of a photon, by means of non-radiative energy transfer process, which relies on the dipole-dipole interaction between luminescent materials in close proximity to each other (i.e., a few nanometers), which was first explained by Theodor Förster. [81] The use of non-radiative energy transfer to enhance the color converter layers consisting of NQDs was first shown by Achermann *et al.* with a blue emitting pump LED consisting of a planar multi-quantum-well (MQW) architecture. [82] As previously discussed in detail (see Chapter 4),

non-radiative energy transfer is a distance dependent process. Distance dependence is observed to change for different geometries. The energy transfer between a two-dimensional planar luminescent donor (i.e., a quantum well) and a zero dimensional (i.e., NQD) acceptor is governed by d^{-4} distance dependence, where d is the average donor-acceptor separation. Afterwards, Achermann *et al.* developed a method to increase the efficiency of the nonradiative energy transfer via etching the capping layer lying over the emitting multi-quantum-wells in order to decrease the distance between NQDs and QWs. [83] Nevertheless, in such planar architectures, the use of nonradiative energy transfer is limited due to a few apparent factors: Interaction area between the acceptor NQDs and the donor QWs is limited (see Figure 6.1.2). Also, energy transfer can take place only between the closest monolayer of the NQDs and the top QW since non-radiative energy transfer rates decrease very rapidly with the increasing donor – acceptor separation (>5 -10 nm). Etching of the capping layers to make NQDs and QWs closer is generally unsuccessful and also undesired. Etching of the capping layer deteriorates the electrical properties of the pump LED.

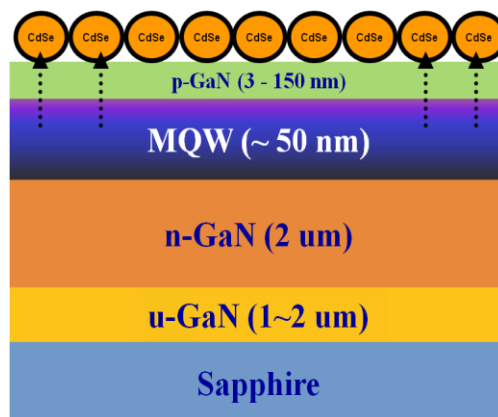


Figure 6.1.2 A similar pump LED and a monolayer of CdSe NQDs used by Achermann *et al.* where they etched GaN capping layer in order to decrease the separation between top QW and monolayer of the NQDs. [83]

6.2 Proposal and Principles of Operation

Non-planar architectures such as one-dimensional nanowires or nanopillars housing QWs could provide large surface-to-volume ratios for QWs as compared to two-dimensional planar structures embedding QWs (see Figure 6.2.2). Increasing the surface area of the luminescent QWs would lead to increased interaction area between NQDs and QWs so that nonradiative energy transfer efficiency between the donor QWs and the acceptor NQDs could be enhanced. More NQDs would have a chance to accept energy from a nearby QW through dipole-dipole coupling mechanism.

Chanyawadee *et al.* [84] coupled NQDs within elliptical holes etched into epitaxially grown InGaN/GaN multi-quantum-wells (MQWs) (see Figure 6.2.1). They have shown that up to 82% efficient energy transfer can take place from MQWs to NQDs due to increased interaction area (see Figure 6.2.1 (a)), they also use elliptical holes with smaller lengths (i.e., holes that cannot reach MQW region) as a negative control group to prove that enhancement in NQD emission is due to energy transfer from MQWs (see Figure 6.2.1(b)).

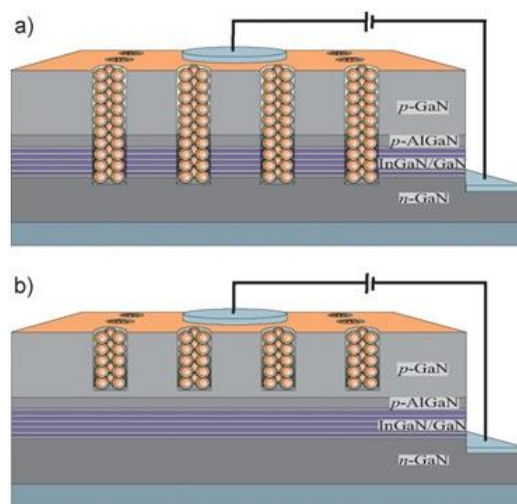


Figure 6.2.1 NQDs elliptically etched holes (a) reaching down to QWs, (b) lying only in p-GaN capping layer. [84] (This figure is reproduced with permission of the publisher John Wiley & Sons Inc.)

In this part of the thesis, we propose the utilization of top-down fabricated InGaN/GaN MQW nanopillars to incorporate with core/shell CdSe/ZnS NQD color converters for enhanced color conversion due to very efficient nonradiative energy transfer that is enabled by the advantages of the nanopillar architecture providing large surface-to-volume ratio for QWs to interact with acceptor NQDs. [85] The proposed architecture is also beneficial in terms of helping to reduce the material usage for the color converter layer due to highly efficient energy transfer.

As shown in Figure 6.2.2, InGaN/GaN MQW nanopillars will be coated with CdSe/ZnS NQDs. The height level of NQDs can be adjusted by tuning the concentration of the incorporated NQD amount so that more than one QW would contribute to the energy transfer and very high efficiency energy transfer dynamics could be attained.

In this part, we only optically pump the MQWs to study the energy transfer dynamics of the proposed architecture. Blue emitting MQWs are excited via another UV laser, then dominant nonradiative energy transfer take place because of increased interaction volume between MQWs and NQDs. Most of the electron-hole pairs (i.e., excitons when they are bound) created in the QWs will be migrated to the NQDs with a transfer rate that can compete very well with the other decay channels in MQWs.

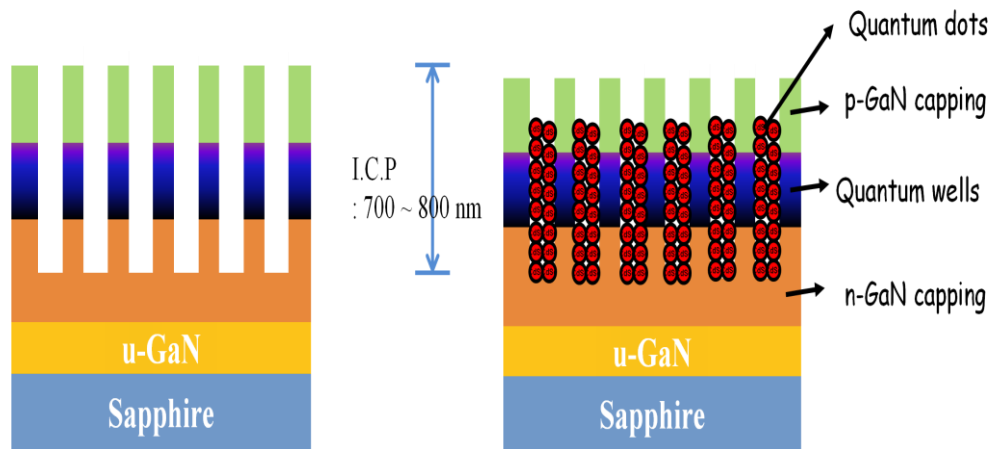


Figure 6.2.2 InGaN/GaN multi-quantum-well nanopillars obtained via inductively plasma reactive ion etching (ICP REI). Inbetween pillars are incorporated NQDs.

Nanopillar architecture would be also advantageous for radiative energy transfer due to enhanced light trapping properties of the nanopillars. Electron-hole pairs, which are recombined in the QWs, can be more efficiently coupled to the NQDs than the coupling in planar architecture. Since nanostructures are on the order of the wavelength of the emitted photons, trapping is more pronounced. As a result, pump photons will be trapped to be absorbed more via NQDs for enhanced color conversion. Yet, due to highly efficient nonradiative energy transfer, most of the electron hole pairs could be coupled to NQDs without emission of a intermediate photon.

6.3 Experiments and Results

Pump LEDs consist of InGaN/GaN MQW epitaxial structures, which are fabricated by our collaborators from Korea-KOPTI (Korea Photonics Technology Institute). The brief explanation of the fabrication procedure of the growth and fabrication is as follows.

Epitaxial structure was grown by metal organic chemical vapor deposition (MOCVD) method. Trimethylgallium (TMGa), trimethylindium (TMIn) and NH₃ were used as precursors for Ga, In and N, respectively. A thermal annealing of c-plane sapphire substrate was performed at 1000 °C for 10 min, followed by the growth of a low temperature GaN buffer layer. A 1 μm thick undoped GaN layer and a 2 μm thick n-type GaN layer were grown at 1060 °C. After that, five pairs of InGaN/GaN MQW were grown on high-quality GaN epitaxial layers and a 150 nm thick p-GaN layer was directly grown on MQW layer.

A 100 nm thick SiO₂ layer and a 10 nm thick Ni mask were deposited on the epi-wafer surface by plasma-enhanced chemical vapor deposition (PECVD) and electron beam evaporator, respectively. This epi-wafer was subsequently annealed under flowing nitrogen at a temperature of 800 °C for 1 min to form Ni clusters. Then, SiO₂ and GaN layers were etched for 120 s and 5 min using an inductively coupled plasma reactive ion etching (ICP-RIE) process. Finally, Ni metal and SiO₂ layers were removed by buffered oxide etchant (BOE). The fabrication steps are schematically explained in Figure 6.3.1.

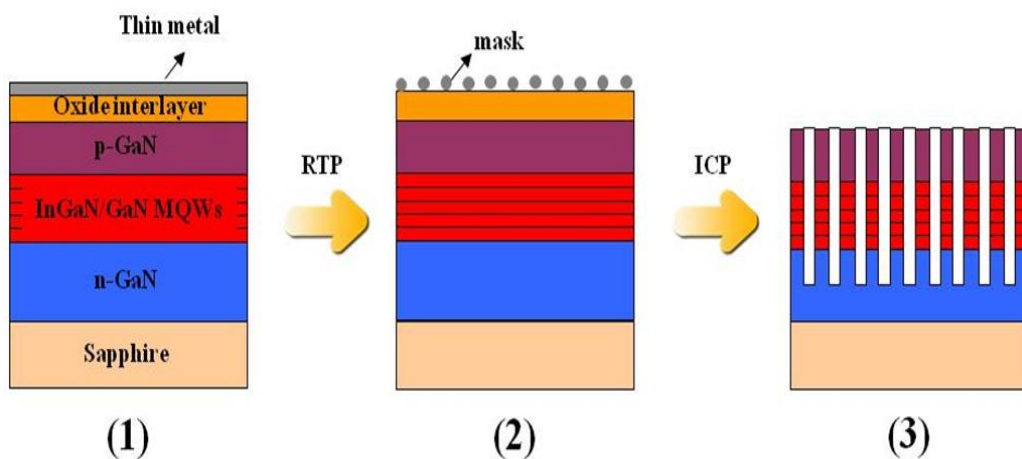


Figure 6.3.1 Explanatory schematics for the fabrication of InGaN/GaN MQW nanopillar structures.

After the fabrication of the nanopillars, we have performed the structural, material and optical characterizations. Scanning electron microscopy images verify the formation of nanopillars as can be seen from Figure 6.3.2.

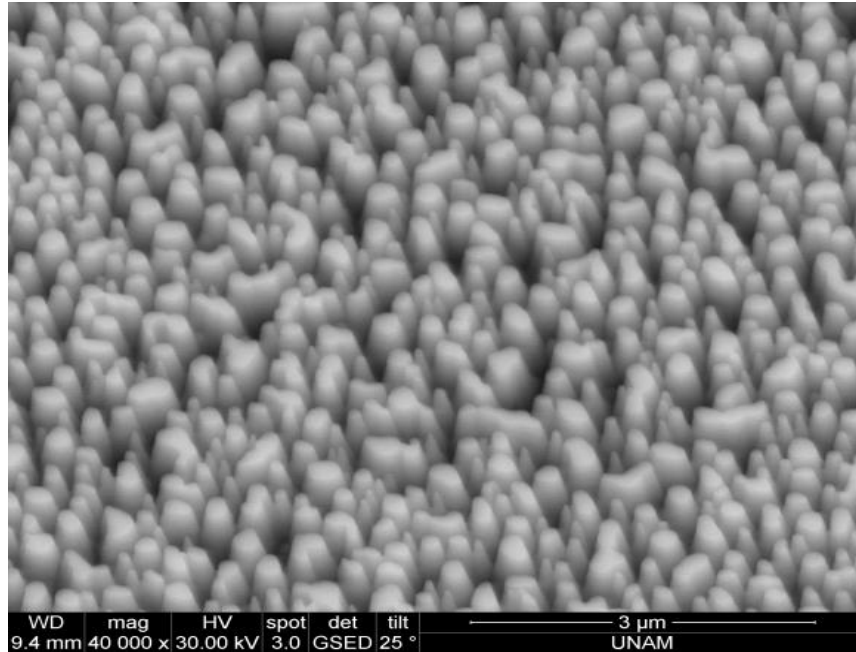


Figure 6.3.2 SEM image of the top-down fabricated InGaN/GaN MQW nanopillars.

X-ray diffraction measurements indicates the formation of crystalline InGaN/GaN MQWs for both planar and nanopillar structures as shown in Figure 6.3.3.

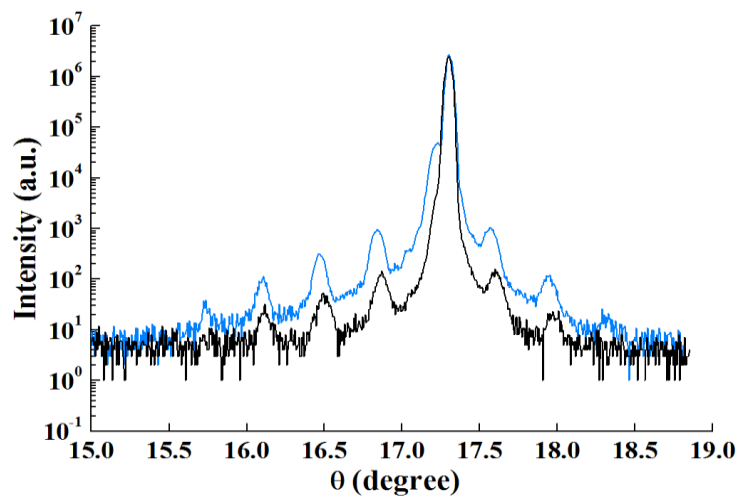
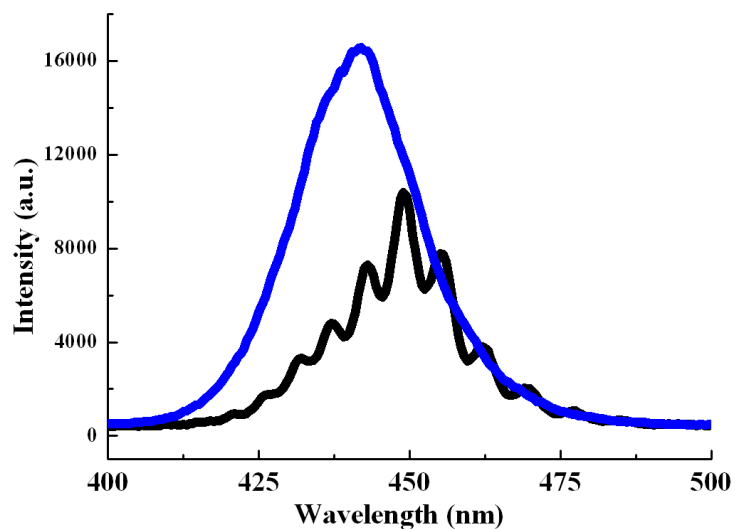
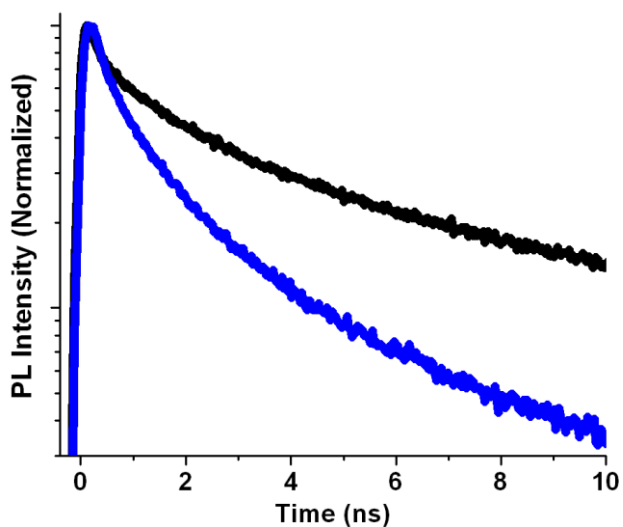


Figure 6.3.3 X-ray diffraction measurement of the nanopillars (blue) and planar (black) architecture.

We also perform steady state and time resolved photoluminescence measurements of the grown InGaN/GaN MQW planar and nanopillar structures, as can be seen in Figure 6.3.4. PL intensity of the nanopillars are blue-shifted and emission intensity is increased as compared to unetched planar architecture's PL spectra. The observed blue shift is attributed to the reduction in the indium content during etching process, which can increase the band gap of the nanopillar MQWs slightly. Enhancement in the absolute PL intensity is attributed to the better light coupling of the nanostructured architecture. [86, 87] Fluorescence lifetime decays shows that nanopillars decay faster than the planar. This can be due to several possible reasons. First, it may be due to increased surface traps, which could increase the nonradiative relaxation channels in the nanopillars. However, since steady state PL emission is observed to be increasing, this could not be the case. The second reason is the strain relaxation, which is also indicated by the observed blue shift in the PL.



(a)



(b)

Figure 6.3.4 (a) Photoluminescence spectra of InGaN/GaN multi-quantum-well planar (black) and nanopillar (blue) structures, and (b) time resolved fluorescence decays for planar (black) and nanopillar (blue).

As acceptors, we have utilized core/shell CdSe/ZnS NQDs of different sizes so that emission wavelength can be tuned in the visible spectrum (i.e., green, yellow and red). NQDs were obtained from Evident Inc. and used without further purification. These NQDs have TOPO ligands and their in-solution

photoluminescence quantum yields are on the order of 40%. Our green-, yellow- and red-emitting NQDs have molecular weights of 94, 140, 270 $\mu\text{g/nmol}$ and their corresponding diameters are ca. 3.3, 3.8, and 5.0 nm with a size dispersion of <5%, respectively. They have an in-solution concentration of 10 mg/mL. Emission and absorption spectra of the NQDs that are incorporated into InGaN/GaN MQW nanopillars are presented in Figure 6.3.5.

To have efficient nonradiative energy transfer between two species (at least one of them being fluorescent): First, the emission spectrum of the donor and absorption spectrum of the acceptor should have a strong match. Second, the distance between species should be as small as possible since nonradiative energy transfer rate scales reciprocal of the distance to the power four to six, depending on the geometry. Quantum yield of the donor and refractive index of the medium are also other factors affecting nonradiative energy transfer rates. In our case, for MQW donors and NQDs acceptors, the spectral overlap is quite high as can be seen from Figure 6.3.5. The spectral overlap between blue emitting MQW nanopillars and red-emitting NQDs allows us to obtain a strong spectral overlap of $4.421 \times 10^{16} \text{ M}^{-1} \text{ cm}^{-1} \text{ nm}^4$ as calculated according to the Förster's formula (see (6.3.7)). Broad absorption spectrum of the NQDs with increasing extinction coefficients towards UV and blue region enables them as efficient energy acceptors for shorter wavelength emitting donors.

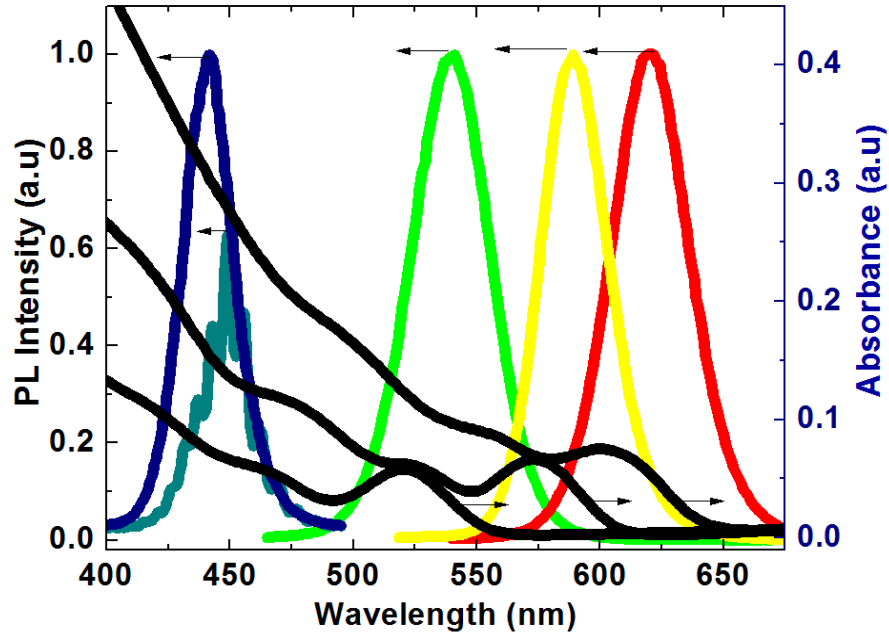


Figure 6.3.5 In-solution PL and absorbance spectra of the utilized CdSe/ZnS NQDs in this part of the thesis. Emission of the planar and nanopillar LEDs are also shown to indicate the spectral overlap between the donor emission and the acceptor absorption.

We have utilized a time resolved fluorescence spectrometer (PicoQuant FluoTime 200) consisting of a time correlated single photon counting system (TCSPC) and a picosecond pulsed laser to measure the photoluminescence lifetimes of the donor QWs and acceptor NQDs in order to study nonradiative energy transfer dynamics between two species. Since nonradiative energy transfer creates a new path for relaxation of the electron – hole pairs in the donor QWs, the donor lifetimes are expected to decrease due to increase in total depopulation rate of the excited state in MQWs (see (6.3.1)). On the other hand, the acceptor NQD lifetimes are expected to be elongated due to energy feeding (see (6.3.2)).

$$k_{relaxation_{QWs}} = k_{radiative} + k_{nonradiative} + [k_{nonradiative\ energy\ transfer}] \quad (6.3.1)$$

$$k_{relaxation_{QDs}} = k_{radiative} + k_{nonradiative} - [k_{nonradiative\ energy\ transfer}] \quad (6.3.2)$$

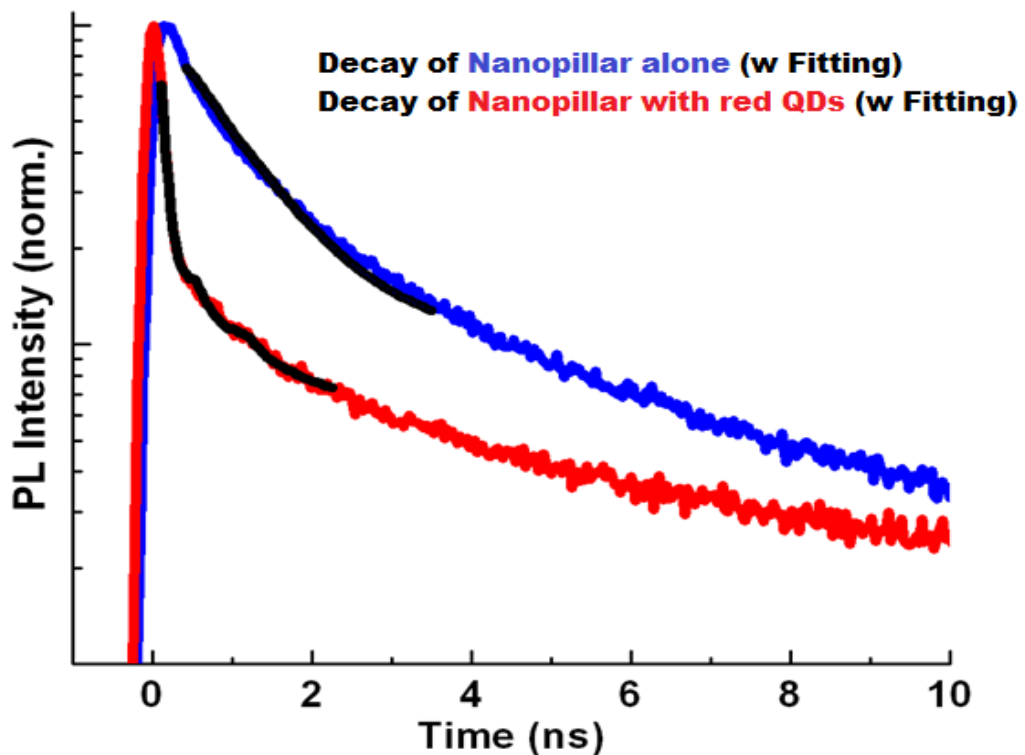
Since our NQDs are in core/shell structure and inorganic protective shells are thick enough to block any direct Drexel-type charge transfer processes between QWs and NQDs, all of the emission kinetics change in the donor lifetime is attributed to the nonradiative energy transfer mechanism.

After incorporation of the NQDs with nanopillar MQWs, the energy transfer efficiencies up to 83.0% with an energy transfer rate of $(0.192 \text{ ns})^{-1}$ could be obtained. According to the experimental results, almost up to 41% of the electron – hole pairs created in the QWs can be transferred to the NQDs through nonradiative energy transfer means. These energy transfer rates and efficiencies could be tuned by changing the spectral overlap and the effective distance via changing the size of the NQDs. We have also theoretically approximated the energy transfer rates using Förster's formalization which gives well matched results with experimental results indicating that the main nonradiative energy transfer pathway between QWs and NQDs is the dipole-dipole coupling.

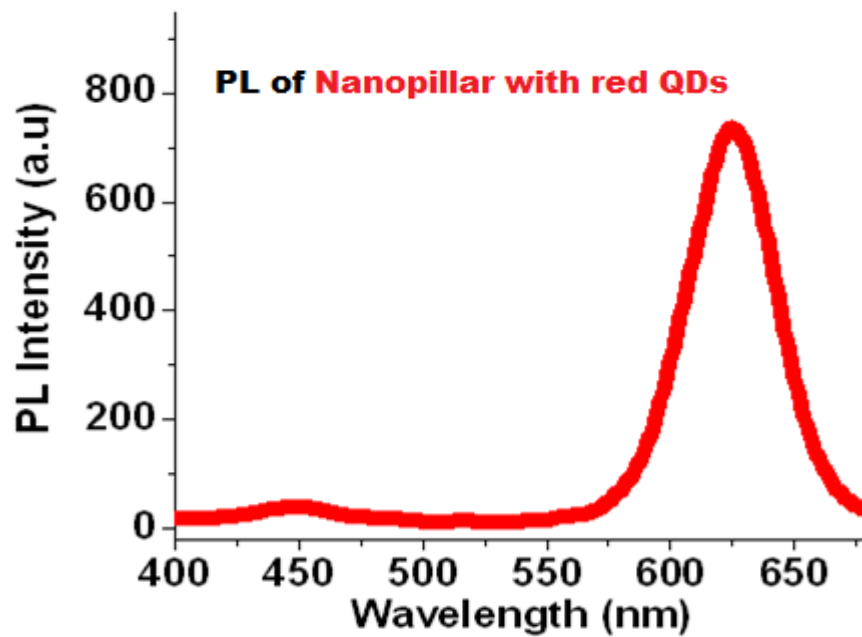
In this part, we have utilized three different sized core/shell CdSe/ZnS NQDs emitting at 540, 590 and 620 nm, separately, with the nanopillar MQWs. Incorporation of these NQDs into nanopillars is performed via drop-casting of the NQDs from the solution phase (i.e., dissolved in toluene) onto pre-cleaned nanopillar substrates (regular solvent cleaning). After drop casting, samples were annealed at 100 °C for 1 hour to evaporate the solvent to end up with thin films of the NQDs in between and on the nanopillars. Coating process was performed in a clean room environment to prevent any unwanted particle (e.g., dust) deposition on nanopillars.

Next, we performed lifetime measurements using our time resolved fluorescence spectrometer, which has an instrument response function (IRF) with a full-width-half-maximum of around 200 ps. As a result, all of the measured decays are convoluted with the system's IRF. While fitting the measured decays, we take IRF into account through deconvolution fitting.

Figure 6.3.6 (a) shows the measured fluorescence decay of the MQWs in the presence and absence of the incorporated red-emitting NQDs. As can be seen, when red-emitting NQDs are introduced, the fluorescence decay of the MQWs becomes faster indicating a strong lifetime modification due to strong nonradiative energy transfer process. In Figure 6.3.6(b) steady state PL emission of the nanopillar MQW sample with hybridized NQDs is shown. Due to efficient nonradiative energy transfer plus radiative energy transfer, almost 100% color conversion is obtained except for a weak emission of the MQWs at blue region.



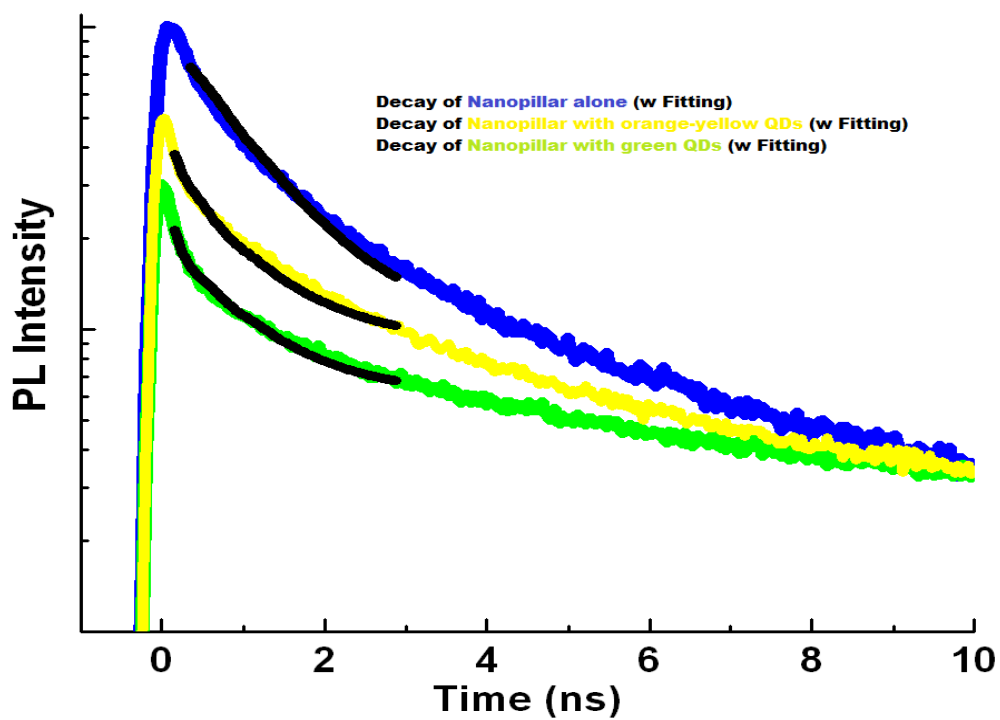
(a)



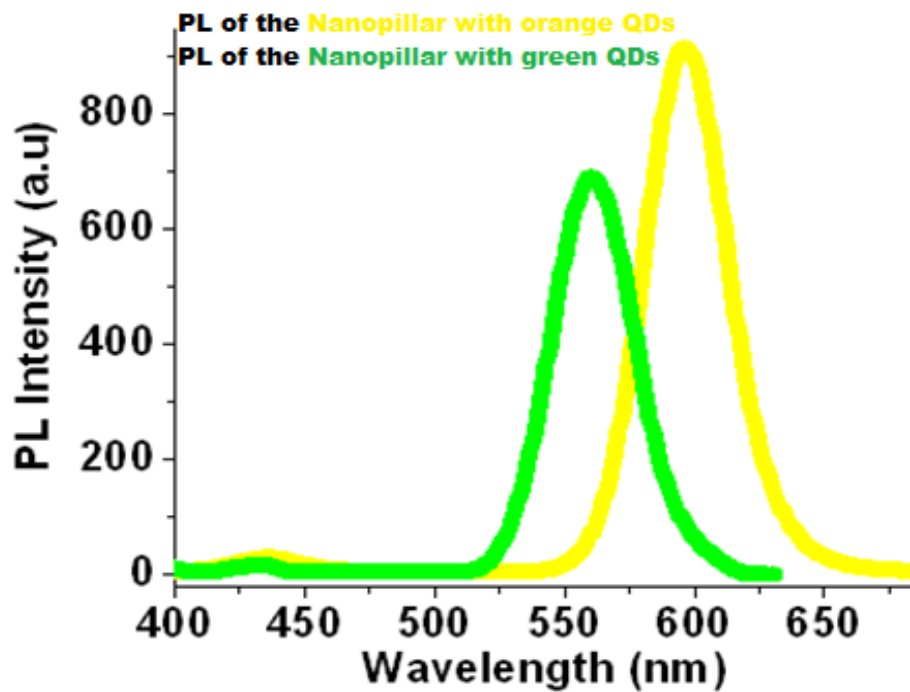
(b)

Figure 6.3.6 (a) Time resolved fluorescence decays of multi-quantum-wells in nanopillar architecture with and without red NQDs along with exponential fits. (b) Steady state PL spectrum of the nanopillar NQD hybrid using red NQDs.

In Figure 6.3.7(a) we present fluorescence decays of the MQWs when nanopillars are incorporated with shorter wavelength emitting NQDs (i.e., orange and green). The decays are plotted for different peak photon counts. We observe that, although spectral overlap decreases due to utilization of smaller NQDs having blue shifted absorption onset (see Figure 6.3.5), there is still a considerable amount of lifetime modification in the donor emission kinetics. Also, Figure 6.3.7(b) shows the steady state PLs of the MQW nanopillars hybridized with green and orange emitting NQDs, where almost 100 % color conversion can again be achieved due to efficient energy transfer.



(a)



(b)

Figure 6.3.7 (a) Time resolved fluorescence decays of multi-quantum-wells in nanopillar architecture with and without green and yellow NQDs along with their fit exponential fits. (b) Steady state PL spectra of the nanopillar NQD hybrids using yellow and green NQDs.

Measurement results are analyzed to deduce the energy transfer dynamics. Decay of the MQWs in the absence of NQDs are fitted with single exponential decays as given by (6.3.3). Total relaxation rate of the MQWs is given in (6.3.4).

$$I_{nanopillar\ MQWs\ alone} = A \exp\left(-\frac{t}{\tau_{donor_alone}}\right) \quad (6.3.3)$$

$$\frac{1}{\tau_{donor_alone}} = \kappa_{radiative} + \kappa_{nonradiative} \quad (6.3.4)$$

We model the emission kinetics of the donor QWs in the presence of acceptors as follows: Electron-hole pairs, which are close to the surface of the nanopillars, are also close to the NQDs so that they are more prone to be migrated to NQDs via nonradiative energy transfer. However, electron-hole pairs, which are created away from the surface of the nanopillars, will not be transferred at all, if they are quite far away (e.g., larger than twice of the Förster radius where efficiencies drop only to a few percent). As written in (6.3.5), we discriminate between the electron-hole pairs of the MQWs by dividing them into two: transferring and not transferring electron-hole pairs. Not transferring electron-hole pairs will continue to decay with their original decay rates as in the case of MQWs alone, however most of the electron-hole pairs close to the surface of the nanopillars will decay at a faster rate due to nonradiative energy transfer (see (6.3.5)).

$$I_{nanopillar\ MQWs\ with\ QDs} = A_1 \exp\left(-\frac{t}{\tau_{donor_alone}}\right) + A_2 \exp\left(-\left(\frac{1}{\tau_{donor_alone}} + \frac{1}{\tau_{energy\ transfer}}\right)t\right) \quad (6.3.5)$$

Donor MQW emission in the absence of NQDs are fitted using (6.3.3). In the presence of NQDs, MQW decays are fitted using (6.3.5). After obtaining the rates from the fittings, energy transfer efficiency can be calculated using (6.3.6).

$$\eta_{Energy_transfer} = \frac{\kappa_{ET}}{(\kappa_{ET} + \kappa_{donor_alone})} \quad (6.3.6)$$

Fitting the decay curves for MQWs in the absence and presence of the NQDs, we obtain the transfer rates and efficiencies as shown in Table 6.3.1. Percent of the transferred electron-hole pairs are obtained from the ratio of amplitudes which represent ‘transferring’ and ‘not transferring’ electron-hole pairs: $A_2 / (A_1 + A_2)$ from (6.3.5).

Sample	$k_{\text{total}} (\text{ns})^{-1}$	$k_{\text{ET}} (\text{ns})^{-1}$	Transfer efficiency (%)	Percent of transferred e-h pairs
Nanopillar alone	$(0.944)^{-1}$	-	-	-
Nanopillar + red NQDs	-	$(0.192)^{-1}$	83	41
Nanopillar + orange NQDs	-	$(0.237)^{-1}$	79.8	39
Nanopillar + yellow NQDs	-	$(0.253)^{-1}$	78.8	39

Table 6.3.1 Total decay rate for nanopillar alone and energy transfer rates, efficiencies and percent of transferred electron-hole pairs for red, orange and yellow emitting NQDs incorporated into nanopillars are shown.

To understand the underlying physics, we modify Förster’s formulation of energy transfer to adapt our case. We check whether nonradiative energy transfer dynamics can be explained by only dipole-dipole coupling or not. (6.3.7) is the classical formula for the calculation of spectral overlap between donor emission and acceptor absorption. Here F_D is the normalized emission of the donor and ε is the extinction coefficient of the acceptor.

$$J = \int_0^{\infty} F_D(\lambda) \varepsilon(\lambda) \lambda^4 d\lambda \quad (6.3.7)$$

After obtaining the spectral overlap J , Förster radius can be calculated using (6.3.8).

$$R_0 = 0.211 (\kappa^2 n^{-4} Q_D J)^{\frac{1}{6}} \quad (6.3.8)$$

R_0 is the Förster radius (nm) where energy transfer efficiency drops to 50% when the donor and acceptor are separated by that distance. Here κ is the dipole orientation factor, which is taken to be 2/3 for randomly oriented dipoles. n is the refractive index of the medium. Q_D is the quantum yield of the donor alone and J is the spectral overlap.

Energy transfer rate is presented in (6.3.9).

$$k_{ET} = k_{donor\ alone} \left(\frac{R_0}{r} \right)^6 \quad (6.3.9)$$

When we take into account the computation of two dimensional QW donor to the distribution of NQDs, we drive(6.3.10) where we can estimate the energy transfer rates. Here d is the average separation between the donor and acceptor and σ is the absorption cross-section of the acceptor NQDs. Here is the derivation given as follows.

$$\begin{aligned} k_{ET} &= k_D \left(\frac{R_0}{R} \right)^6 \\ k_{ET} &= \sigma \int_0^\infty k_{ET} dS \\ k_{ET} &= k_D \sigma R_0^6 \int_0^\infty \frac{2 \pi \rho}{(d^2 + \rho^2)^3} d\rho \\ k_{ET} &= k_D \sigma R_0^6 2\pi(-1) \left[\frac{1}{4(d^2 + \rho^2)^2} \right]_0^\infty \\ k_{ET} &= \frac{k_{donor\ alone} 0.5 \pi \sigma R_0^6}{d^4} \end{aligned} \quad (6.3.10)$$

Using (6.3.10), we extract energy transfer rate. R_0 , d , σ are either calculated, estimated or taken from the literature. The rate of donor alone decay is known

experimentally. In Table 6.3. 2, we present the experimental and theoretical results together.

Sample	k_{ET} experimental	k_{ET} theoretical	J - spectral overlap	n - refractive index	d separation	σ - absorption crosssection
+ red NQDs	$(0.192 \text{ ns})^{-1}$	$(0.197 \text{ ns})^{-1}$	4.421×10^{16} $M^{-1}cm^{-1}nm^4$	1.934	4 nm	2.100×10^{12} cm^2
+orange NQDs	$(0.237 \text{ ns})^{-1}$	$(0.230ns)^{-1}$	1.491×10^{16} $M^{-1}cm^{-1}nm^4$	1.894	3.5 nm	2.872×10^{12} cm^2
+yellow NQDs	$(0.253 \text{ ns})^{-1}$	$(0.248 \text{ ns})^{-1}$	4.933×10^{15} $M^{-1}cm^{-1}nm^4$	1.874	3 nm	4.164×10^{12} cm^2

Table 6.3. 2. Experimental and theoretical energy transfer rates are compared. Other parameters used for the calculation of the theoretical rates are also given (J, n, d, and σ).

The values of n are approximated from [88, 89] to find R_0 . Size of the NQDs changes their effective refractive index. Use of smaller size NQDs results in a reduced refractive index. Spectral overlaps are calculated using emission spectra shown in Figure 6.3.4 and approximated values for the extinction coefficients of the NQDs. Average donor-acceptor separation (d) is approximated using the knowledge of the physical quantities. Ligands of the NQDs have lengths of around 1 nm and inorganic ZnS shell is about 0.6 nm. By changing the core size, we could effectively tune separation.

Theoretical values for energy transfer rates turn out to be quite coherent with the experimental values. We conclude that nonradiative energy dynamics between MQWs and NQDs in a nanopillar architecture can be explained only by Förster-like dipole-dipole coupling mechanisms.

6.4 Conclusions

To sum up, we have proposed and showed a novel color converter architecture consisting of CdSe/ZnS core/shell NQDs and nanopillar InGaN/GaN MQWs where the principle of operation of the hybrid system relies mainly on the

mechanism of nonradiative excitation energy transfer. The efficiencies achieved for the energy transfer between the pump MQWs and NQDs outperform the previous efforts in the literature to the best of our knowledge.

Novel nanopillar architecture is exploited due to increased surface-to-volume ratio of the QWs, which enables a larger interaction volume between NQDs and QWs. Also, more than one QW can contribute to the energy transfer. As a result, we observe a significantly enhanced nonradiative energy transfer efficiencies in our proposed system. We have also shown that we can tune the rate and efficiency of the energy transfer via changing the size of NQDs and thus the emission wavelength of the NQDs. We also checked on the underlying physics behind the efficient energy transfer process driving a new formulation for Förster-like dipole-dipole coupling. Theoretical and experimental results show an excellent agreement, which indicates that nonradiative energy transfer takes place mainly due to dipole-dipole coupling between MQWs and NQDs. Future work will include the design and optimization of electrically driven nanopillar MQWs integrated with NQDs.

Chapter 7

Specifically anchored polymer - quantum dot hybrids: Temperature dependent nonradiative energy transfer dynamics for excitonically pumped quantum dot based light emitting diodes

This chapter is based in part on the publication “Temperature dependent non-radiative energy transfer dynamics between specifically functionalized conjugated polymer and core/shell quantum dot nanocrystals for excitonically pumped quantum dot based light emitting diodes” **B. Guzelturk**, P. L. Hernandez-Martinez, D. Tuncel, and H. V. Demir, (to be submitted - 2011).

7.1 Introduction and Motivation

Colloidally synthesized semiconductor quantum dot nanocrystals are superior luminescent materials owing to their size tunable emission spectra, high photoluminescence quantum yields, narrow emission full-width-at-half-maximums (FWHMs) and increased environmental stabilities. [90, 91] These properties feature nanocrystal quantum dots (NQDs) as promising materials for light emitting device applications. Utilization of NQDs in light emitting diodes (LEDs) are commonly realized with two different approaches. Conventional

color converter method can employ NQDs as optically active materials, as also studied in this thesis (see Chapter 6). The alternative electrically active utilization approach aims of benefiting NQDs in electrically active layers of the LEDs, also known as QD-LEDs [91, 92, 93] There have been a lot of efforts to improve QD-LEDs, though most popular excitation method is still injection of charge through tunneling, which is not quite effective due to poor electrical properties of the NQDs. Although colloiddally synthesized core/shell NQDs with stabilizing organic ligands exhibit high quality optical properties, those organic ligands pose large potential barriers against injection of the charges into NQDs. [94, 95] Also, balance of the charge injection can be problematic due to electron affinity – ionization energy level differences with the adjacent injection layers, which could cause charging of the NQDs with subsequent Auger recombination of the excitons via non-radiative means. [96]

As a paradigm shift, QD-LEDs can be driven by direct exciton injection instead of conventional charge injection. In order to inject excitons into NQDs, non-radiative energy transfer means could be employed. Previously, exciton injection via nonradiative energy transfer has been profited for color converter LEDs making use of NQDs. [97, 98] Efficiency of the color conversion was shown to be enhanced via exciton injection through nonradiative energy transfer means as a complementary route to only radiative transfer of the excitation in the pump LED.

In order to effectively use exciton injection scheme in electrically active devices, selection of the material system comes into prominence. Hybrids consisting blends of conjugated polymers and quantum dots can be good candidates thanks to their combined optical and electrical properties and their ease of solution processing methods. Many aspects of these organic-inorganic hybrid material systems have been studied including surface chemistry, mechanical properties, charge separation and charge transport, [99, 100, 101] though understanding of the exciton related interactions in these hybrid systems still need to be extended.

7.2 Proposal and Principles of Operation

In this work, we propose a hybrid material system consisting of core/shell NQDs specifically hybridized with side-group functionalized polyfluorene (PF) derivative conjugated co-polymer. Specific hybridization is useful for reducing phase segregation between the polymer and NQDs when made into thin films. We study nonradiative energy transfer dynamics in hybrid films through investigation of temperature dependent, time resolved fluorescence measurements. We observe that loading level of the NQDs in the hybrids causes different temperature dependent energy transfer efficiency dynamics. In order to explain these differences due to NQD loading, donor fluorescence decays are modeled using Loring-Anderson-Fayer (LAF) and Gösele models. We also have proposed a simple model to understand the underlying physics. A significant cause of the differences in energy transfer trends have been studied in the context of exciton diffusion in the conjugated polymers. As we have observed temperature activated diffusion kinetics in the polymer from the results of the model similar to previous observations for the same polymer family. [102] Moreover, we have shown that effects of exciton diffusion are acceptor loading dependent. Increased number of NQDs in the hybrid is shown to be reducing the effects of diffusion due to increased donor-acceptor interactions and isolation of the donor polymers from each other, which limits the exciton diffusion in the organic part so that almost temperature independent energy transfer efficiency trend has been obtained for highly loaded hybrids.

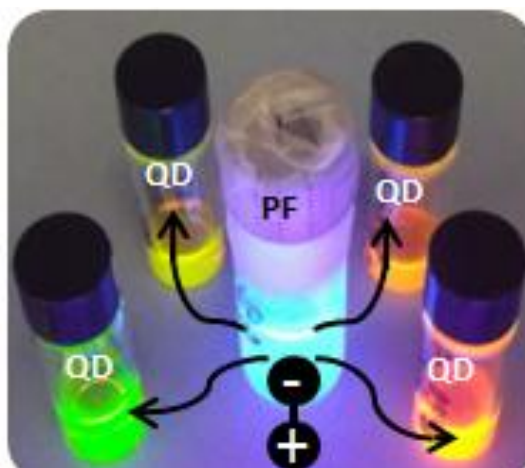


Figure 7.2.1 Five different vials containing functionalized polyfluorene (PF) derivative copolymer emitting in blue and our own-synthesized core/shell NQDs of different sizes and emission wavelengths (green to orange). Functionalized PF is depicted as donating its excitons to the NQDs.

As shown in Figure 7.2.1, functionalized PF emits blue light under UV light illumination and our core/shell NQDs emit at their emission wavelength spanning almost whole visible except blue by changing the size. In Figure 7.2.1 illustration of the exciton transfer from functionalized PF to NQDs is shown.

The principle of operation of these devices is similar to organic light emitting diodes, where an active layer consisting of proposed organic-inorganic hybrid is sandwiched between electron injecting aluminum and hole injecting PEDOT:PSS-ITO layers, as shown in Figure 7.2.2, along with the photography of a fabricated device. Electrically injected charge carriers are combined in the polymer matrix to form excitons. Then, these excitons can be either recombine in the polymer to give electroluminescence at the polymer's emission wavelength, or they can be transferred to NQDs via nonradiative energy transfer with the assist of exciton diffusion in the polymer so that electroluminescence of NQDs is obtained via exciton pumping. The principle of operation of the proposed exciton pumped QD-LEDs is schematically shown in Figure 7.2.3.

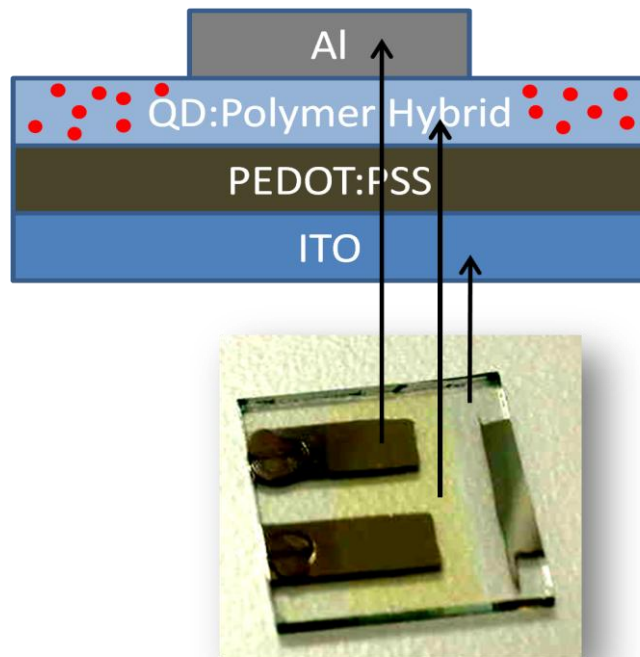


Figure 7.2.2 Schematic of the QD-LED device architecture with the actual photograph of a fabricated device.

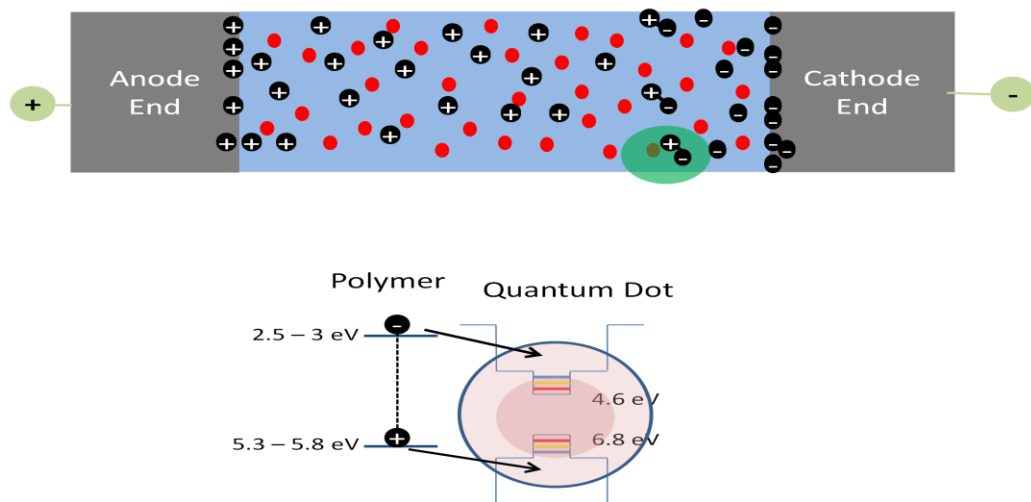


Figure 7.2.3 Schematic for the principle of operation of the exciton pumped QD-LEDs where electrons ‘-’ and holes ‘+’ are injected from cathode and anode, respectively. Also, red dots represent the hybridized NQDs. Due to finite mobility of the charges in the polymer matrix, they are combined to form excitons, which can be effectively transferred to the NQDs via nonradiative energy transfer.

The advantages of the excitonic pumping of QD-LEDs would be as follows. First, conjugated polymers possess electrically superior properties as compared to the NQDs so that electrical injection into polymers is much easier and more efficient. [103] Since we are utilizing core/shell NQDs, charge transfer between polymer and NQD is a weaker process as compared to dominant nonradiative energy transfer. [111] For this reason, charging of the NQDs will be minimized due to balanced injection of the charges in the form of excitons, which will subsequently minimize the following Auger recombination. Fine tuning of the exciton injection could be achieved via choosing the material and optical properties of the organic and inorganic parts so that specific designs for requested emission spectra could be performed.

We have fabricated and showed the proof of concept QD-LEDs using the proposed active layers to exploit excitonic pumping method. Although we suffered from degradation of the materials in ambient environment during fabrication processes and absence of the proper injection layers for conjugated polymer matrix, external quantum efficiencies of the devices are on the order of a few percent. Also, electroluminescence spectra of the devices resulted in almost pure NQD emission by tuning the exciton pumping for strong energy transfer.

7.3 Temperature dependent nonradiative energy transfer dynamics

Previously, there have been some reports discussing the excitation energy transfer in similar material systems. [104, 105, 106] Störfle *et al.* have discussed about the contribution of exciton diffusion to the energy transfer for relatively low concentration of NQDs in the polymer since they have observed severe phase segregation between their polymer and NQDs at high concentrations.

[105] Lutich *et al.* have discussed the effects of the morphology (i.e., layer-by-layer assembled) to the suppression of the exciton diffusion in the organic part so that polymer will become more efficient. [106] Still, developing a further understanding of the exciton involving processes in these organic-inorganic hybrid systems is important to engineer hybrid devices such as QD-LEDs alternatively pumped via exciton injection.

In this part of the thesis, we will mainly discuss the effects of NQD loading and temperature on the nonradiative energy transfer dynamics in thin films of specifically hybridized conjugated polymer and NQDs hybrids. We will figure out the underlying physics behind the observed trends.

Phase segregation between different materials when made into thin films is a known phenomenon where materials are separated into different spatial phases when cast into solid films (see Figure 7.3.1). Phase segregation can take place due to chemical incompatibility such as miscibility differences and solvent effects between two species. [107, 108] While studying the excitonic processes between organic-inorganic material systems, phase segregation is undesired. First, it reduces the interaction area between the organic and inorganic materials so that inter-material processes become limited. Second, the physics and the dynamics of the processes become difficult to understand due to reproducibility problems. In our proposal, formation of homogenous films of NQDs in polymer matrix is vital, since exciton pumping to be efficient, NQDs and polymer should have a great interaction volume.

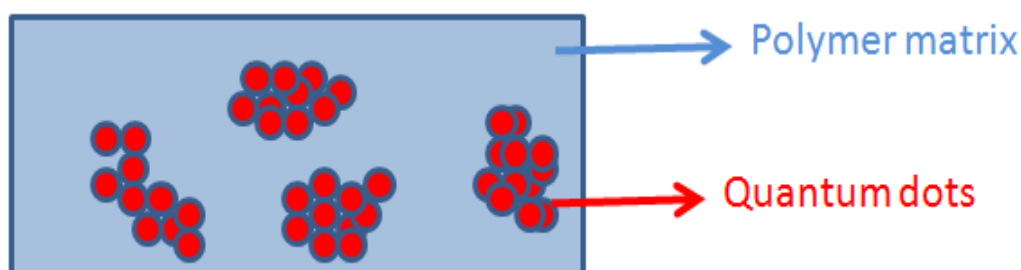


Figure 7.3.1 Schematic depiction of phase segregation between NQDs and polymer.

Since blends of organic and inorganic materials have no specific chemical or physical interaction between them, it is not possible to guarantee reproducible and homogenous thin films. Therefore, different hybridization schemes have been utilized to obtain hybrid organic-inorganic material systems. Polymers that are functionalized with reactive groups can encompass NQDs through surface binding affinities of the functional reactive groups. [108] Alternatively, NQDs can be synthesized in desired polymeric host medium so that they become the ligands of the synthesized NQDs. [109] Ligand exchange of the NQDs can also be performed with monomers, oligomers or polymers. [110] Finally, electrostatic interactions between electro-active ligands having NQDs and polyelectrolyte polymers can be utilized to obtain robust organic-inorganic hybrids exploiting layer-by-layer coatings. [111] However, some of the techniques described above are not suitable for optoelectronic applications since these treatments can be detrimental to the desired photophysical and electronic properties of the NQDs. Ligand exchange free means would render hybrid systems more suitable for optoelectronics since initial properties of NQDs will not be degraded.

Chemical groups such as amines, carboxylic acids, and thiols are generally benefited because of their high surface binding affinities. In our study, hybridization takes place through surface binding affinity of the carboxyl group functionalized polyfluorene (PF) co-polymer, which binds to the core/shell alloy-like CdSe/CdS/ZnS NQDs. [107, 108] Functionalized PF co-polymer with carboxyl groups on its side chain was synthesized by our collaborator Prof. Donus Tuncel's Lab at the Department of Chemistry. The structure of the polymer is given in Figure 7.3.2.

In our labs, we have synthesized core/shell alloy-like CdSe/CdS/ZnS NQDs using a recipe similar to the one described in Ref. 112. Synthesis of the NQDs are explained in detail in Chapter 3.

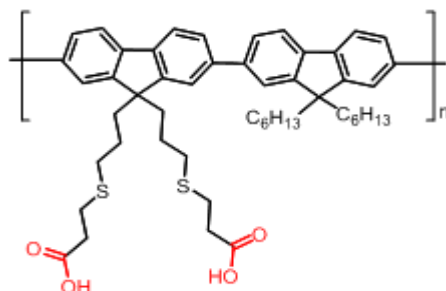


Figure 7.3.2 Carboxyl group functionalized polyfluorene derivative co-polymer.

As a negative control group, we utilized another PF derivative co-polymer having no special functionalization to show and compare the phase segregation tendencies of the NQDs in non-functional polymers. Non-functional PF is obtained from American Dye Source (ADS 232 GE) with its chemical structure shown in Figure 7.3.3.

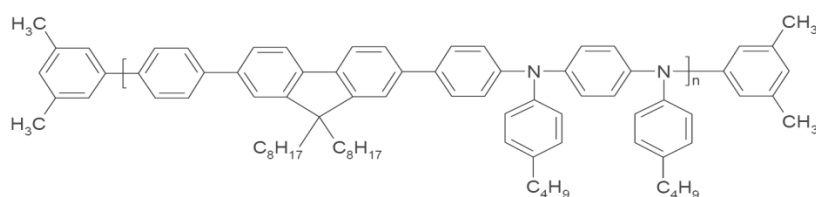
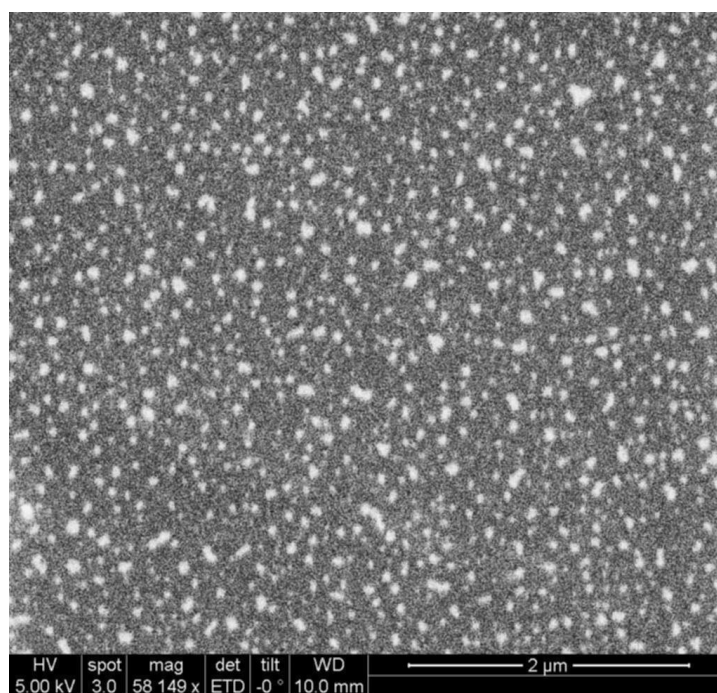


Figure 7.3.3 Non-functionalized polyfluorene derivative co-polymer used as a negative control group.

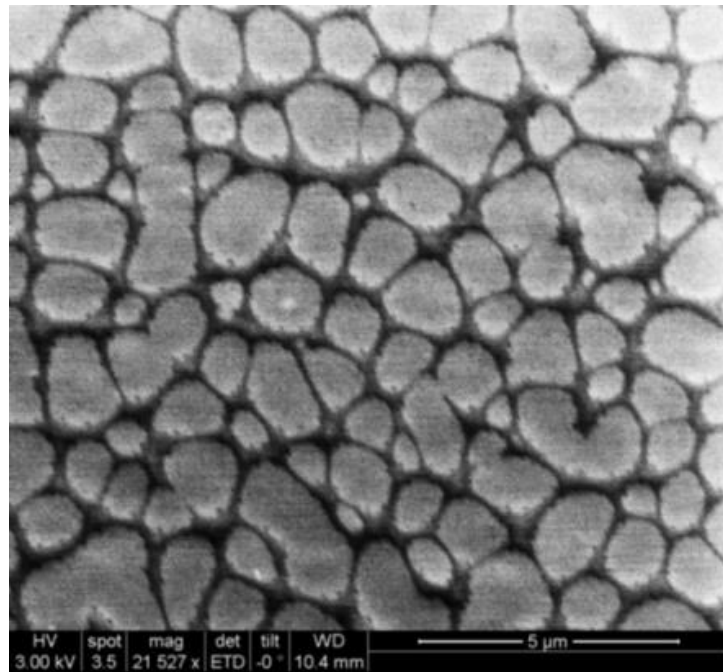
Thin film properties of the functionalized PF - NQD hybrids and non-functionalized PF - NQD blends are examined using scanning and transmission electron microscopies, SEM and TEM, respectively. Also, atomic force microscopy was used to determine topography of the films. Thin films of the hybrids and blends were prepared via spin coating on pre-cleaned silicon substrates for SEM imaging. As shown in Figure 7.3.4 (a)-(d) non-functionalized PF - NQD blend films suffer from severe phase segregation. Although NQD loading is kept as small as possible (i.e., 3w%), sub-micron phase segregations are still observable (see Figure 7.3.4 (a)). For increased concentration of NQDs in these blend thin films (i.e., ~ 30w% and ~ 60 w%) as shown in Figure 7.3.4 (b)-(c), the degree of segregation increases. Using energy

dispersed spectrometer module (EDAX) with our SEM system, we observed that dark regions in Figure 7.3.4 (a)-(d) mostly consist of segregated polymers and bright regions, mostly of NQDs. Due to this severe phase separation tendency between non-functionalized PF and NQDs, optical and electrical properties of these blend thin films were not reproducible.

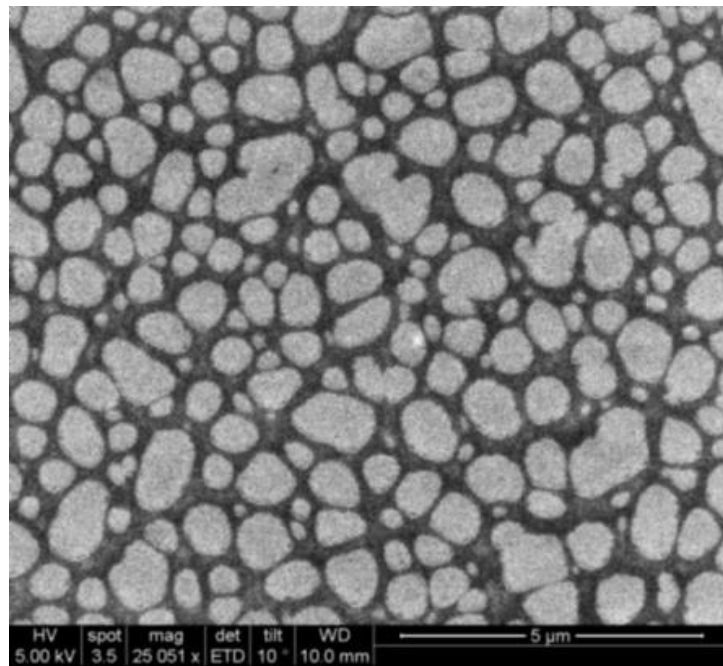
On the other hand, we do not observe any significant indication of the phase segregation from SEM images of the functionalized PF-NQD hybrid films (see Figure 7.3.4 (e)). Thanks to chemical interaction between two species, homogenous thin films are formed and phase segregation is minimized. Again, material analysis using EDAX gave almost the same material distribution from different parts of the films, indicating homogeneity of the resulting hybrid films.



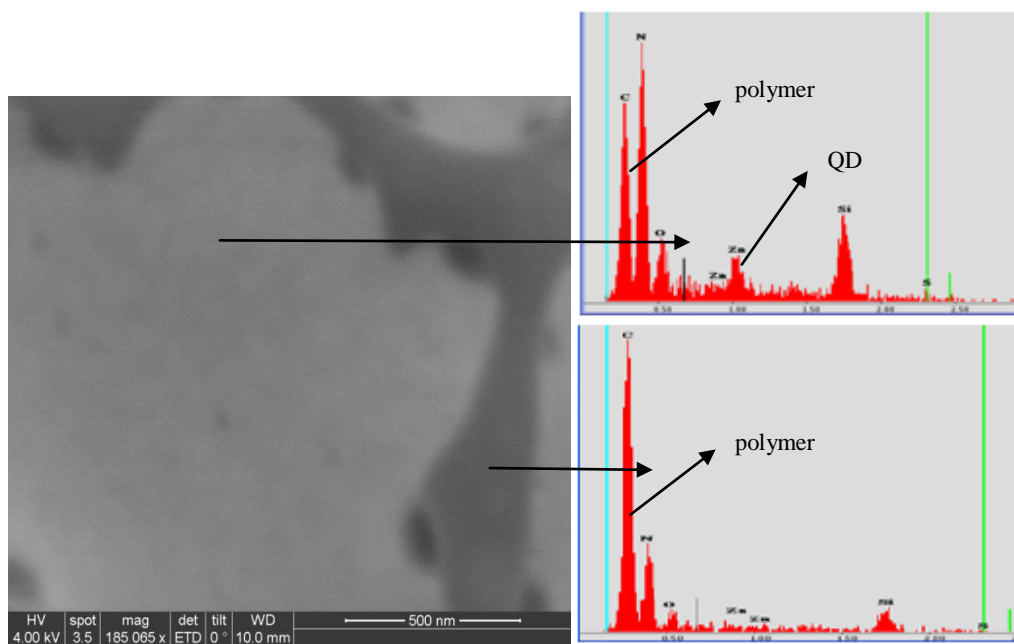
(a)



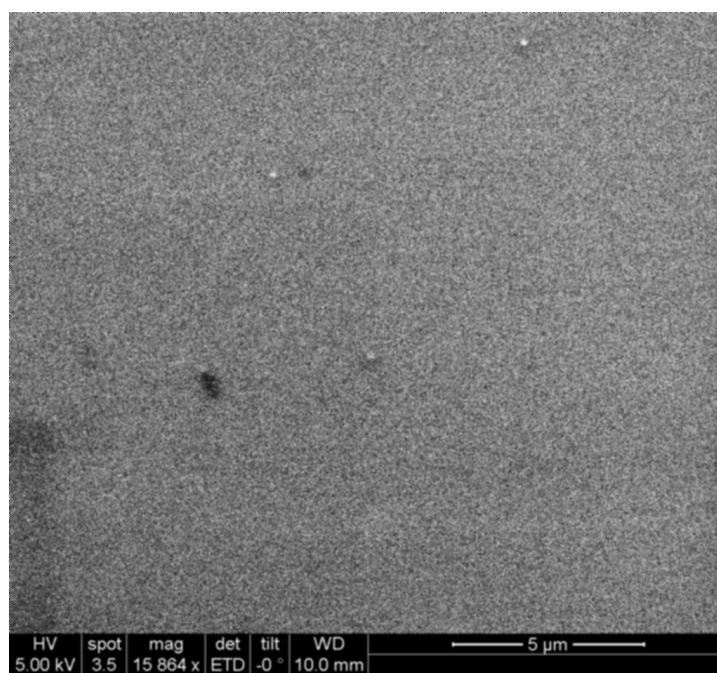
(b)



(c)

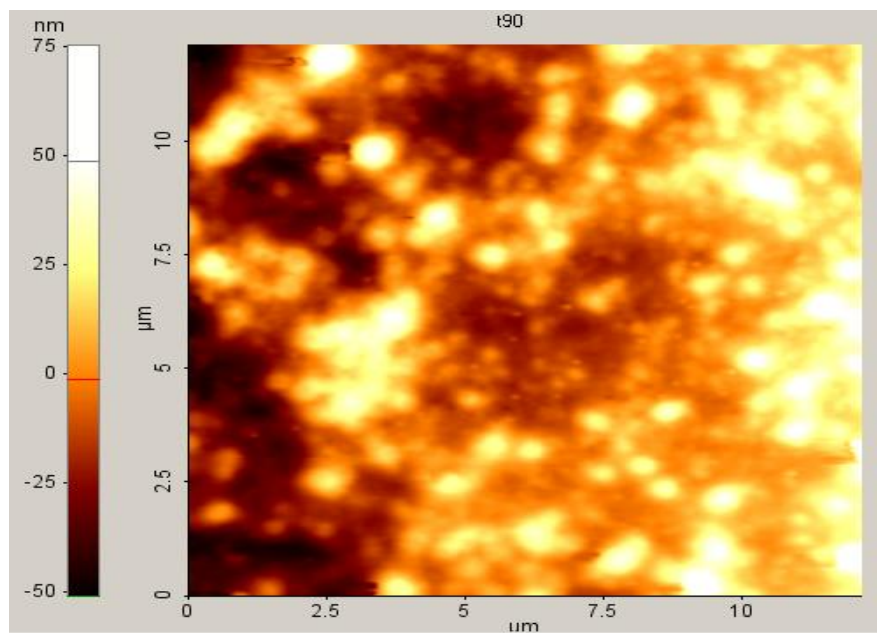


(d)

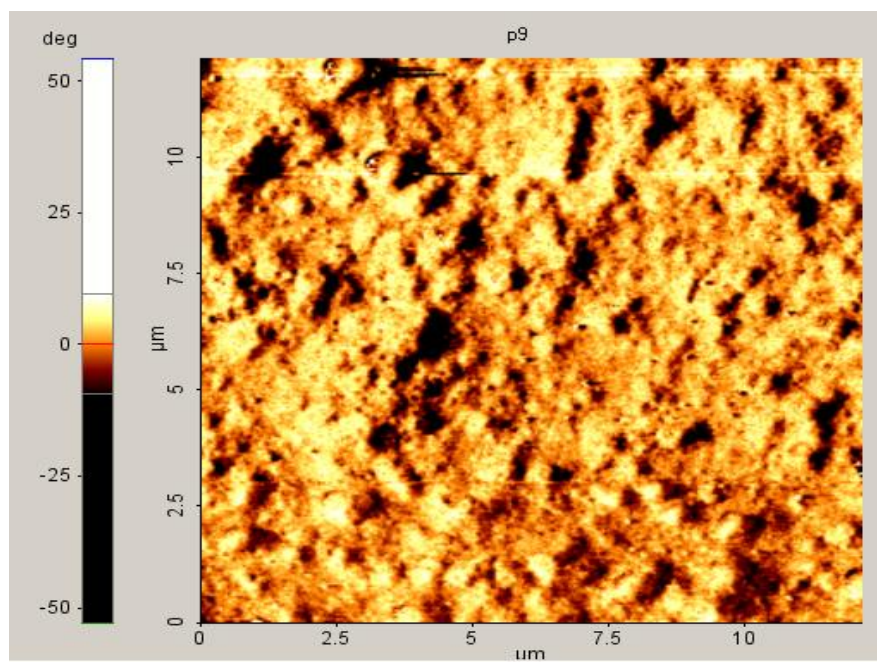


(e)

Figure 7.3.4 SEM images of thin films of (a)-(d) NQDs with non-functionalized PF blends shown with material EDAX analysis of the segregated parts of the films in (d), and (e) NQDs with functionalized PF hybrids.



(a)



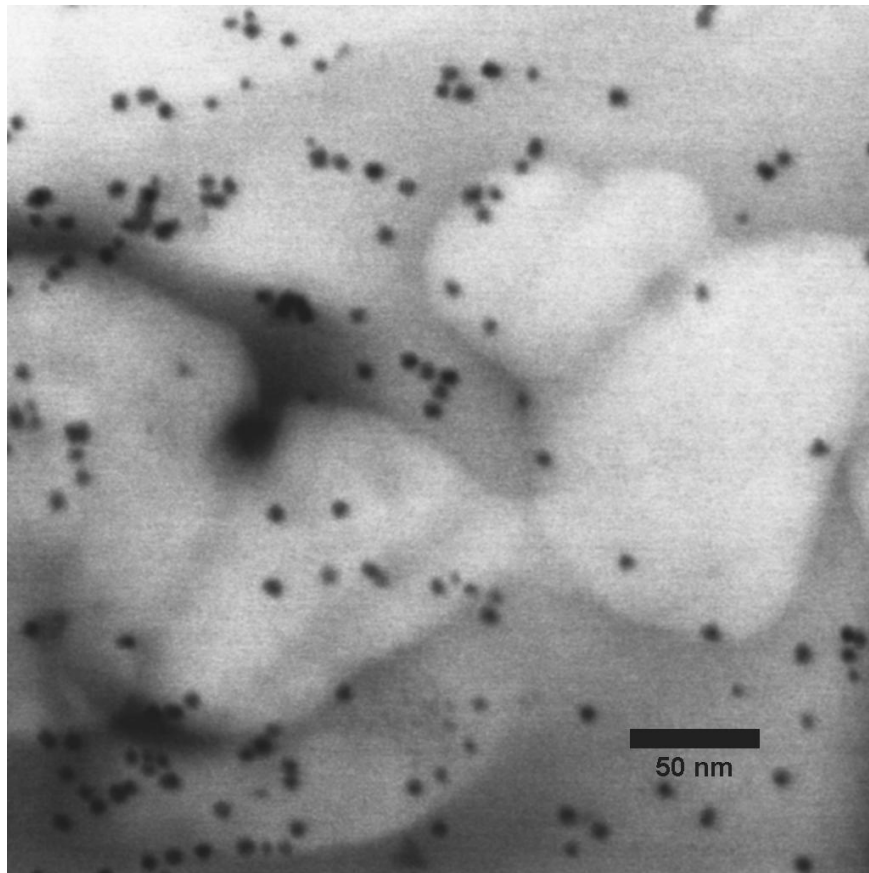
(b)

Figure 7.3.5 Atomic force microscopy images of non-functionalized PF-NQD blends: (a) topography, and (b) phase image.

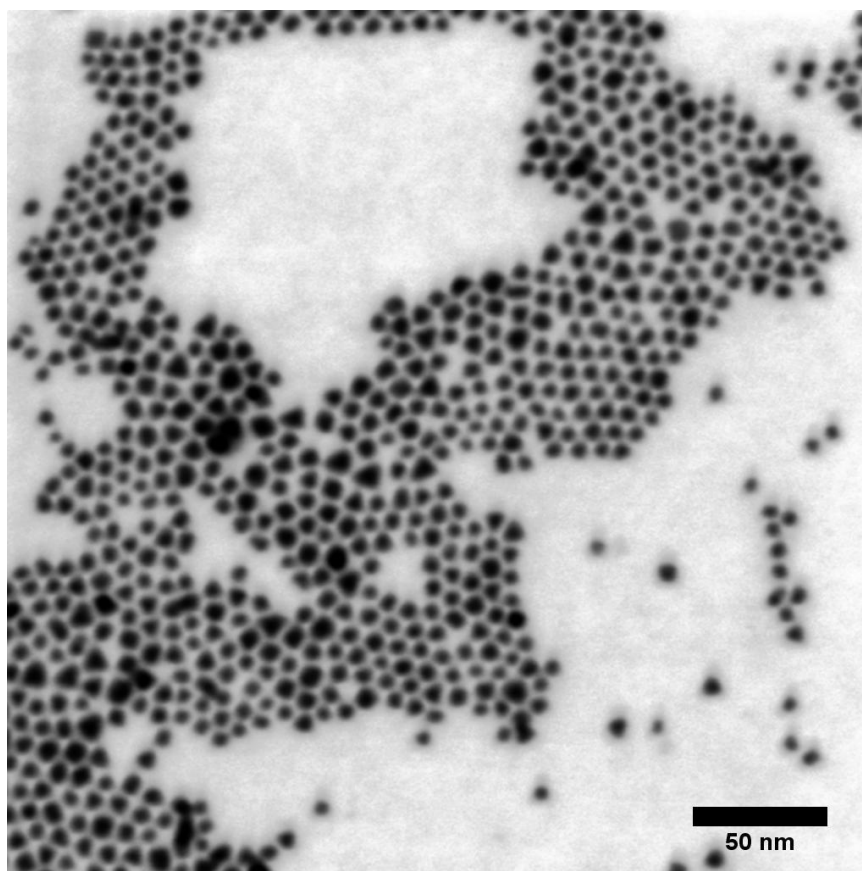
Atomic force microscopy imaging of the thin films of non-functionalized PF-NQD blends reveal rough films due to severe segregations (see Figure 7.3.5 (a)). Phase imaging, which is quite sensitive to nanometer scale material differences

due to measurement of the AFM tip's phase changes while tapping on the surface, supports the observation of phase separation. As can be seen from Figure 7.3.5 (b), bright regions and dark regions represent two different materials: NQDs and polymer segregated phases.

We also performed transmission electron microscopy (TEM) imaging to further understand the nanoscale interaction between the functional and non-functional polymer and NQDs. As shown in Figure 7.3.6, we performed bright field scanning mode TEM (STEM) imaging of the blends and hybrids. The same amount of NQDs have been mixed with the same weight of functional and non-functional PF. NQDs are more neatly dispersed in the functional PF as observed from Figure 7.3.6 (a). On the other hand, severely aggregated NQDs have been observed for non-functional polymer – NQD blends as can be seen from Figure 7.3.6 (b). In the TEM imaging, although the polymer itself cannot be easily imaged, NQDs are observed to be lying in nebulous host, which we attribute to the surrounding polymer (see Figure 7.3.6 (a)). For non-functional polymer, we do not observe any nebulous formation around NQDs, which also indicates that there is no specific interaction between NQDs and non-functional polymer (see Figure 7.3.6 (b)).



(a)



(b)

Figure 7.3.6 STEM images of NQDs in (a) functionalized PF and (b) non-functionalized PF. Possible explanation is attachment of the functional groups to the NQD surfaces, which helps to distribute NQDs homogenously.

In order to realize exciton injection pumping, efficient nonradiative energy transfer (NRET) will be required. NRET was first explained by Förster [113] who also laid down the requirements for NRET to take place. First, there should be a spectral overlap between the donor emission and the acceptor absorption. As can be seen from Figure 7.3.7, there is a strong spectral overlap between the emission of the functionalized PF and the absorption of CdSe/CdS/ZnS alloy-like core/shell NQDs. Here, we also note the difference between the emission and absorption spectra of functionalized PF in solution and in thin film (see Figure 7.3.7 (a) and (b), respectively). When made into thin films, the emission and absorption spectra of the polymer are broadened compared to the measured

spectra in solution. Also, emission is observed to be red-shifted. However, a similar shift in the absorption cannot be observed. Broadening of the absorption can be explained due to increased inhomogeneous broadening when the polymer is densely stacked into aggregates in thin films. On the other hand, the red shift in the emission spectrum of the polymer with an emerging emission tail can be attributed to the emitting defect states, which are more easily populated in thin film conditions due to increased inter-chain exciton diffusion rates. Some of the excitons in the thin films can be possibly trapped in the defects such as fluorenones and morphological flaws due to their small band gap property, which is favored within the disordered density of state (DOS) of the polymer. [114, 115] Defects lead to undesired emission in the spectrum of the polymer and also reduces the efficiencies of the polymer, since defects are not efficient emitters.

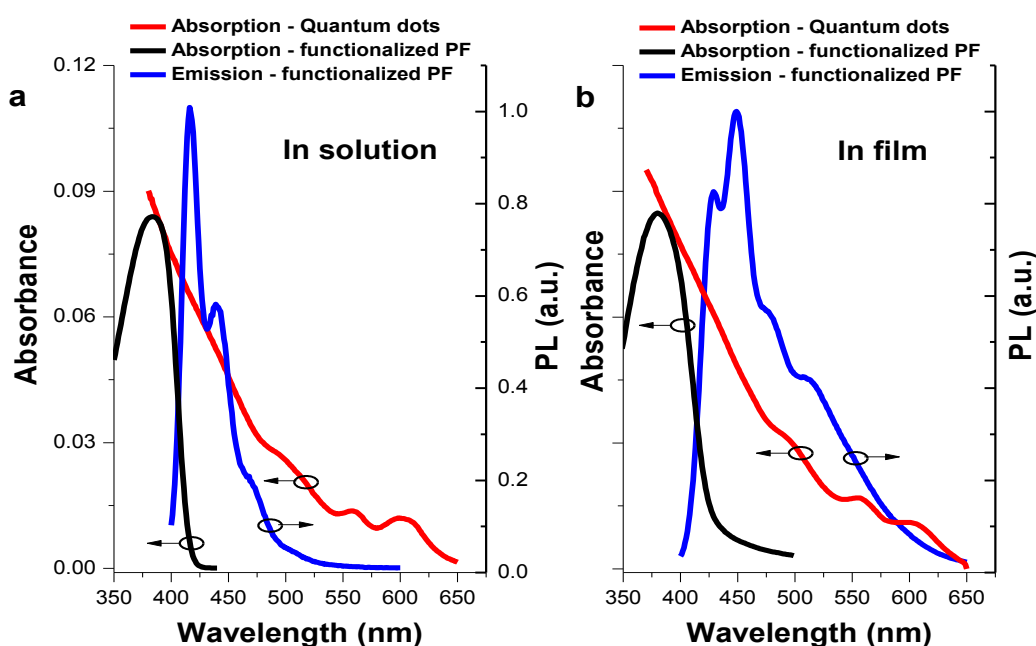


Figure 7.3.7 In-solution (a) and in-film (b) absorption - emission spectra of functionalized PF shown along with the absorption spectrum of NQDs.

Another requirement for NRET is the presence of a reasonable donor-acceptor separation, which should be comparable to Förster radius in order to have a

decent energy transfer rate and efficiency. Calculation of the Förster radius is ambiguous in our case since exact extinction coefficient information for the core/shell alloy-like NQDs is not straightforward to obtain. Also in the literature, there is no much report for the calculation of the extinction coefficient of core/shell NQDs. Nevertheless, using the previous literature on polymer-NQD energy transfer, we notice that Förster radius is estimated to be around 4 - 7 nm for a system of red-emitting CdSe/ZnS NQDs and blue emitting PF derivative co-polymer. [105]

We study energy transfer dynamics through measuring the fluorescence decay kinetics using a closed cycle Helium cryostat integrated with a time resolved fluorescence spectrometer (Fluotime 200) utilizing a TCSPC system (Pico Harp 300). Two different concentrations of NQD loading have been chosen as 3 w% and 45 w% to represent low and high concentration regimes, respectively. 3 w% hybrid is chosen to be for low NQD loading case, because center-to-center NQD separation is approximated to more than 34 nm. On the other hand, 45 w% hybrid is chosen to be the high NQD loading case, since center-to-center distance between NQDs is approximated to be smaller than 18 nm when homogenous distribution of NQDs is assumed.

After mixing functionalized PF and core/shell NQDs for a while in solution phase, thin films of the two different concentrations of the hybrids were obtained via spin coating on pre-cleaned double side polished quartz substrates. Hybrid mixtures are prepared from a 20 mg/ml of functionalized PF and a 10 mg/ml of CdSe/CdS/ZnS NQD solution. The film thicknesses are measured to be around 60 nm using a profilometer.

The sample films are loaded onto the cryostat holder. We preferentially performed our measurements while temperature is being decreased, since polymer may expose to phase relaxations during the cooling down process, which might not revert during the course of heating back to room temperature.

Time resolved fluorescence lifetime measurements are performed using a picosecond pulsed laser with a output photon energy of 3.307 eV operated at 5 MHz repetition rate. The average power of the beam is around 0.5 mW/cm² and energy levels per pulse are on the order of tens of pJs. The spot size of the laser beam is fixed to be a few mm², which is not fully focused in order to keep pulse intensity low to prevent singlet-singlet annihilation in the polymer. The system uses a PMT as a single photon detector, which has an instrument response function (IRF) FWHM around 200ps. To obtain actual decay curves, we have to deconvolve the IRF from the measured decays. Steady state PL information was also constructed using our TCSPC system via integrating under area of the decays measured in time-resolved emission spectra mode (TRES). In order to account for correct wavelength dependent detection response of our PMT, which is not calibrated for steady state PL measurements, we utilized Fluorolog 3 fluorescence spectrometer to correct the emission spectrum of the sample measured at the room temperature. Other temperature measurements are corrected accordingly.

After measuring the fluorescence decays of the hybrids at the donor and acceptor wavelengths at different temperatures, we have extracted lifetimes using exponential fits for the deconvoluted data. A single exponential fit was successful for donor decays in the absence of acceptor. In order to extract the lifetimes of the donors when made into hybrids, Loring-Anderson-Fayer (LAF) model is employed. [116] LAF model extends decay kinetics described by Förster while considering energy migration in donor molecules through dipole-dipole coupling. LAF model is assumed to be working for a wide range of acceptor concentrations and donor-donor coupling strengths. Donor fluorescence decay in the presence of acceptor is modeled by (7.3.1).

$$I_D = I_0 e^{\left[-\frac{t}{\tau_D} - 2 \left(\frac{\gamma_{DD}}{\sqrt{2}} + \gamma_{DA} \right) \left(\frac{t}{\tau_D} \right)^{\frac{1}{2}} \right]} \quad (7.3.1)$$

$$\alpha = \frac{1}{\tau_D} (R_{0A})^6 \quad (7.3.2)$$

$$\beta = \frac{1}{\tau_D} (R_{0D})^6 \quad (7.3.3)$$

where α and β are the strength factors for donor-acceptor and donor-donor couplings, respectively. If one of the coupling is more dominant, then LAF model can be used within the limit that is dictated by the dominant couple. We have calculated strength factors (α , β) using absorption spectra of the functionalized PF polymer obtain while in solution. R_{0D} is found to be 2.3 nm. If we were to use in-film emission and absorption spectra of the polymer, R_{0D} would turn out to be similar or smaller than 2.3 nm due to red-shifted polymer emission in thin films. From the literature, R_{0A} is estimated to be around 4 - 7 nm. When we compare the strengths of α and β , we observe that $\alpha \gg \beta$ so that γ_{DD} can be then neglected. However, LAF model might be underestimating donor-donor Coulomb coupling since R_{0D} is calculated under the point dipole assumption, whereas emitting chromophoric units of the conjugated polymer cannot be properly modeled as point dipoles.[117] Eventually, due to dominance of the donor-acceptor coupling, decay kinetics are modeled at the Förster limit given by (7.3.4). In fact, by doing so, we simply neglect the exciton diffusion in the polymer due to self-NRET between polymers.

$$I_D = I_0 e^{\left[-\frac{t}{\tau_D} - 2\gamma_{DA} \left(\frac{t}{\tau_D}\right)^{\frac{1}{2}}\right]} \quad (7.3.4)$$

γ_{DA} is the reduced acceptor concentration defined as in (7.3.5).

$$\gamma_{DA} = \frac{C_A}{C_{0A}} = C_A \frac{2\pi^{\frac{3}{2}} N R_{0A}^3}{3000} \quad (7.3.5)$$

Efficiency of the energy transfer can be calculated using (7.3.6).

$$\eta = \sqrt{\pi} \gamma_{DA} e^{\gamma_{DA}^2} (1 - \text{erf}(\gamma_{DA}))$$

(7.3.6)

Deconvoluted decay curves of the donor are fitted using (7.3.4). Then, γ_{DA} (i.e., reduced acceptor concentration) and η (i.e., energy transfer efficiency) are extracted at different temperatures for 3 w% and 45 w%. The lifetimes of functionalized PF in the presence of NQD acceptors are determined from energy transfer efficiency formula of $\eta = 1 - \frac{\tau_{DA}}{\tau_D}$. Figure 7.3.8 (a) shows the lifetimes of functionalized PF donor alone, in 3 w% and in 45 w% hybrids with respect to temperature. Figure 7.3.8 (b) also shows the extracted energy transfer efficiencies for 3 w% and 45 w% from the LAF model.

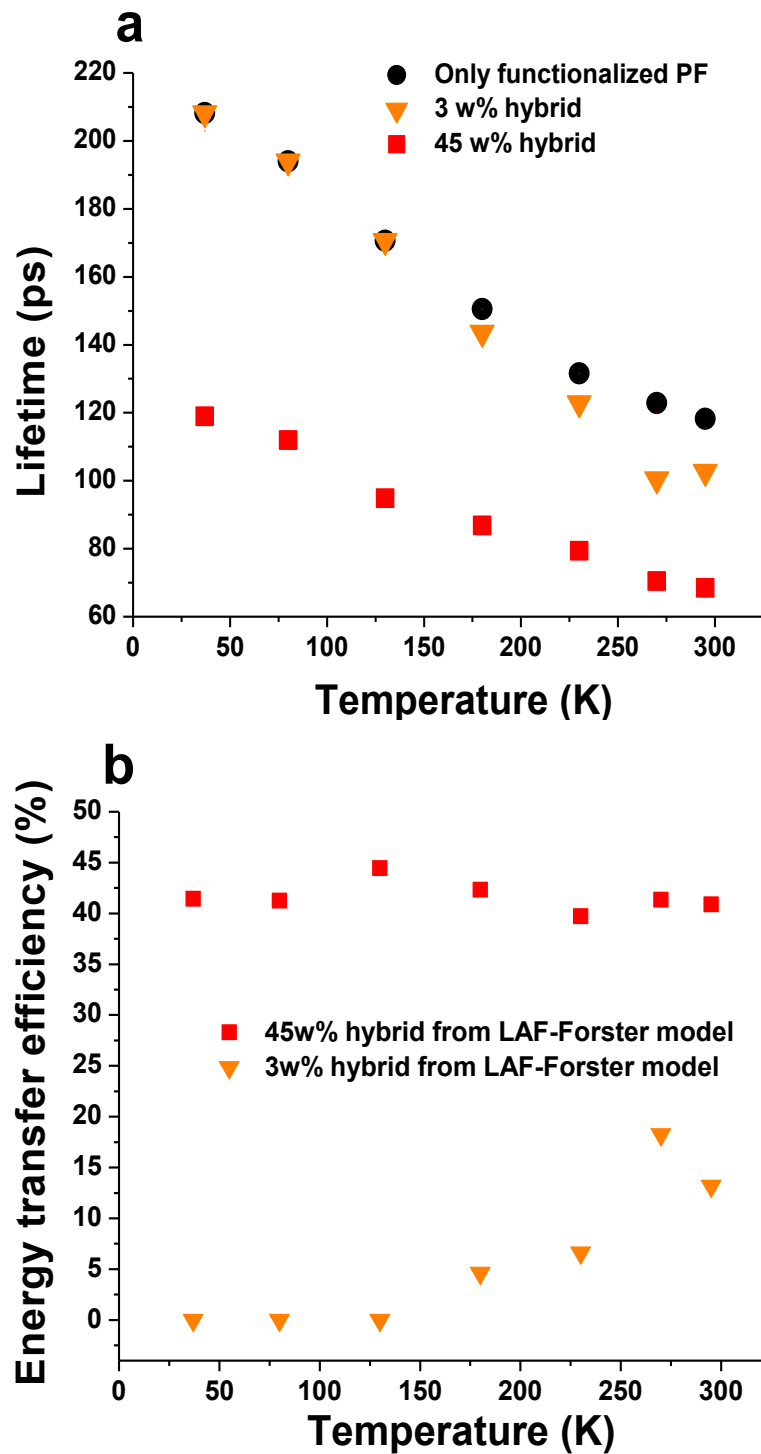


Figure 7.3.8 (a) Lifetimes of the functional PF in the presence and absence of the quantum dots for 3 w% and 45 w% hybrids with respect to temperature. (b) Energy transfer efficiencies extracted from LAF model with respect to temperature for 3 w% and 45 w% cases.

Fluorescence lifetime of the functionalized PF polymer in the absence of acceptor is observed to increase with reduced temperature. This is explained by the suppressed nonradiative relaxation channels for the depopulation of the excited state of the polymer at lower temperatures. Lifetimes of the functionalized PF while hybridized with NQDs also follow similar temperature dependent trends. In 3 w% hybrid, although donor lifetimes at higher temperatures are smaller than donor alone lifetimes, they become almost the same at lower temperatures (see Figure 7.3.8 (a)). However, donor lifetimes in 45 w% hybrid is always smaller than the case of donor alone, which indicates a strong lifetime modification due to increased NRET (see Figure 7.3.8 (a)).

As seen from Figure 7.3.8 (b), trends of energy transfer efficiencies differ significantly between 3 w% and 45 w% hybrid cases. In 3 w% loading (i.e., low loading regime), energy transfer efficiency is found to be decreasing with the reduced temperatures. Also, transfer efficiency shows a temperature activated behavior. However, in 45 w% hybrid, energy transfer efficiencies are found to be almost temperature independent.

We also plot energy transfer rates with respect to the temperature as shown in Figure 7.3.9. Energy transfer rates show a decreasing behavior as the temperature is decreased. Lutich *et al.* have also observed similar behavior for the transfer rates between polymer and NQD thin films prepared via layer-by-layer assembly. [106] Since excited state depopulation rate of the polymer (i.e., inverse of the donor lifetime) decreases at reduced temperatures, NRET rate, which is a competing process, also follows a similar trend. The reduction in the transfer rate with decreasing temperature is also expected from Förster's rate equation, where $k_{ET} = \frac{1}{\tau_D} \left(\frac{R_0}{r} \right)^6$ since τ_D increases significantly as the temperature is decreased. When we compare the transfer rates between low and high NQD loadings, 45 w% hybrid has, by far, larger rates than 3 w% hybrid, as

expected since average donor-acceptor distance in 45 w% is significantly smaller as compared to 3 w% hybrid case.

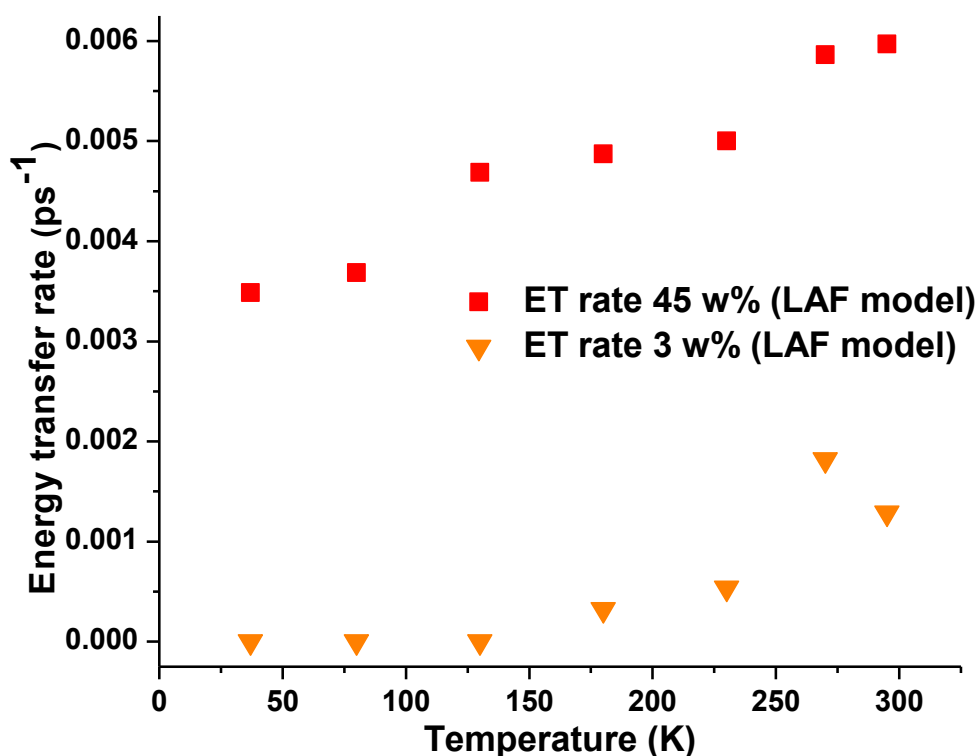


Figure 7.3.9 NRET rates for 3 w% and 45 w% hybrids with respect to temperature.

From the results that we obtained with LAF model, it has been observed that NQD acceptor loading can severely change the dynamics of the excitonic energy transfer with respect to temperature.

Diffusion of the excitons in the conjugated polymer plays an important role for energy transfer processes. For low acceptor loading regime, exciton diffusion is quite evident since average donor – acceptor separation is considerably large. On the other hand, effects of the exciton diffusion at high NQD loading case might be weaker since we observe an almost temperature independent energy transfer efficiencies.

To deepen the understanding of the underlying physics, we utilize another model proposed by Gösele et al. [118] Gösele model, which is first designed to predict energy transfer dynamics between chromophores having translational diffusion in a solution, is also applicable to molecular crystals since diffusion properties of the excitons in organic conductors can be modeled as translational motion of excitons. In Gösele model, there are two limits, which are determined by the material system itself. These two parameters, r_F the so-called effective trapping radius, and collision distance r_{AD} (i.e., the distance at which the excitons are immediately transferred) are compared to decide in which limit to operate.

If $r_F > r_{AD}$,

$$I_D(t) = I_0 e^{\left[-\frac{t}{\tau_D} - 4\pi D r_F n_A t - 2\gamma_{DA} \left(\frac{t}{\tau_D}\right)^{\frac{1}{2}} \right]} \quad (7.3.7)$$

If $r_{AD} > r_F$,

$$I_D(t) = I_0 e^{\left[-\frac{t}{\tau_D} - 4\pi D r_{AD} n_A t - 8 r_{AD}^2 n_A (\pi D t)^{\frac{1}{2}} \right]} \quad (7.3.8)$$

$$r_F = 0.676 \left(\frac{R_{0A}}{\tau_D D} \right)^{\frac{1}{4}} \quad (7.3.9)$$

where D is the diffusion coefficient, n_A is the number density of acceptors, τ_D is the donor lifetime alone, γ_{DA} is the reduced acceptor concentration which can be expressed in terms of n_A , and R_{0A} is the Förster radius between the donor and acceptor.

We assume r_{AD} to be the half of the Förster radius since more than 90% energy transfer efficiency can be considered as an immediate energy transfer. Using diffusion coefficient value of 1440 nm²/ns from the literature measured for a polymer of polyfluorene family [119] and using single exponential τ_D values for donor alone decays, it turns out that Gösele model for our specific material

system predicts r_F to be greater than r_{AD} . Energy transfer efficiency is shown in the integral form of decay curves as in (7.3.10), which leads to (7.3.11) for Gösele model for with the limit $r_F > r_{AD}$ given.

$$\eta = 1 - \frac{1}{\tau_D} \int \frac{I_D(t)}{I_D^0} dt \quad (7.3.10)$$

$$\eta = 1 - \frac{1}{1 + 4 D n_A \pi r_F \tau_D} + \frac{e^{\left[\frac{\gamma_{DA}^2}{1 + 4 D n_A \pi r_F \tau_D} \right]} \sqrt{\pi} \gamma_{DA} \operatorname{erfc} \left(\frac{\gamma_{DA}}{\sqrt{1 + 4 D n_A \pi r_F \tau_D}} \right)}{(1 + 4 D n_A \pi r_F \tau_D)^{\frac{3}{2}}} \quad (7.3.11)$$

Energy transfer efficiency obtained via Gösele model (using (7.3.11)) depends on independent parameters of R_{0A} , n_A , τ_D and D . R_{0A} is approximated between 4 – 7 nm and we assume it to be ~ 6 nm for the following discussions. Using the experimental data, we also know τ_D . Only unknown parameters are n_A and D .

We plot iso-efficiency (i.e., η) curves with respect to D (i.e., diffusion coefficient) vs. n_A (i.e., acceptor concentration) and L_D (i.e., diffusion length) vs. center-to-center NQD separation as shown in Figure 7.3.10 at three different temperatures of 295 K, 230 K and 180 K both for 3 w% (Figure 7.3.10 (a)) and 45 w% (Figure 7.3.10 (b)) hybrids.

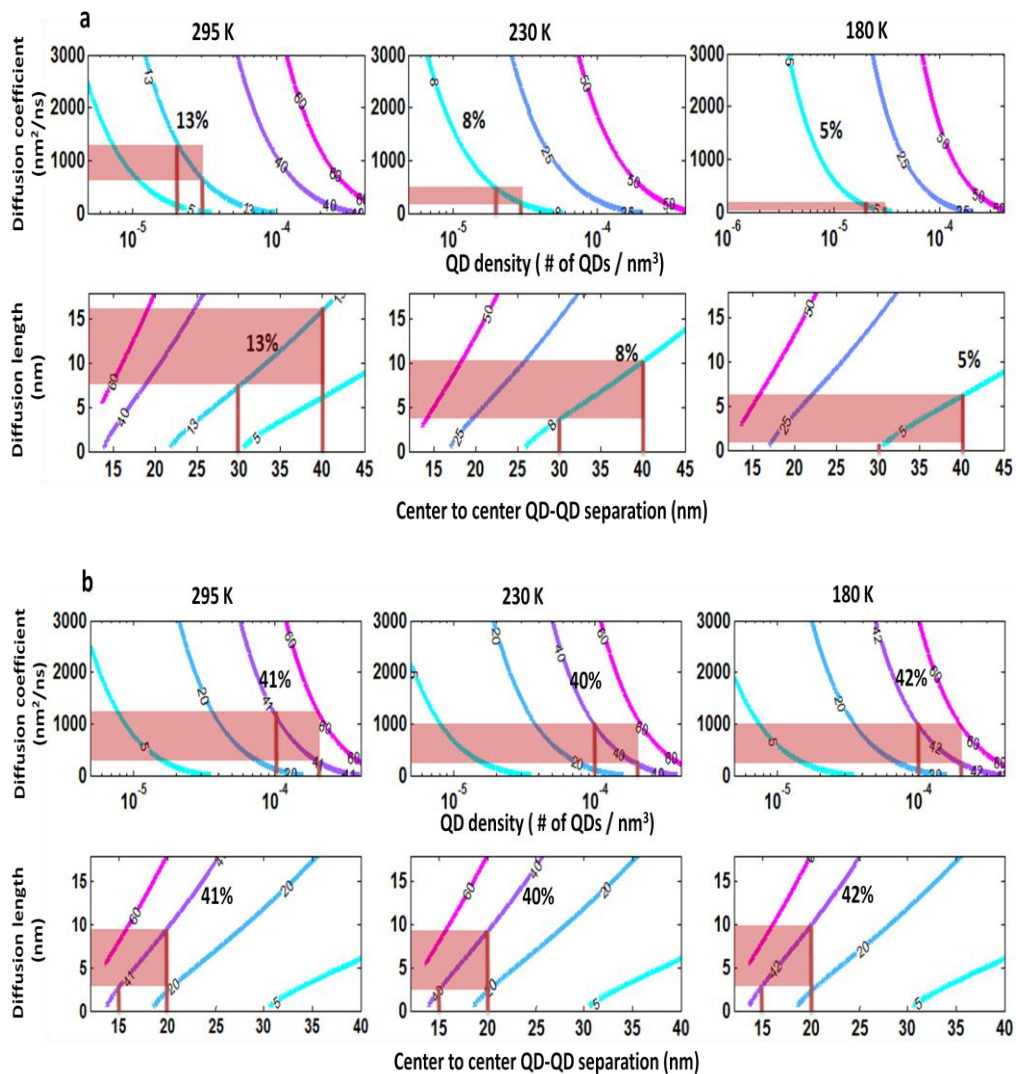


Figure 7.3.10 Iso-efficiency curves with respect to D vs. n_A and L_D vs. acceptor-acceptor separation for (a) 3 w% and (b) 45 w% hybrids. Semitransparent pink regions indicate the possible regions for D and L_D for predicted n_A and NQD separations in the respective thin film. For 3 w%, we estimate n_A to be around $2 - 3 \cdot 10^{-5}$ and center-to-center NQD separation between 30-40 nm. For 45 w%, we estimate n_A to be around $1 - 2 \cdot 10^{-4}$ and center-to-center NQD separation as 15-20 nm. The feasible range of diffusion coefficients and diffusion lengths are indicated on the plots by shaded areas for a given expected acceptor concentration and a center-to-center NQD separation.

As can be seen from Figure 7.3.10 (a) for 3 w% hybrid, possible range of diffusion coefficient decreases rapidly with decreasing temperature. Diffusion length is also shortened with lowered temperatures. This observation is in agreement with temperature activated diffusion properties of the PF family polymers due to requirement of an activation energy related to kT . At lowered temperatures due to reduced activation energy of the medium, up-hill jumps of excitons in the disordered DOS of the polymer becomes limited, which eventually limits the exciton diffusion. [120]

For 45 w% case (see Figure 7.3.10 (b)) 45 w% hybrid, we observe a slight decrease for the diffusion coefficient range with decreasing temperature as compared to 3 w% case. However, the diffusion length region is observed to be temperature independent. These observations for diffusion properties of the polymer agree with the observed energy transfer dynamics. At room temperature diffusion length is much larger in 3 w% as compared to 45 w%. However, diffusion length in 3 w% is cut down with decreasing temperature, which explains the decrease in the energy transfer efficiency trends for 3 w%. In 45 w% case, the diffusion length stays almost constant, which indicates that, although diffusion coefficient slightly decreases, increase in exciton lifetime at reduced temperatures balance each other out.

Also, L_D shows differentiation with NQD loading regime. At room temperature, L_D value range is larger in 3 w% than what it is for 45 w%, which means that excitons in 3 w% case can diffuse more at room temperature. For reduced temperatures, L_D value range decreases rapidly for 3 w% unlike 45 w% case, where L_D stays almost temperature independent.

In order to explain these observations, we take into account inter-chain and intra-chain diffusion properties of the conjugated polymers. As indicated by several previous reports, inter-chain diffusion is found to be faster than intra-chain diffusion for conjugated polymers. [117, 121] Comparing the exciton

diffusion properties of the polymers when they are highly isolated (e.g., in solution phase) and highly aggregated cases (e.g., when made into thin films), it has been observed that inter-chain diffusion becomes dominant in aggregated state of the polymer and it is much faster than intra-chain exciton diffusion, which is otherwise dominant in solution phase. [121] In our case, for 45 w% hybrid, shell-to-shell NQD separation is estimated to be smaller than 13 nm by assuming homogenous distribution of the NQDs so that polymer chains are more isolated as compared to 3 w% case where shell-to-shell NQD separation is more than 25 nm, leading to more aggregated state. At room temperature, the difference between D and L_D can be interpreted in the introduced context of inter and intra-chain diffusion. Since in 45 w%, polymers are more isolated, D is smaller in 45 w% than the observed D at 3 w%. L_D being smaller in 45 w% as compared to 3 w% is related to the reduced D values and the reduced exciton lifetime for 45 w% due to high NRET rates resulting from increased NQD loading yielding smaller average donor-acceptor separations.

As the temperature is reduced, severe reductions observed in D and L_D for 3 w% should also be explained in a similar context. Although polymers are more entangled at 3 w% case, leading to dominant inter-chain diffusion at room temperature. As the temperature is decreased, intra-chain diffusion should become dominant. Unlike inter-chain diffusion, which is assumed to be taking place due to dipole – dipole interaction between chains so that it is temperature independent, intra-chain diffusion is assumed to be propagate like hopping process of the excitons in the disordered DOS of the polymer due to conjugation length differences and defects in the chains. Traps in polymer chains start to confine more excitons as the temperature is lowered due to insufficient activation energy of the medium to save excitons from those traps. As a result, due to exciton trapping, inter-chain diffusion is lowered in 3 w% hybrid. Thinking of our material system in one dimensional schematic as shown in Figure 7.3.11 would be useful to understand the temperature dependent dynamics of D and L_D . Since fluorescence decay measurements are statistical in

nature because of utilization of pulsed lasers in TCSPC method, average distance of an exciton created in the polymer to a NQD where they are assumed to be homogeneously distributed in the polymer can be taken to be the half distance between two adjacent NQDs (see Figure 7.3.11). From this assumption, for 3 w% case, L_D should become smaller as the temperature is further decreased since we observe a decreasing energy transfer efficiency trend. Looking at Figure 7.3.11 again, assuming Förster radius as 6 nm, shell-to-shell NQD separation is more than 26 nm and an exciton will be created on the average in the polymer 13 nm away from an NQD. Excitons which are away from an NQD on the order of two times of the Förster radius will have negligible energy transfer efficiency.

For low temperatures, Gösele model tends to underestimate D and L_D since energy transfer efficiencies and modification in the decay becomes smaller where model becomes less sensitive. For example, if we think of a hypothetical case of a single NQD in a thick polymer film where we would like to model exciton diffusion in the polymer, we will get zero D and L_D values, since ensemble measurement of the polymer decay would not change with a single NQD incorporation at all. The model will underestimate the diffusion length of the excitons, which are at the end of the diffusion process still more than $2R_0$ away from NQDs since this diffusion process did not contribute to NRET. As can be seen from Figure 7.3.11, the diffusion length of R_x for 3 w% case will be insufficient. For 45 w%, since the distance of an average exciton created in the polymer to a NQD is shorter (see Figure 7.3.11) as compared to 3 w%, the prediction of D and L_D using Gösele model is more reliable. For 45 w% case, L_D value ranges being almost temperature independent supports the observed temperature independent energy transfer efficiency dynamics from the experiments. Again making use of the one dimensional schematic in Figure 7.3.11, the center-to-center distance between NQDs are approximated to be smaller than 18 nm, which implies that an exciton is created in the polymer 9 nm away from a NQD core on the average. From the model, L_D range is

approximated to be around 2 to 5 nm. For our assumed numbers for one dimensional schematic, about 3 nm of L_D will result in average exciton formation being 6 nm away from the center of an NQD, which will result in an NRET efficiency of around 50%, quite in agreement coherent with the experimental results of around 43%.

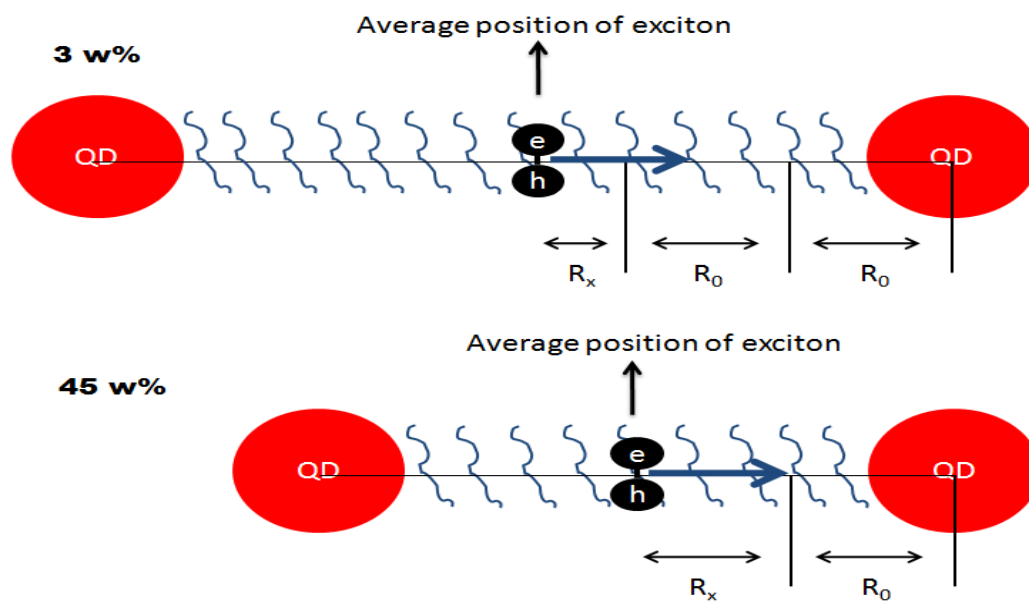


Figure 7.3.11 One dimensional schematic interpretation of the exciton diffusion in polymer in relation to NRET dynamics.

For 45w%, almost temperature independent L_D also verifies the temperature independence of the energy transfer. Although D is decreased, increase in the lifetime of the exciton due to reduced temperatures balances out the reduction in D to give almost constant L_D . As a physical interpretation, after the excitation of the polymer at high NQD loading, exciton diffusion may proceed dominantly with only downhill hops in the DOS in the close proximity polymer chains due to suppressed inter-chain diffusion. At almost all temperatures, exciton makes a similar journey only in downhill direction since there is always an intimate NQD around to zip the exciton through NRET.

Normalized steady state PL spectra of donor alone, 3 w% hybrid, and 45 w% hybrid are presented in Figure 7.3.12 for 295 K and 37 K. For polymer alone

case, we observe that, as the temperature is lowered, tail-defect emission is suppressed, which indicates the reduction in mobility of the excitons (as observed reduction in D) so that they are not trapped at the defects as much as it happens at room temperature. As can be seen from Figure 7.3.12, strength of the defect emission also changes with the loading amount. In 45 w% case, at room temperature, polymer exhibits a much lowered defect emission along with dominant shorter wavelength vibronic peak as compared to 3 w% case, where longer wavelength vibronic peak becomes dominant and defect emission is considerably higher. This observation of difference in the steady state PL for 3 w% and 45 w% cases also supports explanation for the physics behind the temperature dependent excitonic energy transfer between the polymers and NQDs: Gösele model predicts D values to be smaller in 45 w% case than 3 w% and we observe a suppressed defect emission in 45 w% compared to 3 w%, which should be directly related to suppressed exciton mobility at high NQD loadings due to change of the exciton diffusion dynamics from inter-chain to intra-chain. Also, since polymer chains are more isolated in 45 w%, its emission spectrum becomes similar to the PL spectrum measured for the same polymer in solution as shown before in Figure 7.3.7(a).

In terms of energy transfer dynamics, normalized PL data are not conclusive since absolute PL values cannot be acquired using our time resolved fluorescence spectrometer setup due to angle dependent count rate sensitivity of our PMT. However, we observe that emission of the NQDs becomes more dominant expectedly as NQD loading is increased.

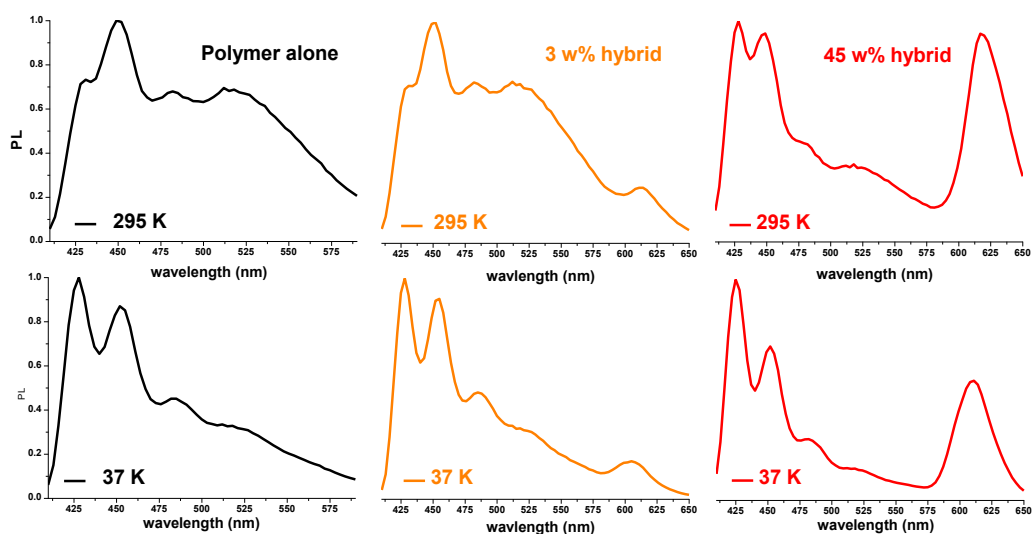
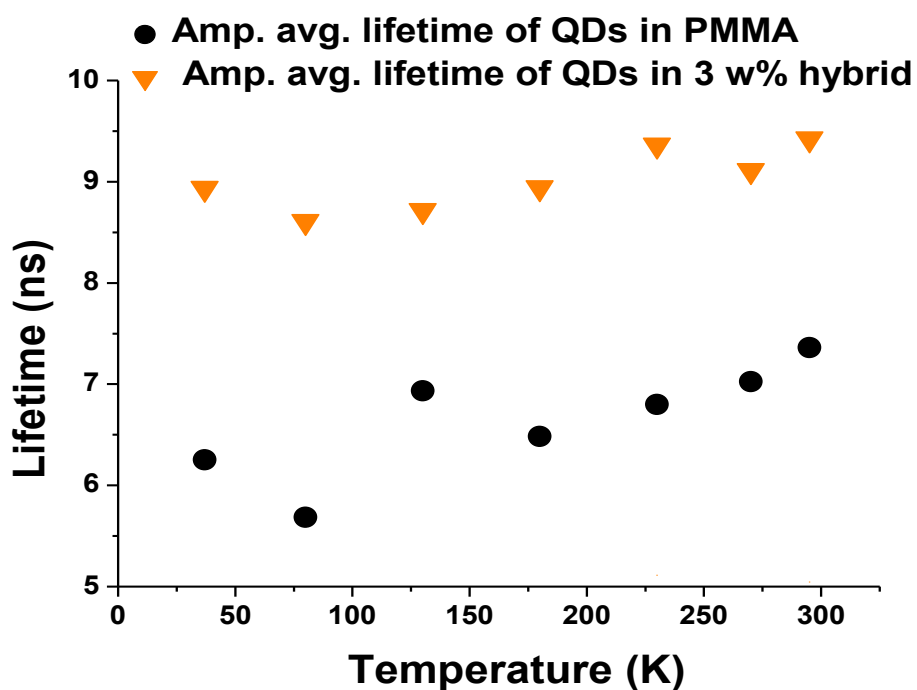


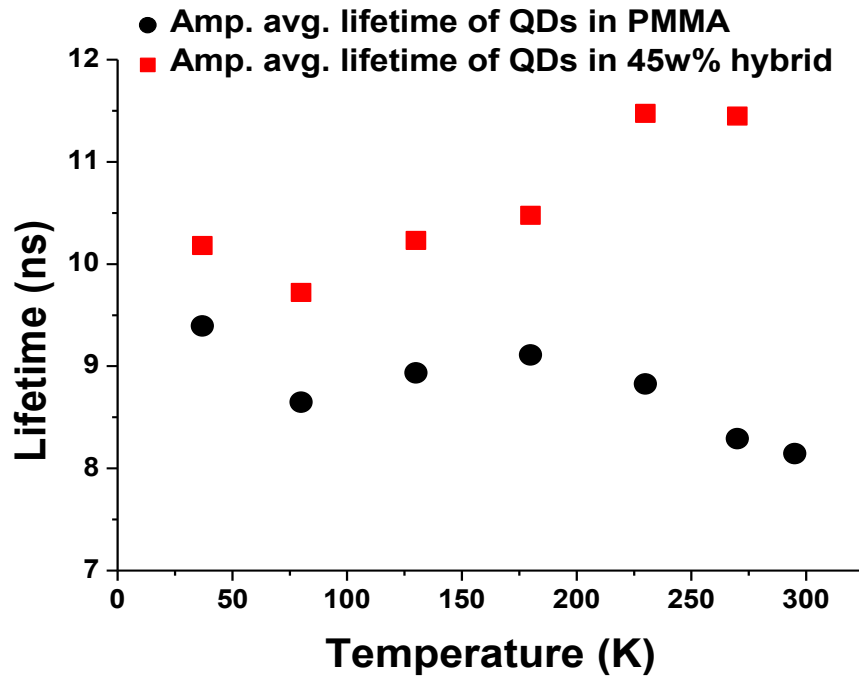
Figure 7.3.12 Steady state PL for only polymer and hybrid at different temperatures (PLs should be corrected with the correction factor).

To verify that excitons donated from the donor molecules can reach acceptors, we also check the acceptor decays. We observe that lifetime of the NQDs are elongated because of exciton injection from donor molecules. Acceptor lifetimes for 3 w% and 45 w% are measured at different wavelengths, since measurements have been performed at their own emission peaks, which differ with NQD loading and temperature. The decays are fitted with two exponentials and amplitude averaged lifetimes are shown in Figure 7.3.13. Acceptor lifetimes are increased as a function of temperature for both 3 w% and 45 w% cases as compared to only NQD lifetimes. For 3 w% hybrid, although we observe energy transfer rates approaching zero at lower temperature in the donor point of view, the acceptor lifetimes are enhanced for all temperatures. This discrepancy is due to the large difference in the number of donor and acceptor emitters. Since there are a few number of acceptors, but a much more number of donors around, energy transfer can be negligible for donor molecules when averaged to whole number of donors. For 45 w% case, although acceptor lifetimes are always enhanced for all temperatures indicating that energy transfer is always valid in terms of acceptors, the average lifetimes of the NQDs are in

this case observed to be approaching only acceptor lifetimes at lower temperatures. From the donor point of view, we have observed to have almost constant energy transfer efficiency. However, this might be due to difference in the rates of energy transfer. Since donor decay lifetime is much faster than lifetime of the acceptor NQDs, reduced rate of energy transfer at lower temperatures may lead to weakening of the enhancement in the acceptor lifetimes.



(a)



(b)

Figure 7.3.13 Amplitude averaged acceptor lifetimes for (a) 3 w% and (b) 45 w% at each temperature and sample measured for its peak emission wavelength.

Figure 7.3.14 shows the exemplary donor lifetime decays for the case of donor alone, and 3 w% and 45 w% hybrids at room temperature. As can be seen, IRF is quite close to decay curves since our system has a time resolution down to tens of ps. However, we need to make deconvolution fitting in order to achieve the actual decay curves.

Figure 7.3.14

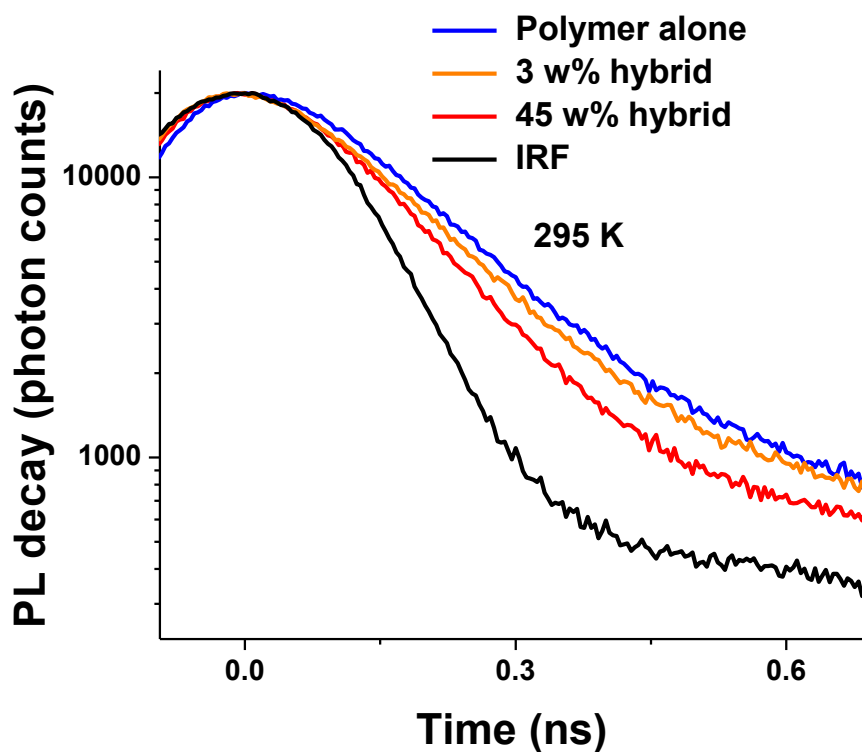


Figure 7.3.14 Exemplary lifetime decays for the cases of donor alone, and 3 w% and 45 w% hybrids shown together with IRF at room temperature.

7.4 Excitonically driven QD-LEDs

In section 7.2, we have described the principles of operation of the proposed excitonically driven QD-LEDs. The striking feature of the proposed device is exciton injection pumping of NQDs, instead of inconvenient charge injection since charge injection pumping is limited with the potential barriers around NQDs and their resulting poor electrical interface problems. On the other hand, conjugated polymers have superior electrical properties as compared to NQDs, which can be benefited in exciton pumped devices as to form and transfer excitons effectively. [122] Polymer and small organic molecule based organic light emitting diodes (OLEDs) can reach external quantum efficiencies around 5% for only fluorescent polymers and more than 20% when phosphorescent

small organic molecules are employed. [123] To achieve high efficiencies, charge injection, electron-hole injection balance and exciton formation should be engineered. Novel luminescent properties of NQDs and better electrical conductive properties of the conductive polymers are combined in exciton injection LEDs so that NQDs, which they can otherwise hardly be excited by charge injection, could be more effectively excited through nonradiative energy transfer.

The fabrication of the proposed devices consist of eight steps. Our fabrication is rather simple as expected from solution processability of the polymers and NQDs. Only final cathode formation is performed using vacuum deposition technique. Steps are summarized as follows:

- 1) Part of the ITO substrate is etched using an acidic mixture. This is done to prevent short circuit problems since cathode is placed just over active layer coated anode in a planar architecture (see Figure 7.4.1).
- 2) ITO substrates are cleaned very carefully using multiple solvent cleaning method.
- 3) PEDOT:PSS is used as the hole injection layer, which is spin coated over ITO.
- 4) Some part of the PEDOT:PSS is removed off to let direct contact with anode for further device testing. PEDOT:PSS is annealed to remove the solvent.
- 5) As-prepared hybrid active layer of NQDs and polymer is spin coated over PEDOT:PSS layer.
- 6) Again, some part of the hybrid active layer is removed off and annealed.
- 7) Top aluminum contacts are evaporated using physical vapor deposition technique with a shadow mask used in front of the devices to define the active device area.
- 8) Devices are encapsulated in a nitrogen filled glove box using epoxy and cover glass.

These fabrication steps are schematically summarized in Figure 7.4.1.

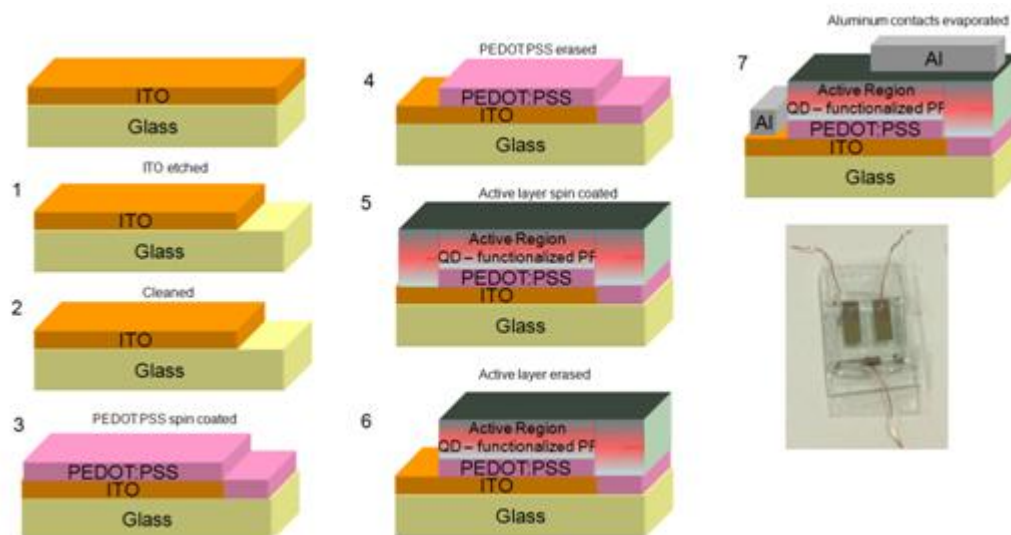


Figure 7.4.1 Schematic representation of the fabrication steps of the QD-LEDs following the fabrication steps 1-8. Photograph of a fabricated and encapsulated device is also shown.

For exciton injection QD-LEDs, selection of proper material systems is of utmost importance. As explained in the previous chapter more detailed, the use of conjugated polymers having no specific interaction with NQDs could possibly produce phase segregated thin films. Poor exciton injection properties are observed for devices having phase segregation due to inability of the donor polymers to effectively donate the excitons to NQD aggregates. We have utilized non-functionalized PF derivative co-polymer (see section 7.3) with core/shell CdSe/ZnS NQDs where there is no specific chemical or physical interaction between them. Besides, irreproducible results, the devices made on phase segregated films resulted in a wide spectrum of emission (see Figure 7.4.2) due to poor transfer capability of the excitons in the polymer. As can be seen in Figure 7.4.2, we observe that emission spectra of these devices consist of both emission of NQDs and polymers. The spectrum also changes with the applied bias voltage. This change depending on the bias is explained by the fact that exciton formation zone shifts with altering the bias since different number

of injected electrons and holes having different mobility will meet each other at different depths in the active layer. For example, taking higher hole mobility of the polymer into account and a better HOMO level match with the work function of the ITO and PEDOT:PSS (i.e., -5.1 eV for the cathode, and -5.6 for HOMO of the non-functionalized polymer), more holes will be injected than electrons. As a result, at lower bias voltages excitons will be created closer to anode. However, at increased bias voltages, exciton formation zone is expected to be broadened and shifted towards the anode since more electrons will be injected due to increased bias. This spatial shift in the exciton formation zone causes changes in the emission spectrum of the LED since there will be different interactions between the polymer and randomly segregated NQDs. For devices utilizing non-functionalized based polymer – NQD blends, we could not observe the severe suppression of the polymer emission although we increase the NQD concentration considerably, as expected, due to very low or no NRET.

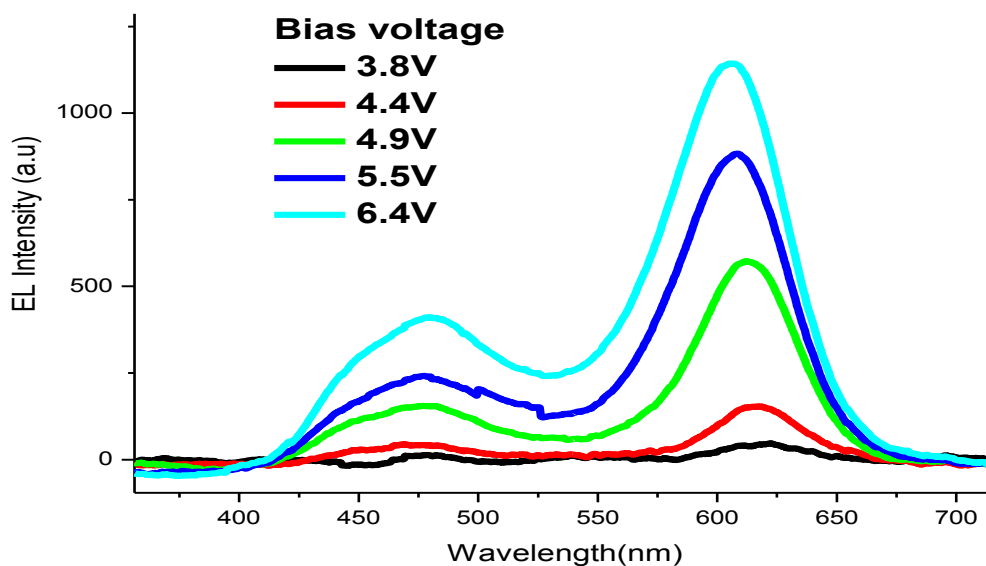


Figure 7.4.2 Exemplary electroluminescence of a QD-LED made up of non-functionalized PF and core/shell NQDs.

As we have stated, exciton injection pumping requires more care in terms of material selection. As a result, we have performed LED fabrication with the proposed specifically hybridized organic – inorganic hybrid material system.

First, we utilized functionalized PF co-polymer and core/shell CdSe/ZnS NQDs. Figure 7.4.3 shows the electroluminescence (EL) spectra of four different LEDs: one of them is only polymer LED, and the others are the QD-LEDs of red-emitting CdSe/ZnS NQDs with different loading amounts. The polymer-LED using only functionalized PF as the active layer has a quite broad emission. This is due to the defect emission in the polymer, which is caused from thin film formation of the polymer and device fabrication processes (i.e., heating under oxygen containing ambient environment). However, QD-LEDs show quite promising EL spectra. As the NQD loading is increased, the entire device emission is dominated by the emission of the NQDs. This shows us that our exciton injection scheme is working. As we increase the acceptor molecule amount in the films, donor excitons are more quenched through NRET means; in other words they are transferred to NQDs. EL emission peak of the red NQD is almost the same as its PL emission peak, with no strong shift at all.

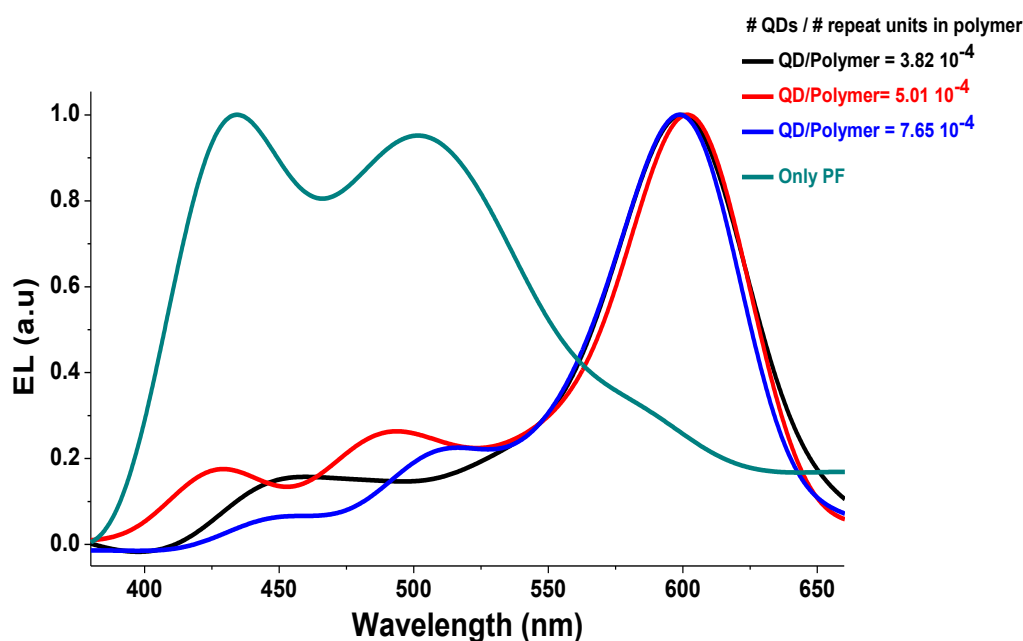


Figure 7.4.3 EL spectrum of excitonically driven QD-LEDs prepared with increasing concentration of NQDs and only polymer-LED at the same voltage level with normalized EL spectra.

As shown in Figure 7.4.4, we have also measured the current-voltage (I-V) characteristics of the fabricated devices (only shown for low and high concentration NQD cases). Although turn-on voltages are in the same range of ~ 5 V, increasing NQD loading amount slightly increases the turn-on voltage of the LED. This can be understood in terms of poor electrical properties of the NQDs. Although NQDs do not directly contribute to charge injection or transport due to presence of the conductive polymer, they can block and suppress charge mobility of the polymer since NQDs are doped into the matrix of polymer. If we were to think of the extreme case of very high NQD loadings, then polymers will be fully isolated from each other so that injected charges will not have a chance to find a current pathway to form excitons.

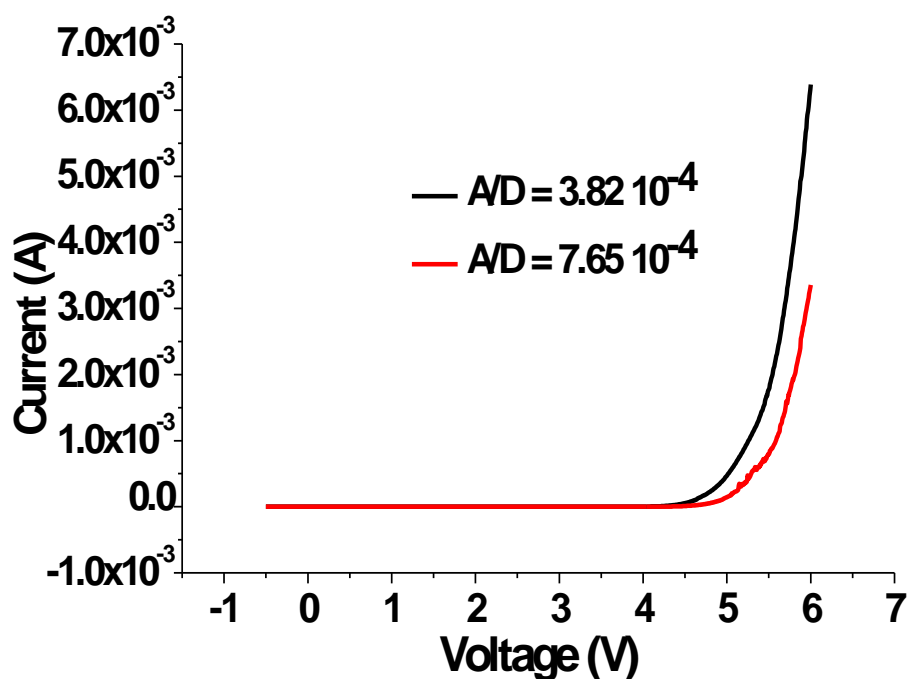


Figure 7.4.4 Typical I-V curve for the excitonically driven QD-LEDs fabricated with functionalized PF and red-emitting CdSe/ZnS NQDs.

We also take luminescence – current (LI) measurements of the same hybrid QD-LEDs. For the device fabricated with moderate NQD loading, it is observed that increasing the current drive through the LED results in almost a linear optical

power output current levels up to 100 mA/cm² (the device active area of 0.1 cm²) (see Figure 7.4.5).

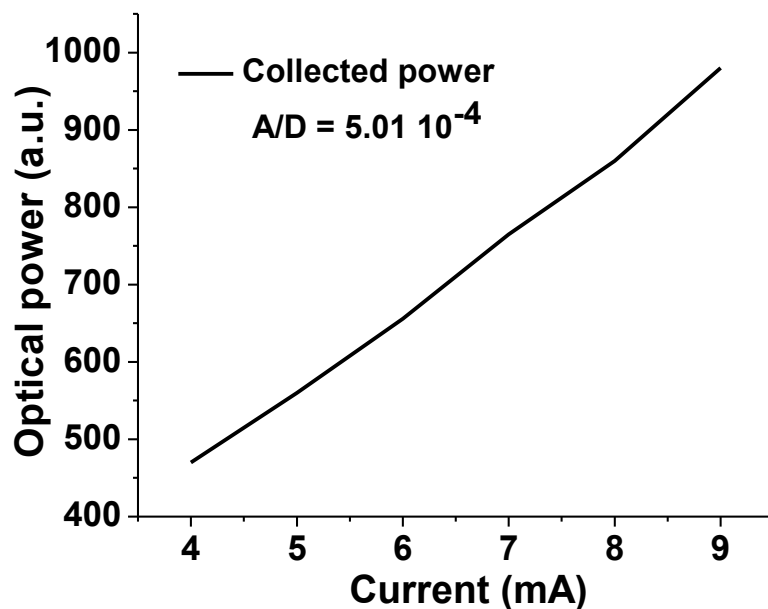


Figure 7.4.5 Luminance – current (LI) measurement of the fabricated excitonically driven QD-LED consisting of functionalized PF and red-emitting CdSe/ZnS NQDs.

Also, using core/shell CdSe/ZnS NQDs emitting at different wavelengths spanning green, yellow and red colors, we obtained excitonically driven QD-LEDs with EL emission spectra exhibiting almost pure NQD emission (see Figure 7.4.6 shown along with photographs of the devices while they are actively working). Although functionalized PF emission is almost totally suppressed with utilization of yellow- and red-emitting NQDs, we encounter with some weak emission coming from the PF when green-emitting CdSe/ZnS NQDs are used. All three devices have been intended to be prepared with the same amount of NQD loadings, which in fact explains the observed phenomenon. Between the functionalized PF and NQDs, spectral overlap of the donor emission and acceptor absorption is the highest for red-emitting NQD, and the lowest for green-emitting NQDs. This implies us that NRET is expected to be stronger for polymer – NQD couple when NQDs emit at longer wavelengths (i.e., red-emitting). Therefore, excitonic pumping of the green-

NQDs are less effective as compared to yellow- and red-emitting NQDs. To overcome this problem and obtain almost pure green-emitting QD-LED, we need to increase the loading amount.

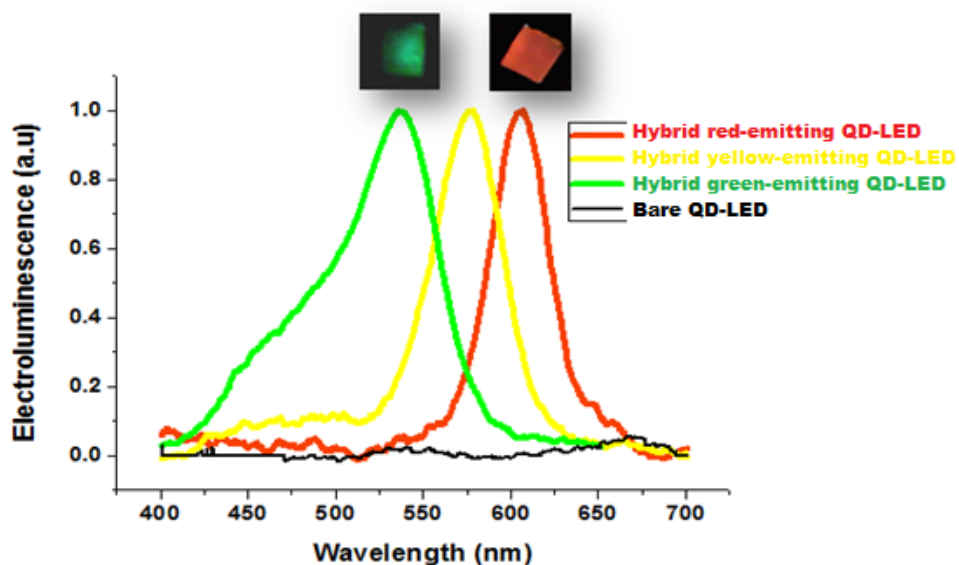


Figure 7.4.6 EL spectrum of excitonically injection pumped QD-LEDs utilizing different color emitting NQDs.

Next, we have performed efficient green-emitting excitonically driven QD-LEDs utilizing alloy-like CdSe/CdS/ZnS NQDs that we have synthesized in our labs. These NQDs are quite efficient in solution where PL quantum yields reach 80%. Designing the active layer with higher NQD loading resulted in QD-LED with a EL of almost pure green as shown in Figure 7.4.7.

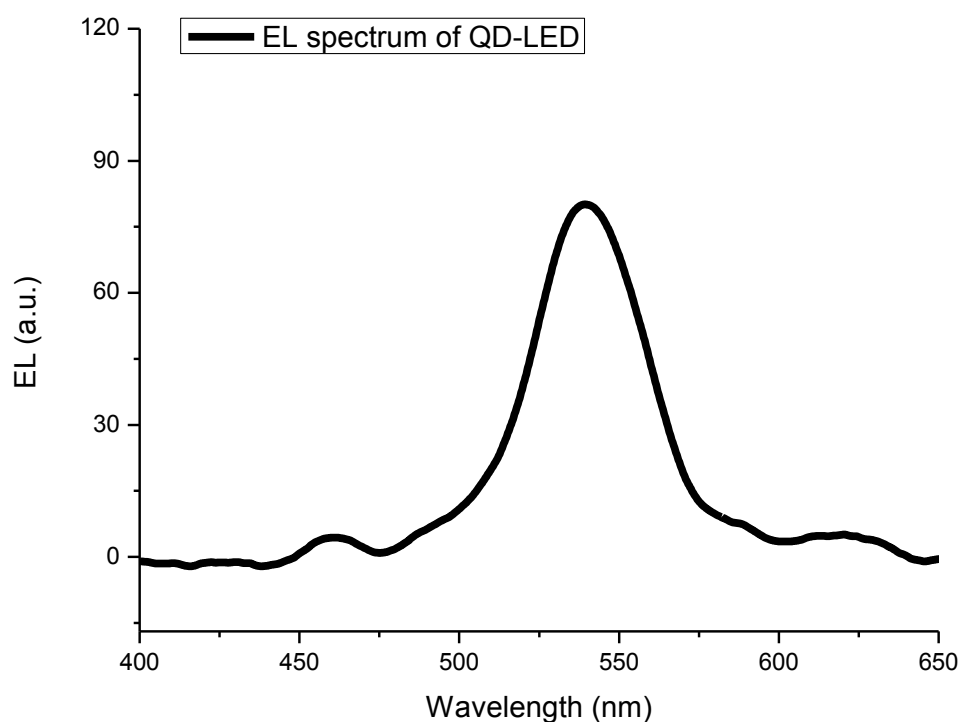


Figure 7.4.7 EL spectrum of excitonically driven QD-LED with functionalized PF and green emitting CdSe/CdS/ZnS NQDs designed for obtaining pure green emission.

In terms of external quantum efficiencies of the devices, we can routinely obtain efficiencies on the order of $\sim 0.01\%$, which can be considered to be quite poor. The low efficiencies of these devices stem from a few factors: First, fabrication of the devices is performed in ambient conditions causing oxidation of the charge injecting interfaces between the polymer and anode/cathode. Although we encapsulate our devices after the fabrication processes immediately, the resulting efficiencies suffer a lot. Encapsulation only helps to preserve the efficiency level just before the devices are brought to be encapsulated. For example, if devices are left to ambient conditions for an hour without encapsulation, even we make encapsulation at the end of the hour, device efficiencies excessively decrease. Normally, the fabrications steps should be performed in oxygen free environments, which is quite conventional for organic electronics. Second, we use the most simple device architecture consisting of only hole injection and luminescent active layer. This causes poor injection for

the polymer, too. To understand this better, we have performed cyclic voltammetry measurements (see Figure 7.4.8) at the group of Prof. Levent Toppare at Chemistry Department of METU. We measure that our functionalized PF polymer has a quite low HOMO level (ionization potential) around -6.2 eV and a LUMO level (electron affinity) around -3.0 eV. Utilization of only PEDOT:PSS hole injection layer which has a HOMO level around -5.1 eV, results in quite poor injection of the holes due to almost 1 eV difference in the HOMO levels. In terms of LUMO levels, there is more than 1 eV potential barrier between LUMO of our polymer and work function of aluminum (i.e., -4.2 eV).

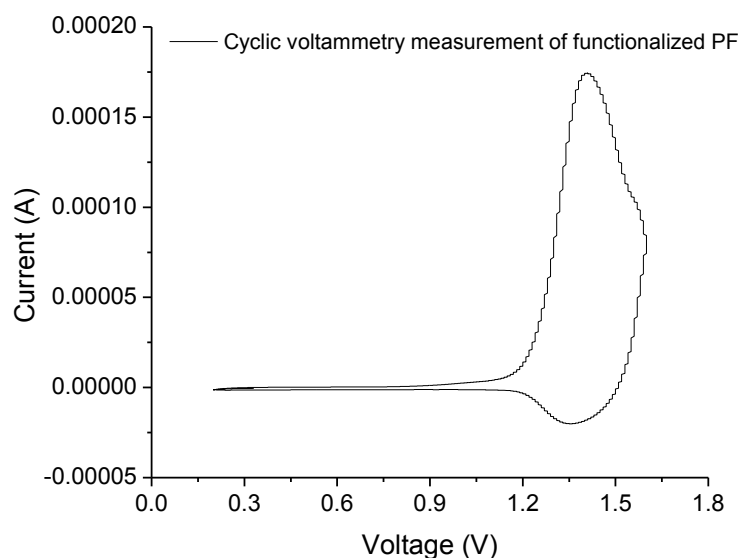


Figure 7.4.8 Cyclic voltammetry measurement of functionalized PF in order to determine its highest occupied molecular orbital level (HOMO).

However, by optimizing the loading amount of CdSe/CdS/ZnS alloy like core/shell NQDs in functionalized PF matrix, we were able to fabricate devices reaching a peak external quantum efficiency around 0.3 % as shown in Figure 7.4.9. The state of art QD-LEDs, working with charge injection principle, utilizing carefully chosen and injection layers can attain at most 1 - 2 % external quantum efficiencies. [124] In our case, there is a large room available for the improvement of the external quantum efficiencies. However, our experimental

results indicate that there is no fundamental limit that will prevent enhancing the efficiency levels of our exciton injection devices.

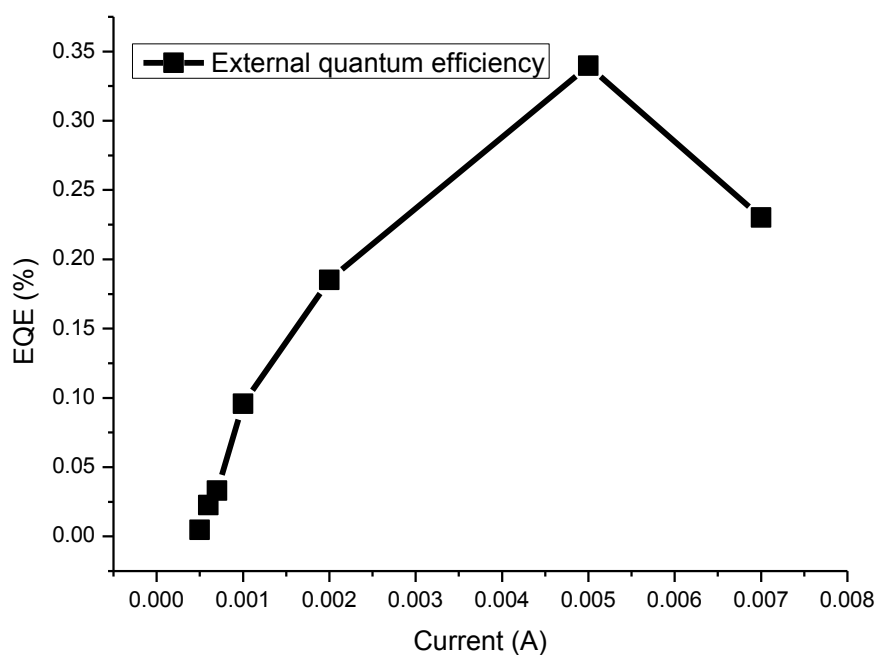


Figure 7.4.9 External quantum efficiency vs. injected current for an excitonically driven QD-LED.

7.5 Conclusions

In conclusion, we have proposed a new paradigm of exciton pumping for quantum dot based light emitting diodes. To achieve effective exciton pumping through nonradiative energy transfer process, we proposed and studied a new hybrid material system of NQDs with a functionalized polymer. Our hybrid material system consists of functionalized PF derivative co-polymer and core/shell CdSe/CdSe/ZnS or CdSe/ZnS NQDs. We have also studied the energy transfer dynamics in our hybrid material system using temperature dependent fluorescence lifetime measurements and analyses to deepen the current fundamental understanding behind the underlying physics of excitonic processes. We observed a strong relation of the temperature dependent energy

transfer dynamics with NQD loading amount. For the high loading case, almost temperature independent transfer efficiency dynamics have been attained. On the other hand, low loading case showed a decreasing transfer efficiencies with reduced temperatures. Interpretation of the results have been made via utilization of two different models (i.e., LAF and Gösele).

Change of exciton diffusion kinetics in the organic part due to effects of NQD loading is found to be main reason of the different transfer efficiency trends. High NQD loading regime makes polymer chains isolated from each other and reduces fast inter-chain diffusion process, but at low loading regime inter-chain diffusion is more dominant since polymer chains are more entangled. We also performed fabrication of the proposed exciton pumped QD-LEDs. Although fabrication related issues (i.e., air degradation of during fabrication) limits the ultimate efficiencies of the devices, we observe that exciton injection pumping method works and it is promising. Devices showing relatively low turn-on voltages with external quantum efficiencies up to 0.3% has been obtained. However, as a future work device designs should be optimized and engineered.

Chapter 8

Conclusions

Today production and utilization of energy has become a significant problem. The scientific community is striving to develop better means of energy production and utilization. To this end, in this thesis, we exploit novel properties of semiconductor nanocrystal quantum dots for photovoltaics and light emitting diodes. Radiative and nonradiative energy transfer capabilities of the nanocrystal quantum dots enabled us to propose and develop new hybrid devices in the pursuit of the device performance improvement.

We have proposed and shown nanocrystal quantum dot integrated nanopillar silicon solar cells, which benefit efficient photon down-conversion owing to superior optical properties achieved by nanostructured architecture of the devices. When nanopillar solar cell is grafted with nanocrystals, a strong enhancement in the spectral performance up to 6-folds could be obtained. Nanopillar architecture produce enhancements in spectral utilization of the sunlight up to 4 times larger than that obtained with planar architecture. The power conversion efficiency of the nanopillar solar cell is increased by 13% as a result of better spectral performance after designing and optimizing the converter layer.

We have also utilized a nanopillar architecture for color conversion light emitting diodes consisting of InGaN/GaN multi-quantum wells hybridized with nanocrystal quantum dots as converter layers. Thanks to increased interaction volume between multi-quantum-wells and nanocrystal quantum dots, to the best of our knowledge, the highest nonradiative energy transfer efficiency of 83%

was obtained. We have shown that nonradiative energy transfer can also be tuned via utilization of different sized quantum dots by modeling the energy transfer kinetics, which agreed well with the experimental results. This work is important for color conversion light emitting diode applications, which employ nanocrystal quantum dots as novel-phosphors for color converter layers.

Finally, we have proposed and demonstrated that charge injection problems of nanocrystal based light emitting diodes can be addressed by direct exciton injection scheme via nonradiative energy transfer means. We have studied the excitonic interactions between a promising hybrid system consisting of conductive polymer and nanocrystal quantum dots. We have studied temperature dependent energy transfer dynamics of the hybrids with different quantum dot loadings. Temperature dependent trends of energy transfer efficiency have been investigated using physical modeling. The underlying physics behind the change of the exciton diffusion properties of the conductive polymer is discussed. We also have shown the proof-of-concept excitonically driven nanocrystal based light emitting diodes with a very simple device design.

We believe that semiconductor quantum dot nanocrystals will come into prominence for various application ranging from optoelectronics to biology. Already several companies offer commercially available nanocrystal quantum dots in solutions such as Invitrogen/LifeTechnologies, Ocean NanoTech, eBioscience, Nanoco Group PLC and Sigma Aldrich. One of the significant applications will emerge shortly in light emitting diode technology including display technology. Several companies are already working on quantum dot based LEDs and displays such as QD Vision, Samsung, Lemnis Lighting, and Nanoco Group PLC. Our results indicate that such proposals and developments of the hybrid systems exploiting nanocrystal quantum dots to enhance device properties hold great promise.

6.1 Contributions

This thesis resulted in two SCI (science citation index) publications and one publication is in submission process. Also, I presented two talks in a refereed international conference about the research work undertaken in this thesis.

[1] **B. Guzelturk**, E. Mutlugun, X. Wang, K.L. Pey, and H.V. Demir, “Photovoltaic nanopillar radial junction diode architecture enhanced by integrating semiconductor quantum dot nanocrystals as light harvesters,” *Appl. Phys. Lett.*, vol. 97, pp. 093111 (2010).

[2] S. Nizamoglu, **B. Guzelturk**, D. - W. Jeon, I. - H. Lee, and H. V. Demir, “Efficient nonradiative energy transfer from InGaN / GaN nanopillars to CdSe / ZnS core/shell nanocrystals,” *App. Phys. Lett.*, vol. 98, pp.163108 (2011).

[3] **B. Guzelturk**, P. L. Hernandez-Martinez, D. Tuncel, and H. V. Demir, “Specifically anchored polymer - quantum dot hybrids: Temperature dependent nonradiative energy transfer dynamics for excitonically pumped quantum dot based light emitting diodes,” (in submission) (2011).

[4] **B. Guzelturk**, E. Mutlugun, X. Wang, K.L. Pey, and H.V. Demir, “Light-harvesting semiconductor quantum dot nanocrystals integrated on photovoltaic radial junction nanopillars,” *IEEE Photonics Society*, 2010 23rd Annual Meeting, Denver, CO pp. 357-358 (2010).

[5] **B. Guzelturk**, T. Erdem, E. Unal, S. Nizamoglu, D. Tuncel, H.V. Demir, “Non-Radiative Energy-Transfer-Driven Quantum Dot LEDs,” *IEEE Photonics Society*, 2010 23rd Annual Meeting, Denver, CO, pp. 146-147 (2010).

BIBLIOGRAPHY

[1] Annual energy outlook 2010, U.S. Energy Information Administration, Washington, DC <http://www.eia.gov/oiaf/aeo/pdf/appendixes.pdf> (accessed on 12.07.11).

[2] The promise of solid state lighting for general illumination light emitting diodes (LEDs) and organic light emitting diodes (OLEDs), Optoelectronics Industry Development Association, Washington, DC, http://www.netl.doe.gov/ssl/PDFs/oida_led-oled_rpt.pdf (accessed on 12.07.11).

[3] R. V. Steele, "The story of a new light source," *Nature Photonics*, vol. 1, pp. 25-26 (2007).

[4] Light Emitting Diode (LED): A Global Market Report, Global Industry Analysts, Inc. (GIA) (2011).

[5] E. F. Schubert, *Light Emitting Diodes*. Cambridge University Press, New York (2006).

[6] A. P. Allivisatos, "Semiconductor clusters, nanocrystals, and quantum dots," *Science*, 271, 933 – 937 (1996).

[7] M. Achermann, M. A. Petruska, S. Kos, D. L. Smith, D. D. Koleske and V. I. Klimov, Energy-transfer pumping of semiconductor nanocrystals using an epitaxial quantum well, *Nature*, vol. 429, pp. 642-646 (2004).

-
- [8] V.L. Colvin, M.C. Schlamp, A.P. Alivisatos, "Light-emitting diodes made from cadmium selenide nanocrystals and a semiconducting polymer," *Nature*, vol. 370, pp. 354–357 (1994).
- [9] S. Coe-Sullivan, W. Woo, M.G. Bawendi, V. Bulović, "Electroluminescence of Single Monolayers of Nanocrystals in Molecular Organic Devices," *Nature*, vol. 420, pp. 800- 803 (2002).
- [10] B. B. Rath, J. Marder, "Power from sunlight: photovoltaics," *Adv. Mater. and Proc.*, vol. 165, pp. 62-64 (2007).
- [11] Photovoltaics basics, Bundesministerium für Wirtschaft und Technologie (BMWi) Federal Ministry of Economics and Technology, Germany.
- [12] Türkiye'nin güneş enerjisi potansiyeli 380 milyar kWh, *Yatırımlar Dergisi*, 10 May 2008.
- [13] A. Müller, M. Ghosha, R. Sonnenschein, and P. Woditsch, "Silicon for photovoltaic applications," *Mater. Sci.Eng. B*, vol. 134, pp.257-262 (2006).
- [14] R. M. Swanson, "A vision for crystalline silicon photovoltaics," *Progress in Photovoltaics: Research and applications*, vol. 14, pp. 443-453 (2006).
- [15] M. Green, *Third generation photovoltaics: Advanced solar energy conversion*, Springer Verlag, Berlin (2004).
- [16] C. Honsberg, S. Bowden, "Quantum efficiency," PV CDROM, pveducation.org.

[17] N. S. Sariciftci, L. Smilowitz, A. J. Heeger, F. Wudl, "Photoinduced electron transfer from a conducting polymer to buckminsterfullerene," *Science*, vol. 258, pp. 1474-1476 (1992).

[18] J. H. Burroughes, D.D.C. Bradley, A.R. Brown, R.N. Marks, K. Mackay, R.H. Friend, P.L. Burns, A.B. Holmes, "Light emitting diodes based on conjugated polymers," *Nature*, vol. 347, pp. 539-541 (1990).

[19] F. Hide, M.A. Diaz-Garcia, B.J. Schwartz, M.R. Andersson, Q.B. Pei, A.J. Heeger, "Semiconducting polymers: a new class of solid-state laser materials," *Science*, vol. 273, pp. 1833-1836 (1996).

[20] A.R. Brown, A. Pomp, C.M. Hart, D.M. Deleeuw, "Logic gates made from polymer transistors and their use in ring oscillators," *Science*, vol. 270, pp. 972-974 (1995).

[21] J. R. Lakowicz, *Principles of fluorescence spectroscopy*, Springer, third edition New York, NY (2006).

[22] S.V. Gaponenko, *Optical properties of semiconductor nanocrystals*, Cambridge University Press, 1998.

[23] C.B. Murray, D.J. Norris, M.G. Bawendi, "Synthesis and characterization of nearly monodisperse CdE (E = S, Se, Te) semiconductor nanocrystallites," *J. Am. Chem. Soc.*, vol. 115, pp. 8706-8715 (1993).

[24] V.I. Klimov, *Nanocrystals quantum dots*, 2nd edition, CRC Press, 2010.

-
- [25] J. McBride, J. Treadway, L.C. Feldman, S.J. Pennycook, S.J. Rosenthal, "Structural basis for near unity quantum yield core/shell nanostructures," *Nano Lett.*, vol. 6, pp. 1496-1501 (2006).
- [26] M. Achermann, M. A. Petruska, S. Kos, D. L. Smith, D. D. Koleske, V. I. Klimov, "Energy-transfer pumping of semiconductor nanocrystals using an epitaxial quantum well," *Nature*, vol. 429, pp. 642-646 (2004).
- [27] S. Nizamoglu, T. Ozel, E. Sari, and H. V. Demir, "White light generation using CdSe/ZnS core-shell nanocrystals hybridized with InGaN/GaN light emitting diodes," *Nanotechnology*, vol. 18, pp. 065709 (2007).
- [28] S. Nizamoglu, B. Guzelturk, D. - W. Jeon, I. - H. Lee, H. V. Demir, "Efficient nonradiative energy transfer from InGaN / GaN nanopillars to CdSe / ZnS core/shell nanocrystals," *App. Phys. Lett.*, vol. 98, pp.163108 (2011).
- [29] V. L. Colvin, M. C. Schlamp, A. P. Alivisatos, "Light-emitting diodes made from cadmium selenide nanocrystals and a semiconducting polymer," *Nature*, vol. 370, pp. 354–357 (1994).
- [30] S. Coe-Sullivan, W. Woo, M.G. Bawendi, V. Bulović, "Electroluminescence of single monolayers of nanocrystals in molecular organic devices," *Nature*, vol. 420, pp. 800-803 (2002).
- [31] T.-H. Kim, K.-S. Cho, E. K. Lee, S. J. Lee, J. Chae, J. W. Kim, D. H. Kim, J.-Y. Kwon, G. Amaratunga, S. Y. Lee, B. L. Choi, Y. Kuk, J. M. Kim¹, K Kim, Full-colour quantum dot displays fabricated by transfer printing, *Nature Photonics*, vol. 5, pp. 176-182 (2011).

[32] W.U. Huynh, J.J. Dittmer, A.P. Alivisatos, “Hybrid nanorod-polymer solar cells,” *Science*, vol. 295, pp. 2425-2427 (2002).

[33] I. Gur, N.A. Fromer, M.L. Geier, A.P. Alivisatos, “Air-stable all-inorganic nanocrystal solar cells processed from solution,” *Science*, vol. 310, pp. 462-465 (2005).

[34] E.H. Sargent, “Infrared photovoltaics made by solution processing,” *Nature Photonics*, vol. 3, pp. 325-331 (2009).

[35] B. Guzelturk, E. Mutlugun, X. Wang, K.L. Pey, H.V. Demir, “Photovoltaic nanopillar radial junction diode architecture enhanced by integrating semiconductor quantum dot nanocrystals as light harvesters,” *Appl. Phys. Lett.*, vol. 97, pp. 093111 (2010).

[36] G. Konstantatos, E.H. Sargent, “Nanostructured materials for photon detection,” *Nature Nanotechnology*, vol. 5, pp. 391-400 (2010).

[37] F. Perrin, “Fluorescence et induction moléculaire par résonance,” *C. R. Hebd. Seances Acad. Sci.*, vol. 184, pp.1097-1100 (1927).

[38] T. Förster, “Zwischenmolekulare energiewanderung und fluoreszenz,” *Annalen der Physik*, vol. 437, pp. 55-75 (1948).

[39] R.M. Clegg, “Förster resonance energy transfer – FRET what is it, why do it, and how it is done,” *Laboratory Techniques in Biochemistry and Molecular Biology*, vol. 33, pp. 1-57 (2009).

[40] A.R. Clapp, I.L. Medintz, H. Matotoussi, "Förster resonance energy transfer investigations using quantum-dot fluorophores," *ChemPhysChem.*, vol. 7, pp. 47-57 (2006).

[41] C.R. Kagan, C.B. Murray, M. Nirmal, M.G. Bawendi, "Electronic energy transfer in CdSe quantum dot solids," *Phys. Rev. Lett.*, vol. 76, pp. 1517-1520 (1996).

[42] I. L. Medintz, J. H. Konnert, A. R. Clapp, I. Stanish, M. E. Twigg, H. Mattoussi, J. M. Mauro, J. R. Deschamps, "A fluorescence resonance energy transfer-derived structure of a quantum dot-protein bioconjugate nanoassembly," *Proc. Nat. Acad. Sci. USA*, vol. 101, pp. 9612-9617 (2004).

[43] A. C. Samia, X. Chen, C. Burda, "Semiconductor quantum dots for photodynamic therapy," *J. Am. Chem. Soc.*, vol. 125, pp. 15736-15737 (2003).

[44] E. Mutlugün, I. M. Soganci, and H. V. Demir, " Photovoltaic nanocrystal scintillators hybridized on Si solar cells for enhanced conversion efficiency in UV," *Opt. Express*, vol. 16, pp. 3537-3545 (2008).

[45] B. Guzelturk, E. Mutlugun, X. Wang, K.L. Pey, H.V. Demir, "Photovoltaic nanopillar radial junction diode architecture enhanced by integrating semiconductor quantum dot nanocrystals as light harvesters," *Appl. Phys. Lett.*, vol. 97, pp. 093111 (2010).

[46] M. Achermann, M. A. Petruska, S. Kos, D. L. Smith, D. D. Koleske, V. I. Klimov, "Energy-transfer pumping of semiconductor nanocrystals using an epitaxial quantum well," *Nature*, vol. 429, pp. 642-646 (2004).

[47] J. Zhu, "Photovoltaics: More solar cells for less," *Nature Materials*, vol. 9, pp. 183-184 (2010).

[48] A. Müller, M. Ghosha, R. Sonnenschein, and P. Woditsch, "Silicon for photovoltaic applications," *Mater. Sci.Eng. B*, vol. 134, pp.257-262 (2006).

[49] E. Epstein, "Review: The anomaly of silicon in plant biology," *Proc. Natl. Acad. Sci. USA*, vol. 91, pp. 11-17 (1994).

[50] T. Stelzner, M. Pietsch, G. Andra, F. Falk, E. Ose, S. Christiansen, "Silicon nanowire-based solar cells" *Nanotechnology*, vol. 19, pp. 295203 (2008).

[51] E. C. Garnett and P. D. Yang, "Silicon nanowire radial p-n junction solar cells" *J. Am. Chem. Soc.*, vol. 130, pp. 9224-9225 (2008).

[52] L. Tsakalakos, J. Balch, J. Fronheiser, B. A. Korevaar, O. Sulima, and J.Rand, "Silicon nanowire solar cells," *App. Phys. Lett.*, vol. 91, pp.233117 (2007).

[53] B. Tian, X. Zheng, T.J. Kempa, Y. Fang, N. Yu, G. Yu, J. Huang, C.M. Lieber, "Coaxial silicon nanowires as solar cells and nanoelectronic power sources," *Nature*, vol. 449, pp. 885-890 (2007).

[54] K. Peng, Y. Xu, Y. Wu, Y. Yan, S.-T. Lee, and J. Zhu, "Aligned single-crystalline si nanowire arrays for photovoltaic applications," *Small*, vol. 1, pp. 1062-1067 (2005).

[55] J. Li, H. Y. Yu, S. M. Wong, G. Zhang, X. Sun, P. G.-Q. Lo, and D.-L. Kwong, "Si nanopillar array optimization on si thin films for solar energy harvesting," *Appl. Phys. Lett.*, vol. 95, pp. 033102 (2009).

[56] J. Zhu, Z. Yu, G. F. Burkhard, C.-M. Hsu, S. T. Connor, Y. Xu, Q. Wang, M. McGehee, S. Fan, and Y. Cui, "Optical absorption enhancement in amorphous silicon nanowire and nanocone Arrays," *Nano Lett.*, vol. 9, pp. 279-282 (2009).

[57] M. D. Kelzenberg, S. W. Boettcher, J. A. Petykiewicz, D. B. T. Evans, M. C. Putnam, E. L. Warren, J. M. Spurgeon, R. M. Briggs, N. S. Lewis, and H. A. Atwater, "Enhanced absorption and carrier collection in Si wire arrays for photovoltaic applications," *Nature Mater.*, vol. 9, pp. 239-244 (2010).

[58] J. Zhu, C.-M. Hsu, Z. Yu, S. Fan, and Y. Cui, "Nanodome solar cells with efficient light management and self-cleaning," *Nano Lett.*, vol. 10, pp. 1979-1984 (2010).

[59] S. M. Sze, *Physics of Semiconductor Devices*, 2nd ed. Wiley, New York, 1981.

[60] ASTM G173-03 Reference Spectra, National Renewable Energy Laboratory (NREL) Reference Solar Spectral Irradiance.

[61] B. Guzelturk, E. Mutlugun, X. Wang, K.L. Pey, H.V. Demir, "Photovoltaic nanopillar radial junction diode architecture enhanced by integrating semiconductor quantum dot nanocrystals as light harvesters," *Appl. Phys. Lett.*, vol. 97, pp. 093111 (2010).

[62] E. Mutlugün, I. M. Soganci, and H. V. Demir, "Nanocrystal hybridized scintillators for enhanced detection and imaging on Si platforms in UV," *Opt. Express*, vol. 15, pp. 1128-1134 (2007).

-
- [63] E. Mutlugün, I. M. Soganci, and H. V. Demir, “Photovoltaic nanocrystal scintillators hybridized on Si solar cells for enhanced conversion efficiency in UV,” *Opt. Express*, vol. 16, pp. 3537-3545 (2008).
- [64] T. Trupke, M. A. Green, and P. Würfel, “Improving solar cell efficiencies by down-conversion of high-energy photons,” *J. Appl. Phys.*, vol. 92, pp. 1668-1674 (2002).
- [65] W. G. J. H. M. van Sark, “Enhancement of solar cell performance by employing planar spectral converters,” *Appl. Phys. Lett.*, vol. 87, pp. 151117 (2005).
- [66] B. S. Richards, “Enhancing the performance of silicon solar cells via the application of passive luminescence conversion layers,” *Sol. Energy Mater. Sol. Cells*, vol. 90, pp. 2329-2337 (2006).
- [67] Z. Huang, H. Fang, and J. Zhu, “Fabrication of silicon nanowire arrays with controlled diameter, length, and density,” *Adv. Mater.*, vol. 19, pp. 744-748 (2007).
- [68] K. Peng, M. Zhang, and A. Lu, “Ordered silicon nanowire arrays via nanosphere lithography and metal-induced etching,” *Appl. Phys. Lett.*, vol. 90, pp. 163123 (2007).
- [69] Z. A. Peng and X. G. Peng, “Formation of high-quality CdTe, CdSe, and CdS nanocrystals using CdO as precursor,” *J. Am. Chem. Soc.*, vol. 123, pp. 183-184 (2001).

-
- [70] H. Zhang, Z. Zhou, B. Yang, and M. Gao, "The influence of carboxyl groups on the photoluminescence of mercaptocarboxylic acid-stabilized CdTe nanoparticles," *J. Phys. Chem. B*, vol. 107, pp.8-13 (2003).
- [71] W. W. Yu, L. Qu, W. Guo, and X. Peng, "Experimental Determination of the Extinction Coefficient of CdTe, CdSe, and CdS Nanocrystals," *Chem. Mater.*, vol. 15, pp.2854-2860 (2003).
- [72] C. B. Murray, C. R. Kagan, and M. G. Bawendi, "Synthesis and characterization of monodisperse nanocrystals and close-packed nanocrystal assemblies," *Annu. Rev. Mater. Sci.*, vol. 30, pp. 545-610 (2000).
- [73] D. V. Talapin, J.-S. Lee, M. V. Kovalenko, E. V. Shevchenko, "Prospects of colloidal nanocrystals for electronic and optoelectronic applications," *Chem. Rev.*, vol. 110, pp.389-458 (2010).
- [74] V. L. Colvin, M. C. Schlamp, A. P. Alivisatos, "Light-emitting diodes made from cadmium selenide nanocrystals and a semiconducting polymer," *Nature*, vol. 370, pp. 354–357 (1994).
- [75] S. Coe-Sullivan, W. Woo, M.G. Bawendi, V. Bulović, "Electroluminescence of single monolayers of nanocrystals in molecular organic devices," *Nature*, vol. 420, pp. 800-803 (2002).
- [76] P. O. Anikeeva, C. F. Madigan, J. E. Halpert, M. G. Bawendi, V. Bulović, "Electronic and excitonic processes in light-emitting devices based on organic materials and colloidal quantum dots," *Phys. Rev. B.*, vol. 78, pp. 085434 (2008).
- [77] S. Nakamura and G. Fasol, *The Blue Laser Diode*. Springer, Berlin (1997).

[78] E. F. Schubert, *Light Emitting Diodes*. Cambridge University Press, New York (2006).

[79] M. R. Krames, O. B. Shchekin, R. Mueller-Mach, G. O. Mueller, L. Zhou, G. Harbers, and M. G. Craford, "Status and Future of High-Power Light-Emitting Diodes for Solid-State Lighting," *J. Disp. Technol.*, vol. 3, pp.160-175 (2007).

[80] S. Nizamoglu, T. Ozel, E. Sari, and H. V. Demir, "White light generation using CdSe/ZnS core-shell nanocrystals hybridized with InGaN/GaN light emitting diodes," *Nanotechnology*, vol. 18, pp. 065709 (2007).

[81] T. Förster, "Zwischenmolekulare Energiewanderung und Fluoreszenz," *Ann. Phys.*, vol. 6, pp.55 (1948).

[82] M. Achermann, M. A. Petruska, S. Kos, D. L. Smith, D. D. Koleske, V. I. Klimov, "Energy-transfer pumping of semiconductor nanocrystals using an epitaxial quantum well," *Nature*, vol. 429, pp. 642-646 (2004).

[83] M. Achermann, M. A. Petruska, D. D. Koleske, M. H. Crawford, and V. I. Klimov, "Nanocrystal-Based Light-Emitting Diodes Utilizing High-Efficiency Nonradiative Energy Transfer for Color Conversion," *Nano Lett.*, vol. 6, pp. 1396-1400 (2006).

[84] S. Chanyawadee, P. G. Lagoudakis, R. T. Harley, M. D. B. Charlton, D. V. Talapin, and S. Lin, "Increased color-conversion efficiency in hybrid light-emitting diodes utilizing non-radiative energy transfer," *Adv. Mater.*, vol. 22, pp. 602-606 (2010).

-
- [85] S. Nizamoglu, B. Guzelturk, D. - W. Jeon, I. - H. Lee, H. V. Demir, "Efficient nonradiative energy transfer from InGaN / GaN nanopillars to CdSe / ZnS core/shell nanocrystals," *App. Phys. Lett.*, vol. 98, pp.163108 (2011).
- [86] V. Ramesh, A. Kikuchi, K. Kishino, M. Funato, Y. Kawakami, "Strain relaxation effect by nanotexturing InGaN/GaN multiple quantum well," *J. Appl. Phys.*, vol. 107, pp. 114303 (2010).
- [87] J.-H. Zhu, S.-M. Zhang, X. Sun, D.-G. Zhao, J.-J. Zhu, Z.-S. Liu, D.-S. Jiang, L.-H. Duan, H. Wang, Y.-S. Shi, S.-Y. Liu, H. Yang, "Fabrication and Optical Characterization of GaN-Based Nanopillar Light Emitting Diodes," *Chin. Phys. Lett.*, vol. 25, pp. 3485 (2008).
- [88] J. R. Lakowicz, *Principles of Fluorescence Spectroscopy*, Springer, New York, (2006).
- [89] L.-W. Wang and A. Zunger, "Pseudopotential calculations of nanoscale CdSe quantum dots," *Phys. Rev. B*, vol. 54, pp. 9579 (1996).
- [90] Q. Sun, Y. A. Wang, L. S. LI, D. Wang, T. Zhu, J. Xu, C. Yang, Y. Li, Bright, multicoloured light-emitting diodes based on quantum dots, *Nature Photonics*, vol. 1, pp. 717-722 (2007).
- [91] T.-H. Kim, K.-S. Cho, E. K. Lee, S. J. Lee, J. Chae, J. W. Kim, D. H. Kim, J.-Y. Kwon, G. Amaratunga, S. Y. Lee, B. L. Choi, Y. Kuk, J. M. Kim, K Kim, Full-colour quantum dot displays fabricated by transfer printing, *Nature Photonics*, vol. 5, pp. 176-182 (2011).

-
- [92] V.L. Colvin, M.C. Schlamp, A.P. Alivisatos, "Light-emitting diodes made from cadmium selenide nanocrystals and a semiconducting polymer," *Nature*, vol. 370, pp. 354–357 (1994).
- [93] S. Coe-Sullivan, W. Woo, M.G. Bawendi, V. Bulović, "Electroluminescence of Single Monolayers of Nanocrystals in Molecular Organic Devices," *Nature*, vol. 420, pp. 800- 803 (2002).
- [94] U. Banin, Light-Emitting Diodes Bright and Stable, *Nature Photonics*, vol. 2, pp. 209-210 (2008).
- [95] A. H. Mueller, M. A. Petruska, M. Achermann, D. J. Werder, E. A. Akhador, D. D. Koleske, M. A. Hoffbauer, V. I. Klimov, Multicolor light-emitting diodes based on semiconductor nanocrystals encapsulated in GaN charge injection layers, *Nano Lett.*, vol. 4, pp. 1039-1044 (2005).
- [96] P. O. Anikeeva, C. F. Madigan, J. E. Halpert, M. G. Bawendi, V. Bulović, Electronic and excitonic processes in light-emitting devices based on organic materials and colloidal quantum dots, *Phys. Rev. B.*, vol. 78, pp. 085434 (2008).
- [97] M. Achermann, M. A. Petruska, S. Kos, D. L. Smith, D. D. Koleske and V. I. Klimov, Energy-transfer pumping of semiconductor nanocrystals using an epitaxial quantum well, *Nature*, vol. 429, pp. 642-646 (2004).
- [98] S. Nizamoglu, B. Guzelturk, D.-W. Jeon, I.- H. Lee, H. V. Demir, Efficient nonradiative energy transfer from InGaN/GaN nanopillars to CdSe/ZnS core/shell nanocrystals, *App. Phys. Lett.*, vol. 98, pp. 163108 (2011).

-
- [99] D. V. Talapin, J-S Lee, M V. Kovalenko and E V. Shevchenko, Prospects of Colloidal Nanocrystals for Electronic and Optoelectronic Applications, *Chem. Rev.*, vol. 110, pp. 389-458 (2010).
- [100] E. Holder, N. Tessler, A. Rogach, Hybrid nanocomposite materials with organic and inorganic components for opto-electronic devices, *J. Mater. Chem.*, vol. 18, pp. 1064-1078 (2008).
- [101] N. Tomczak, D. Janczewski, M. Han, G. J. Vancso, Designer polymer-quantum dot architectures, *Prog. in Poly. Sci.*, vol. 34, pp. 393-430 (2009).
- [102] F.B. Dias, K.T. Kamtekar, T. Cazati, G. Williams, M.R. Bryce, A.P. Monkman, Exciton diffusion in polyfluorene copolymer thin films: kinetics, energy disorder and thermally assisted hopping, *Chem. Phys. Chem.*, vol. 10, pp. 2096-2104 (2009).
- [103] H. Sirringhaus, N. Tessler, R. H. Friend, Integrated optoelectronic devices based on conjugated polymers, *Science*, vol. 280, pp. 1741-1744 (1998).
- [104] M. Anni, L. Manna, and R. Cingolani, D. Valerini, A. Creti, M. Lomascolo, Förster energy transfer from blue emitting polymers to colloidal CdSe/ZnS core shell quantum dots, *App. Phys. Lett.*, vol. 85, pp. 6149 (2004).
- [105] T. Stöferle, U. Scherf, R. F. Mahrt, Energy transfer in hybrid organic/inorganic nanocomposites, *Nano Lett.*, vol. 9, pp.453-456 (2009).
- [106] A. A. Lutich, A. Pöschl, G. Jiang, F. D. Stefani, A. S. Susa, A. L. Rogach, J. Feldmann, Efficient energy transfer in layered hybrid organic/inorganic nanocomposites: A dual function semiconductor nanocrystals, *Appl. Phys. Lett.*, vol. 96, pp. 083109 (2010).

[107] J. Kwak, W. K. Bae, M. Zorn, H. Woo, H. Yoon, J. Lim, S. W. Kang, S. Weber, H.-J. Butt, R. Zentel, S. Lee, K. Char, C. Lee, Characterization of quantum dot/conducting polymer hybrid films and their application in light-emitting diodes, *Adv. Mater.*, vol. 21, pp. 5022-5026 (2009).

[108] Z.-S. Guo, L. Z., J. Pei, Z.-L. Zhou, G. Gibson, J. Brug, S. Lam, S. S. Mao, CdSe/ZnS nanoparticle composites with amine-functionalized polyfluorene derivatives for polymeric light-emitting diodes: synthesis, photophysical properties, and the electroluminescent performance, *Macromolecules*, vol. 43, pp. 1860-1866 (2010).

[109] H. Skaff, K. Sill, T. Emrick, Quantum dots tailored with Poly(paraphenylene vinylene), *J. Am. Chem. Soc.*, vol. 126, pp.11322-11325 (2004).

[110] S. Pathak, S.-K. Choi, N. Arnheim, M. E. Thompson, Hydroxylated quantum dots as luminescent probes for in situ hybridization, *J. Am. Chem. Soc.*, vol. 123, pp. 4103-4104 (2001).

[111] A. A. Lutich, G. Jiang, A. S. Susa, A. L. Rogach, F. D. Stefani, J. Feldmann, *Nano. Lett.*, vol. 9, pp. 2636- 2640 (2009).

[112] W.L. Bae, K. Char, H. Hur, S. Lee, Single step synthesis of quantum dots with chemical composition gradients, *Chem. Mater.*, vol. 20, pp. 531–539 (2008).

[113] T. Förster, Intermolecular energy migration and fluorescence, *Ann. Phys.*, vol. 2, pp. 55 (1948).

-
- [114] L. Romaner, A. Pogantsch, P. Scandiucci de Freitas, U. Scherf, M. Gaal, E. Zojer, E. W. List, The origin of green emission in polyfluorene-based conjugated polymer: on-chain defect fluorescence, *Adv. Funct. Mater.*, vol. 13, pp. 597-601 (2003).
- [115] I. G. Scheblykin, A. Yartsev, T. Pullerits, V. Gulbinas, V. Sundström, Excited state and charge photogeneration dynamics in conjugated polymers, *J. Phys. Chem. B*, vol. 11, pp. 6303-6321 (2007).
- [116] R.F. Loring, H.C. Anderson, M.D. Fayer, Electronic excited-state transport and trapping in solution, *J. Chem. Phys.*, vol. 76, pp. 2015-2027 (1982).
- [117] V. Gubinas, I. Mineviciute, D. Hertel, R. Wellander, A. Yartsev, V. Sundström, Exciton diffusion and relaxation in methyl-substituted polyparaphenylene polymer films, *J. Chem. Phys.*, vol. 127, pp. 144907 (2007).
- [118] U. Gösele, M. Hauser, U. K. A. Klein, and R. Fray, Diffusion and long-range energy transfer, *Chem. Phys. Lett.*, vol. 34, pp. 519-522 (1975).
- [119] L.M. Herz, C. Silva, A.C. Grimsdale, K. Müllen, R.T. Phillips, Time-dependent energy transfer rates in a conjugated polymer guest-host system, *Phys. Rev. B*, vol. 70, pp. 165207 (2004).
- [120] F. Dias, K. T. Kamtekar, T. Cazati, G. Williams, M. R. Bryce, A.P. Monkman, Exciton diffusion in polyfluorene copolymer thin films: kinetics, energy disorder and thermally assisted hopping, *ChemPhysChem.*, vol. 10, pp. 2094-2104 (2009).

[121] D. Beljonne, G. Pourtois, C. Silva, E. Hennebieq, L. M. Herz, R.H. Friend, G.D. Scholes, S. Setayesh, K. Müllen, J.L. Bredas, Interchain vs. intrachain energy transfer in acceptor capped conjugated polymers, Proc. Natl. Acad. Sci. U.S.A., vol. 99, pp.10982 (2002).

[122] Y.Wang, N. Herron, "Semiconductor nanocrystals in carrier-transporting polymers. Charge generation and charge transport," J. Lumin., vol. 70, pp. 48–59 (1996).

[123] M. A. Baldo, D. F. O'Brien, Y. You, A. Shoustikov, S. Sibley, M. E.Thompson, S. R. Forrest, Highly efficient phosphorescent emission from organic electroluminescent devices," Nature, vol. 395, pp.151-154 (1998).

[124] P. O. Anikeeva, J. E. Halpert, M. G. Bawendi, V. Bulovic, "Quantum dot light emitting devices with electroluminescence tunable over the entire visible spectrum," Nano Lett., vol. 9, pp. 2532-2536 (2009).